SISSA ISAS

SCUOLA INTERNAZIONALE SUPERIORE DI STUDI AVANZATI
INTERNATIONAL SCHOOL FOR ADVANCED STUDIES

Joint Evolution of Supermassive Black Holes and Host Galaxies at High Redshift:

AGN Luminosity Functions and Protogalactic Reionization

Thesis submitted for the degree of
Doctor Philosophiæ

CANDIDATE:

Jirong Mao

SUPERVISORS:

Prof. Luigi Danese
Dr. Andrea Lapi

October 2006

Contents

Preface

Except the successful accomplishment from the hierarchical scenario of galactic formation and evolution, during recent years, the new discovery and progress have being attracted the interest of more and more insightful astronomers: The results of deep survey have shown that massive galactic objects occur at high redshift while small ones shine in the local universe, these downsizing features motivate the exploration towards the high redshift; Black hole/AGN activity and galactic formation and evolution are tightly linked together; The feedback of supernova and AGN, which could prevent the baryons to follow the distribution of dark halo, has been confirmed by the observations and taken into account in the most of theoretical models nowadays.

In the thesis, the investigations are within the framework of the semi-analytical model of coevolution between black holes growth and host spheroid galaxies(Granato et al. 2004). Two specific issues are put forward: (1) Black hole growth and AGN luminosity function, as one side of the coevolution model, provides the fully evolutionary information to explain the observational downsizing features; (2) Star formation history, as the other side of the coevolution model, constructs the stellar population properties and makes the tight constraint to the research of reionization.

The clue of the thesis has been arranged as the following: After the introduction in Chapter 1, the observational research for high redshift AGNs in the Chapter 2 is given for preparing the AGN luminosity function at the faint end; The model of the whole scenario and AGN luminosity function fitting is in the Chapter 3 while the reionization from the protogalaxies is in the Chapter 4; In the Chapter 5, the intrinsic evolution sequence of galaxies is put forward as the conclusion.

The associated materials are presented in the content. Here it is only additional exposition: The background of galactic formation and evolution illustrated in the section 3.1 and 3.2 could be required for the deep understanding about the status of this complex field while observational process presented in the Appendix should not be ignored although the major stuff of the thesis is concerned as theoretical work.

Acknowledgments

During the period of the study in SISSA, Prof. Luigi Danese gives me the direction like the lighthouse with his wide background. He also teaches me the capability to go further carefully from one initial topic until the time that the whole scenario has been grasped. I am so happy to discuss with Dr. Andrea Lapi, he often helps me of the detailed calculation. Prof. Stefano Cristiani puts his patience to teach me the knowledge and the skills of the observation and instruments. Dr. Gian Luigi Granato provides me the code so that I can make the ideas into reality. All of the staff members and my classmates are friendly and warm-hearted to me. I am grateful for all of them.

Citations to previously published works

Part of the work presented in the thesis has appeared in the following papers:

Late Reionization from Protogalactic Spheroids.
Mao, J., Lapi, A., Granato, G.L., Bressan, S., De Zotti, G., Danese, L., 2006, MNRAS, to be submitted

Quasar Luminosity Functions from Joint Evolution of Black Holes and Host Galaxies.
Lapi, A., Shankar, F., Mao, J., Granato, G.L., Silva, L., De Zotti, G., Danese, L., 2006, ApJ, accepted, astro-ph/0603819

The Luminosity Function of high-redshift QSOs - a combined analysis of GOODS and SDSS.
Fontanot, F., Cristiani, S., Monaco, P., Nonino, M., Vanzella, E., Brandt, N., Grazian, A., Mao, J., Stern, D., 2006, A&A, submitted

Chapter 1

Introduction: Cosmology Scenario and AGN Phenomena

First of all, the contents of the standard cosmology are introduced in the Section 1.1. The large structure formed from the initial perturbation is described in the Section 1.2. Based on the standard cosmology scenario, two different models of galactic formation and evolution are presented briefly in the Section 1.3. Active Galactic Nuclei(AGN), one kind of the most interesting objects and the topic of the thesis, is emphasized in the Section 1.4. Finally, in the Section 1.5, the aims of faint AGN research using the project of Great Observatories Origins Deep Survey(GOODS) are discussed.

1.1 Standard Cosmology

The standard cosmology believes that our universe is spatially flat, homogeneous and isotropic on the large scales. Gravitation is the dominant force and the theory of general relativity which is derived by equivalence principle gives us the link between the matter and the geometry of spacetime. From the general relativity, we have the dynamics equation:

$$\frac{\ddot{a}}{a} = -\frac{4\pi G}{3}(\rho + 3p) \tag{1.1}$$

$$\frac{\dot{a}^2 + k}{a^2} = \frac{8\pi G}{3}\rho \tag{1.2}$$

The equations (1) and (2) plus certain state equation can describe the dynamic feature of the universe(Weinberg 1972).

There are relativistic and non-relativistic components in the universe. Massless photons(light) and nearly massless neutrinos are relativistic matters. Baryon, dark matter and dark energy could be non-relativistic matters. Baryon is the "ordinary matter" composed primarily of protons, neutrons and electrons. Dark matter generally refers to the "exotic" non-baryon stuff that has no interaction with the ordinary matter except gravitational interaction. It is assumed to play the important role on the galactic formation. Dark energy is perhaps a property of the vacuum itself, which is characterized by the negative pressure. It is the only form of matters that can cause the expansion of the universe to accelerate, or speed up.

The so-called standard cosmology, a flat Λ-dominated universe seeded by a nearly scale-invariant adiabatic Gaussian fluctuations, can fit the observation of WMAP(Bennett et al. 2003; Spergel et al. 2003, 2006) well. It means that we have the cosmological parameters as below(Spergel et al. 2006)[1]: baryon is only a small portion of the universe, say, 4% ($\Omega_b h^2 = 0.022 \pm 0.001$), 23% is the cold dark matter ($\Omega_m h^2 = 0.13 \pm 0.01$), the last 73% is the dark energy, Hubble constant is $H_0 = 74 \pm 3 kms^{-1} Mpc^{-1}$ and the fluctuation $\sigma_8 = 0.76 \pm 0.05$.

1.2 From Perturbation to Structure Formation

The standard cosmology determined by the general relativity gives the successful framework to our universe. Furthermore, from the very early, homogeneous and isotropic epoch to the present day in which the universe is full of galaxies and clusters, the processes of the structure formation dominate.

The universe inflation is a popular scenario to produce the small over-densities and these over-densities then grow over a period time and eventually form the structures which we can observe now. The inflation is initi-

---

[1] Except the special note, these standard parameters of ΛCDM model have been adopted in the whole thesis.

ated at the scale corresponding to the breaking of the symmetry of grand unification at the energy about $10^{16}Gev$ and the time about $10^{-35}s$. The equations (1) and (2) have the solution of di Sitter space $a \propto expHt$ where $H = \sqrt{8\pi G\rho_{vacuum}/3}$. If this model is correct, the universe indeed had the exponentially expansion and the inflation gives the direct prediction that the universe must be spatially flat(Peacock 1999).

The inflation gives the universe the initial energy density fluctuations. A perturbation analysis of the scalar field's evolution predicts a power spectrum. After inflation, the universe comes into a radiation dominated era. The perturbation of the primordial power spectrum grows as $\delta\rho/\rho \propto a^2$. With the universe expansion, the situation becomes matter-dominated. The perturbation grows continually, but with $\delta\rho/\rho \propto a$. At the redshift about 1100, there is the decoupling of matter and radiation. The radiation of photons is the so-called cosmic microwave background(Padmanabhan 1993).

When the perturbations have grown sufficiently, the self-gravity will start dominating and the dark matter will collapse and form into the virialized, gravitationally bound systems. These systems are called dark matter halos. Once the dark matter halo is formed, it will remain at a mean density which is about 200 times of the background density of the universe. It is required to have the comoving number density of the dark matter halos at a given epoch as a function of the mass. Here it is the famous Press-Schechter mass function(Press & Schechter 1974, Sasaki 1994):

$$N_{ps}(M,t) = \sqrt{\frac{2}{\pi}}\frac{\rho_0}{M}\frac{\delta_c}{D(t)}|\frac{1}{\sigma^2}\frac{d\sigma}{dM}|\exp(\frac{-\delta_c^2}{2\sigma^2(M)D(t)^2}) \tag{1.3}$$

where $\delta_c = 1.68$, ρ_0 is the mean comoving density and $D(t) = 1/(1+z)$ is the Peebles function for the growth of the perturbations. Moreover,

$$\sigma^2(M) = \int_0^{k_s} P(k)4\pi k^2 dk \tag{1.4}$$

where P(k) is the power spectrum of the density fluctuation and k_s is linked by $M = 6\pi^2\rho_0 k_s^{-3}$(Mahmood, Devriendt & Silk 2005).

Alternatively, after dark matter halo forms, at first, the hot baryons are diffuse upon the potential well. Then, by cooling process, the baryons will lose energy, sink to the center of the dark matter halo and form into galaxies and clusters. During the whole process, the baryon and the dark matter have no collision. Therefore, it is important to calculate the cooling timescale of the baryons (Silk & Bouwens 2001). Clearly, if the cooling time of the gas is larger than the Hubble time, the gas can not evolve during the history of the universe. If the cooling time is smaller than the Hubble time but larger than the dynamic time($t_{dyn} \sim \sqrt{1/G\rho}$), the gas will be slowly quasi-static collapse into the center of the dark matter halo. If the cooling time of the gas is smaller than the dynamic time, the galaxy will be effectively formed. Compton cooling as one possible process will be important at redshift larger than 10 while at lower redshift the dominant cooling mechanism is bremsstrahlung especially for the gas which is in the massive dark halo.

1.3 Galactic Formation and Evolution: Hierarchical or Monolithic

After the cooling of baryons in the dark matter halos, the stars and galaxies are formed[2]. There are two prevailing scenarios for the formation and evolution of galaxies: one in which ellipticals formed at high redshift from monolithic collapse and the other in which ellipticals formed as the hierarchy by mergers from spiral galaxies.

For the former situation, the early collapse and fragmentation into stars prior to the collapse of the halo can constitute the core of the elliptical while stars formed from the secondary gas infall can constitute the shallower wings. The dark halos may form at redshift beyond 10 so that the angular momentum of the slow-rotating ellipticals can be no larger than 0.05.

For the hierarchical case, the resultant angular momentum for the formed elliptical can be considerably smaller than that of the colliding disk galaxies. There are examples of disks merging into ellipticals in the local universe and it is conceivable that mergers were more frequent in the past. Some ellipticals possess features, such as shells or other sharp features, indicative of mergers

---

[2] Since the galactic formation and evolution is an open problem, in this section, the basic pictures are only introduced simply. The detailed discussion will be presented in the Chapter 3.

or other violent formation. Detailed N-body simulations of mergers represent the observations well.

1.4 AGN Description

1.4.1 Taxonomy

During the structure formation, the galaxies and the stars are formed. The normal galaxy is considered in the sense that their energy emission is thermal radiation mostly from the stars. Alternatively, another class of the extragalactic sources is Active Galactic Nuclei (AGN) which produces the high luminosity about $10^{46} ergs\ s^{-1}$ powered by accretion in the center of the host galaxy and shows a gross power-law spectrum from radio to high energy band.

From the phenomenon, the traditional classification of AGNs are including(Peterson 1997):

(1) Seyfert galaxies: low luminosity $M_B > -21.5$ with the strong, high-ionization emission lines.

- Seyfert 1 galaxies: with both broad(width up to $10^4 kms^{-1}$) and narrow lines(width about a few hundred kilometers per second);

- Seyfert 2 galaxies: only with narrow lines.

(2) Quasi-Stellar Objects(Quasar or QSOs): the most luminous($M_B < -21.5$) subclass of AGNs and the angular size less than 7 arcsecond;

(3) Low-Ionization Nuclear Emission Regions(LINERs): Spectroscopically, they resemble Seyfert 2 galaxies, except the low-ionization lines, e.g., [OI] and [NII] are relatively strong.

(4) Blazars: mainly include BL Lac objects and Optically Violent Variables(OVV) which have highly variable in radio, optical and X-ray bands with no broad optical emission lines.

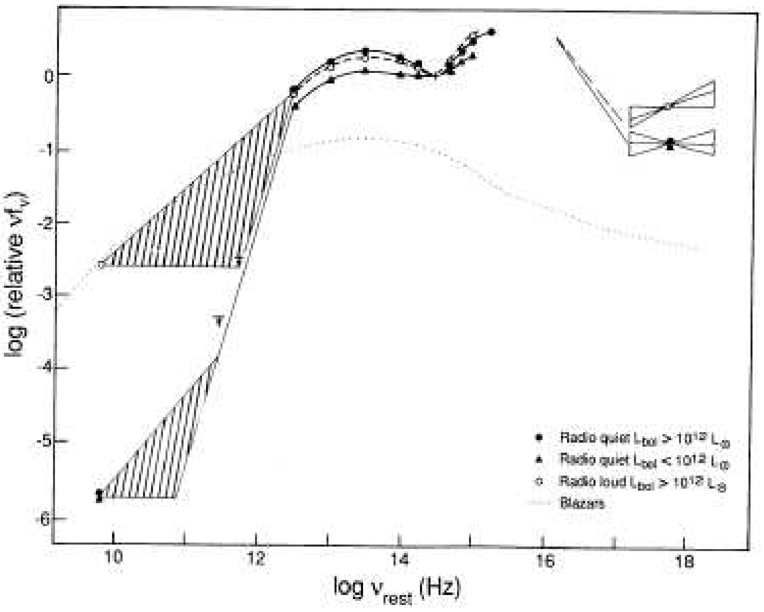

Figure 1.1: AGN Broad-band Spectral Energy Distribution

1.4.2 Broad-band Spectrum and Unified Model

The average multi-wavelength spectrum of AGN is shown in Fig. 1.1(Sanders et al. 1989). Here, some of the important observing features need to be included: The spectrum in the radio band is non-thermal and relatively steep; A significant amount of energy is emitted in a broad feature that dominates the spectrum from about $4000\mathring{A}$ to the UV band; the emission in the range from 10nm to $0.3\mu m$ is called the big blue bump while the emission between $2\mu m$ and 1mm is known as infrared bump; In the X-ray region, below 1keV, the emission is seriously affected by absorption, within 2-10keV, the spectrum can be well approximated by a power law and beyond 10keV the spectrum is flattened.

Although AGNs show all kind of different morphology types as described in the Section 1.4.1, we can view them as a whole(for a review, see Begelman, Blandford & Rees 1984) by the so-called unified model(Antonucci 1993, Urry & Padovani 1995) as shown in the Fig. 1.2[3].

---

[3] cited by ESO messenger article in www.eso.org/science/goods

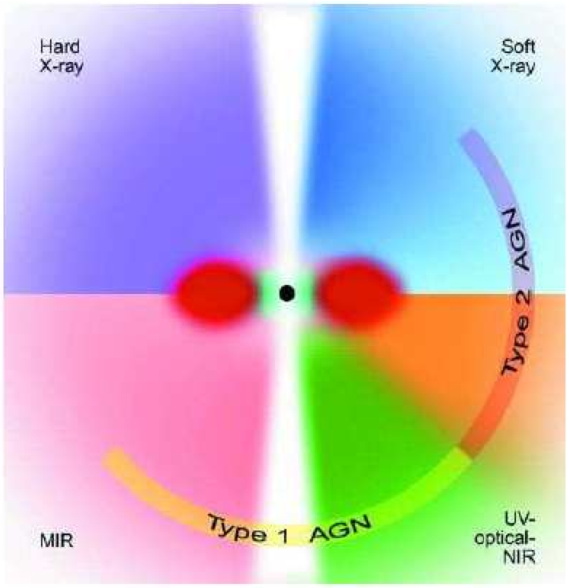

Figure 1.2: AGN Unified Model

At the AGN center, the deep potential well which is popularly regarded as massive black hole of 10^6 to 10^8 solar mass is confirmed by Fe K-alpha line in the X-ray band(Tanaka et al. 1995). Around the massive black hole, there is the disk which is formed by the gravitational accretion due to the central black hole and the thermal emission from the disk fits the big blue bump well in the UV band. The accretion mechanism is well presented by a geometry-thin and optical-thick disk(Shakura & Sunyaev 1973) or/and an advection-dominated accretion flow(ADAF) model(Narayan & Yi 1994). The jet is powered directly by the central black hole(Blandford & Znajek 1977) or by the magnetic accretion disk(Blandford & Payne 1982). Moreover, the outside part is the torus made by molecular dust which may be optical thick(Pier & Krolik 1992, Granato & Danese 1994). the Broad-Line Region(BLR) which is a few pc far away from the central black hole produces the broad emission lines and the Narrow-Line Region(NLR) whose distance is 100-1000pc can be spatially resolved in the optical band and contributes the narrow emission lines to the spectrum(Peterson 1997).

Due to accretion, the central engine is powered not by the nuclear action as the stars but gravitation. The inward gravitational force will balance the outward radiation force, so that the luminosity is linked to the central black hole mass and it is defined by Eddington luminosity:

$$L_E = \frac{4\pi G c m_p}{\sigma_T} M \tag{1.5}$$

where M is the central mass which provides the luminosity reach the Eddington limit.

Given certain efficiency ε, the bolometric luminosity is(Small & Blandford 1992):

$$L_{bol} = \varepsilon \dot{M} c^2 = \lambda \frac{M_{BH}}{t_{edd}} c^2 \tag{1.6}$$

in which

$$\dot{M} = \frac{dM_{BH}}{dt} \tag{1.7}$$

is the mass accretion rate, $t_{edd} = \sigma_T c/4\pi G m_p = 4.6 \times 10^8 year$ is the Eddington timescale and λ is the Eddington ratio. Therefore, the seed black holes at high redshift increase as exponential form:

$$M_{BH} = M_0 exp(\lambda t/\varepsilon t_{edd}) \tag{1.8}$$

It is noticed that the black holes may grow by super-Eddington accretion at high redshift. The pioneer idea of the black hole super-Eddington accretion is proposed theoretically by Begelman (1978). The detailed model of the moderately supper-Eddington accretion is the so-called slim disk(e.g. Abramowicz 1988) or magnetized thin disk with photon bubble instability(Begelman 2002). It is quite possible that super-Eddington condition prevails for most of the time that the central black hole mass is being built up. From the observational view, this accretion mode has been considered to have the $M_{BH} - FWHM(H\beta)$ relation(Wang 2003) and possible evidence of the narrow line Seyfert 1 galaxies and narrow line QSOs(Kawaguchi, Pierens & Huré 2004, Kawaguchi et al. 2004).

1.4.3 Selection Methods

Since AGNs are far away from the earth, they look like the points on the image. This morphology character can be naturally used to distinguish with the local galaxies.

Optical selection is one of the traditional methods for AGN research. Using one telescope to do spectroscopy, we can see the strong emission lines, such as Lyman alpha1216, MgII2798 and CIV1549. This is one effective identification method because very few stars have these typical emission lines and optical spectroscopy is a widely-used and mature technique. However, if we need to select high redshift and faint samples which emit weak light in the optical band, even very big ground-based telescopes have difficulties to obtain the spectroscopy.

Multi-band photometry survey and optical color is another useful method to select AGN. The optical colors of AGN which are modeled as a power law plus broad emission lines deviated in a systematic way from pure stellar colors as a function of power-law index, redshift and the fraction of total light in the non-thermal continuum(Sandage 1971). Using the multicolor data, it is possible to construct color ratios that efficiently select objects with unusual values. This is especially useful for high redshift AGN survey. Since the optical spectra of AGNs have different shapes from those of stars and galaxies so that the ratios of their fluxes in different photometry bands can be distinguished(Krolik 1999). Using this multicolor survey method, recently, Sloan Digital Sky Survey(SDSS) even get the bright AGN at redshift 6.43(Fan et al. 2003) and obtained the complete Gun-Peterson trough to determine the reionization epoch(Fan et al. 2002).

Since AGNs are multi-wavelength emission objects, compared with the ordinary galaxies and stars, they have the particularly strong X-ray radiation. Besides optical selection, X-ray survey is another efficient way especially for searching the obscured AGN which can be hardly found by optical selection. The advantages of X-ray selection of AGN include(Mushotzky 2004):

(1)High contrast between the AGN and the stellar light;

(2)A relatively large fraction of the bolometric energy(3-20%) is radiated in the classical X-ray bands;

(3)Penetrating power of X-rays. Column densities corresponding to $A_V = 5(N_H \sim 10^{22} cm^{-2})$ only reduce flux by 3 in the Chandra and XMM soft X-ray bands observation;

(4)Accurate positions from Chandra. Unique identifications can be made with counterparts in other wavelength bands;

(5)High areal density of X-ray-selected AGN reaching 400 sources deg^{-2} at $F_X \sim 10^{-15} ergscm^{-2}s^{-1}$ in the 2-8keV band of Chandra observation.

Due to the Chandra deep survey(Rosati et al. 2002), the origin of the X-ray background has been understood(Gilli 2003). Optical identification shows that the main contribution of X-ray background is original from AGN and most sources are found at the redshift distribution $z < 1$. From the X-ray background observation, the synthesis model tests the different ratios between obscured and unobscured AGN by different redshifts(Gilli, Salvati & Hasinger 2001). In the local universe, the correlation between the nuclear dust of 100pc scale and the Compton thin($10^{23}cm^{-2} \leq N_H \leq 10^{24}cm^{-2}$) obscuration has been confirmed and it can be interpreted as due to the large covering fraction of gas associated with dust lanes(Guainazzi, Matt & Perola 2005). The work of X-ray selected AGN at very high redshift $z > 5$ has also been done by the Chandra deep field(Barger et al. 2003). In the X-ray study, the hardness ratio is defined as $(H - S)/(H + S)$, where S and H are the soft(0.5-2keV) and hard(2-8keV) X-ray band net counts. The high redshift AGN($z > 5$) should appear soft in X-ray band with the hardness ratio about -0.5 and those of Compton thick($N_H > 10^{24}cm^{-2}$) could have the ratio about 0.0(Wang et al. 2004).

During the survey strategy, for both optical and X-ray observation, the sensitive flux limit should be considered. The Great Observatories Origins Deep Survey(GOODS) provides one of the deepest observations nowadays available and it will be described in the Chapter 2.

1.4.4 Type 1/Type 2 or Obscured/Unobscured

Usually, by optical selection, AGNs can be classified into type 1 which show both broad lines and narrow lines and type 2 which show only narrow lines. By X-ray selection, AGNs can be divided as obscured and unobscured subclass. Here, the term of “obscure” means the nucleus of the source is hidden behind the absorbing materials. Thus obscured AGNs are prevented from being directly observed in optical band, but still can be found through an X-ray telescope. Of this kind of obscured materials, the mainly composition may be the grain which dominate around the circumnuclear region(Maiolino et al. 2001; Maiolino, Marconi & Oliva 2001).

For optical observation the absorption effect can be measured as the absorption parameter A_v and for X-ray observation the absorption can be measured as the column density of neutral hydrogen N_H. Therefore, the classification is shown in the Fig. 1.3 and 1.4(Gilli, Risaliti & Severgnini 2001).

Since the emission of AGN will be more strongly absorbed in optical band than in X-ray band while X-ray selection is still short of the Compton-thick sources, the strict relations between optical and X-ray classifications are(Matt 2002):

$$type1 \longleftarrow unobscured \tag{1.9}$$

$$type2 \longrightarrow obscured \tag{1.10}$$

1.4.5 Observational Optical and X-ray Luminosity Function

One of the topics for understanding the distribution of objects in the universe is luminosity function. The AGN luminosity function is the number density as the function of luminosity or magnitude[4]. It is relevant for the cosmology since it is believed to trace the formation of the cosmic structure. Therefore the luminosity function contains almost all the information about the AGN evolution. Given the integrated density as the function of redshift we have the density evolution and given the mean luminosity as a function of the redshift we have the luminosity evolution.

The AGN luminosity function in optical band has been well studied(Boyle, Shanks & Peterson 1988; Pei 1995; Boyle et al. 2000; Croom et al. 2004) using all kinds of observational data. As an example, it can be described by the double power law at low redshift from 2dF survey as(Croom et al. 2004):

$$\Phi(M_{bj}, z) = \frac{\Phi(M^*_{bj})}{10^{0.4(\alpha+1)(M_{bj}-M^*_{bj})} + 10^{0.4(\beta+1)(M_{bj}-M^*_{bj})}} \tag{1.11}$$

---

[4] the methods and calculation for derivation of luminosity function from observational data are shown in the Appendix B.1.

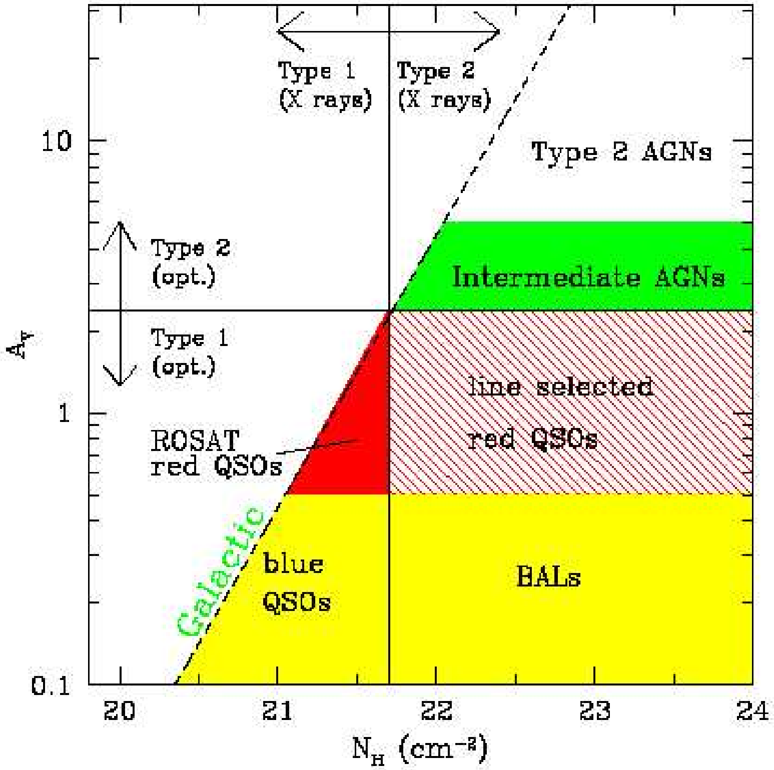

Figure 1.3: AGN Classification in the A_V-N_H Plane

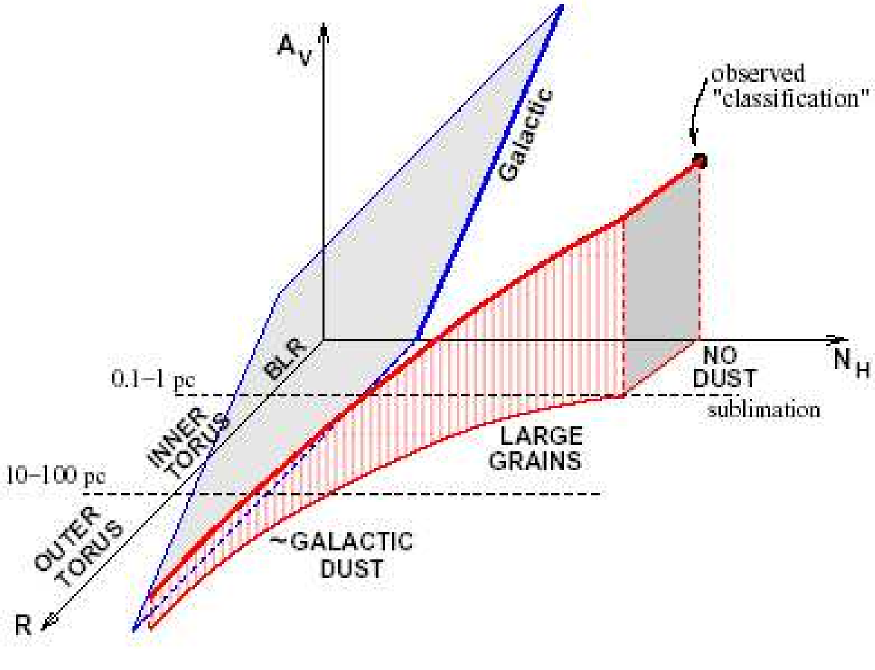

Figure 1.4: AGN Classification in 3D

where M_{bj}^{*} is the break magnitude, α and β are corresponding parameters. The luminosity evolution has the second-order polynomial form:

$$M_{bj}^{*} = M_{bj}^{*}(z=0) - 2.5(k_1 z - k_2 z^2) \tag{1.12}$$

or an exponential form with look-back time τ:

$$M_{bj}^{*} = M_{bj}^{*}(z=0) - 1.08 k_1 \tau \tag{1.13}$$

The Fig. 1.5 shows the AGN luminosity function derived by Croom et al. (2004).

For the X-ray luminosity function of AGNs, previous studies have been obtained in both soft(0.5-2keV) X-ray band(Miyaji, Hasinger & Schmidt 2000; Miyaji, Hasinger & Schmidt 2001; Hasinger, Miyaji & Schmidt 2005) and hard(2-10keV) X-ray band(Cowie et al. 2003; Ueda et al. 2003; Barger et al. 2005). For instance, in hard X-ray band, the luminosity function from a combination dataset of HEAO1, ASCA and Chandra survey has been shown as a double power law by Ueda et al. (2003):

$$\frac{d\Phi(L_X, z=0)}{dlogL_X} = A[(\frac{L_X}{L_*})^{\gamma 1} + (\frac{L_X}{L_*})^{\gamma 2}]^{-1} \tag{1.14}$$

where L_* is the break luminosity, A, $\gamma 1$ and $\gamma 2$ are corresponding parameters.

The pure luminosity evolution is expressed as:

$$\frac{d\Phi(L_X, z)}{dlogL_X} = \frac{d\Phi[L_X/e(z), 0)]}{dlogL_X} \tag{1.15}$$

while the pure density evolution model is:

$$\frac{d\Phi(L_X, z)}{dlogL_X} = \frac{d\Phi(L_X, 0)}{dlogL_X} e(z) \tag{1.16}$$

where

$$e(z) = \begin{cases} (1+z)^{p1} & (z < z_c) \\ e(z_c)[(1+z)/(1+z_c))]^{p2} & (z \geq z_c) \end{cases} \tag{1.17}$$

in which z_c, p1 and p2 are corresponding parameters.

A more sophisticated model of luminosity-dependent density evolution has also been proposed as below:

$$\frac{\mathrm{d}\Phi(L_{\mathrm{X}}, z)}{\mathrm{dLog}L_{\mathrm{X}}} = \frac{\mathrm{d}\Phi(L_{\mathrm{X}}, 0)}{\mathrm{dLog}L_{\mathrm{X}}} e(z, L_{\mathrm{X}}) \tag{1.18}$$

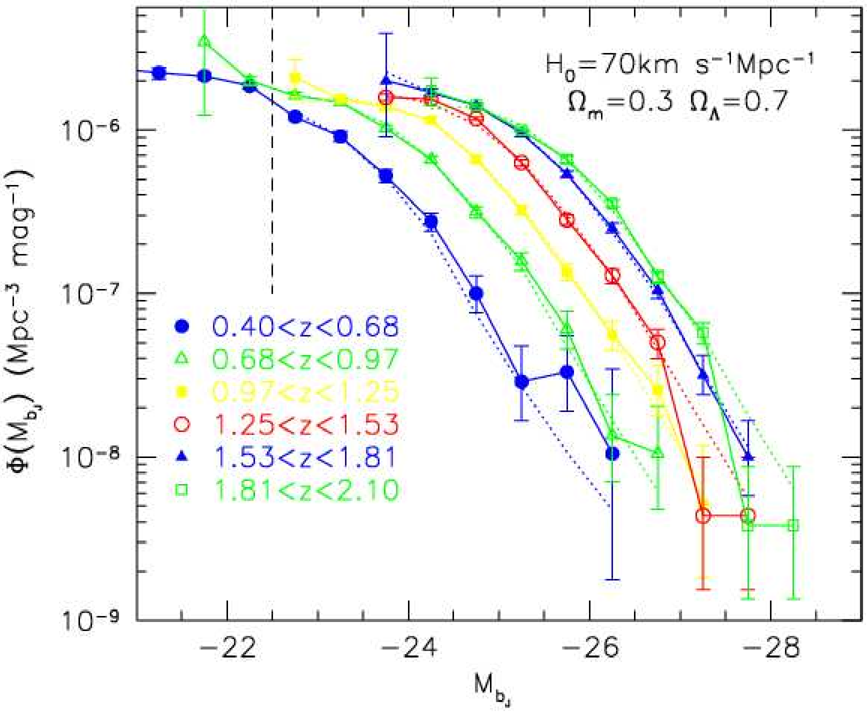

Figure 1.5: The Optical Luminosity Function of AGN

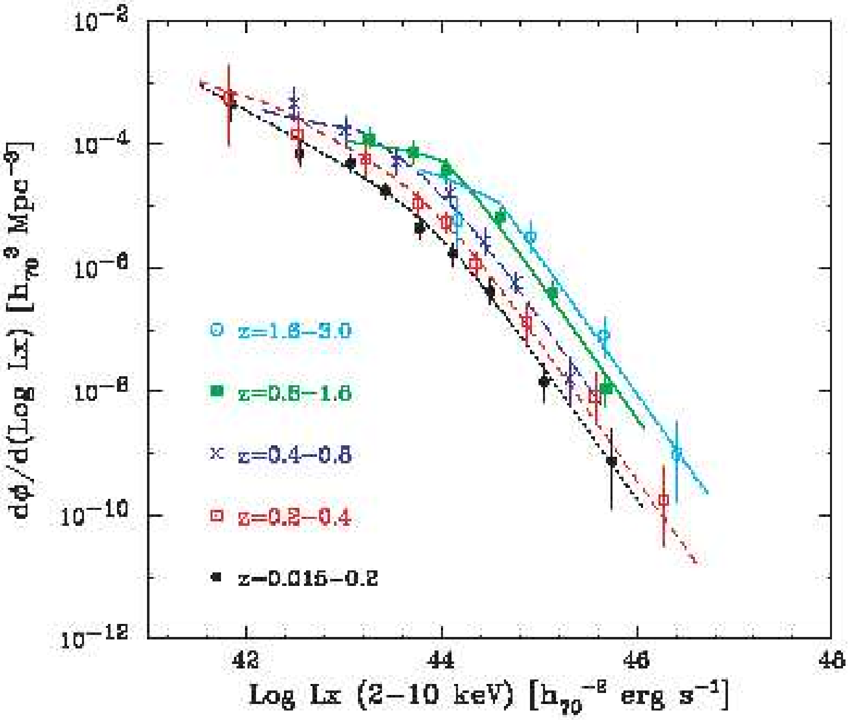

Figure 1.6: The X-ray luminosity Function of AGN

where the functions

$$e(z, L_{\mathrm{X}}) = \begin{cases} (1+z)^{p1} & (z < z_c(L_X)) \\ e(z_{\mathrm{c}})[(1+z)/(1+z_c(L_X))]^{p2} & (z \geq z_c(L_X)) \end{cases} \tag{1.19}$$

and

$$z_{\mathrm{c}}(L_{\mathrm{X}}) = \begin{cases} z_{\mathrm{c}}^{*} & (L_{\mathrm{X}} \leq L_a) \\ z_{\mathrm{c}}^{*}(L_{\mathrm{X}}/L_a)^{\alpha} & (L_{\mathrm{X}} < L_a) \end{cases} \tag{1.20}$$

in which z_{c}^{*} and L_a are corresponding parameters.

The evolution of X-ray luminosity function(Ueda et al. 2003) is shown in the Figure 1.6. Barger et al. (2005) found that the hard X-ray luminosity functions of AGNs were well described by pure luminosity evolution at $z < 1.2$. For the higher redshifts, the number densities had the evidence of a decline(Ueda 2003; Barger & Cowie 2005; see however Nandra et al. 2005).

1.4.6 Clustering

Besides the luminosity function, the clustering property is another fundamental tool used to understand the formation and evolution of the cosmic structure. The clustering is expected to show up among pairs or groups of AGNs which are close to each other in both redshift and position on the sky(Shaver 1984). The typical two-point correlation function is defined to describe the clustering as(Shank et al. 1987):

$$\xi(r) = \frac{N_{qq}}{N_{qr}} - 1 \tag{1.21}$$

where N_{qq} is the number density of AGN pairs in a particular range of separations and N_{qr} is the equivalent number density of AGN/random pairs, normalized to the total AGN count in the survey catalog.

It is also useful to present the parameter $\bar{\xi}$ by the correlation function integrated over a sphere of a given radius in the redshift space r_{max}(e.g. Shanks & Boyle 1994):

$$\bar{\xi}(r_{max}) = \frac{3}{r_{max}^3} \int_0^{r_{max}} \xi(r) r^2 dr \tag{1.22}$$

Different authors have chosen a variety of values of r_{max}, such as $10h^{-1}$ Mpc(Croom & Shanks 1996), $15h^{-1}$Mpc(La Franca, Andreani & Cristiani 1998) and $20h^{-1}$Mpc(Croom et al. 2001).

It has also been found that the correlation function has a power-law shape and evolution with the redshift(La Franca, Andreani & Cristiani 1998):

$$\xi(r,z) = (\frac{r}{r_0})^{\gamma}(1+z)^{-(3-\gamma+\epsilon)} \tag{1.23}$$

Since the clustering of AGNs also provides the detailed information on the distribution of dark matter halos whose gravity governs the overall cosmic evolution, the bias factor b(r,z) is used to explain the difference between visible structures and invisible matter. The complex relation is summarized by the following formula(Grazian et al. 2004):

$$\xi(r,z) = b^2(r,z)\xi_m(r,z) \tag{1.24}$$

where $\xi(r,z)$ and $\xi_m(r,z)$ are the correlation functions of radiating objects and dark matter respectively. Myers et al. (2005) have shown that bias increases rapidly with redshift from $b \sim 1.2 - 1.3$ at $z = 0.75$ to $b \sim 3$ at $z = 2.2$. This clustering evolution of photometrically-classified QSOs is in good agreement with the spectroscopic result of Croom et al. (2005).

1.5 Why Beginning with GOODS

As mentioned in the Section 1.2, the Press-Schechter mass function provides the distribution of the large scale structure and predicts the evolution of the galaxies and AGNs. Hierarchical model(White & Rees 1978) assumes that the small dark halos which are perturbed by density fluctuations dominate the early universe. The formation of spiral galaxies is thought to occur in the virialized halos at higher redshift. Then, these small dark halos merge each other and turn into the big ones, while inside these small halos the spiral galaxies also turn to be massive elliptical galaxies by merging process at low redshift.

However, the faint populations at high redshift are poorly understood. Haiman & Loeb (1998) have explored that the faint AGNs may be linked with the low-mass dark halos. It predicts a large number of low luminosity objects at high redshift. These dim systems(e.g. Schirber & Bullock 2003) in the small halos may suffer all kinds of feedback which is investigated in

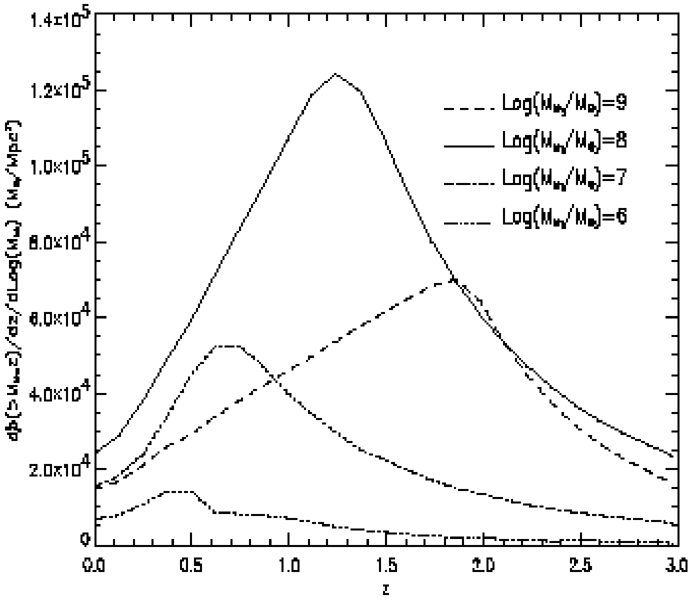

Figure 1.7: The SMBH Mass Function as a Function of Redshifts

the section 3.1.5. These models and tests need to be supported by the deep and multiwavelength observations.

On the other hand, there is growing evidence that massive objects at high redshift are far numerous than predicted by the hierarchical model. For example, the contributions to the local super massive black hole(SMBH) mass function as a function of redshift are investigated using hard X-ray luminosity function(Shankar et al. 2004). The result is shown in the Fig. 1.7. It presents the baryon structure formation oppositely to the hierarchical model. From the observational view, if those massive galaxies and AGNs do exist at high redshift universe, they may be reddened or obscured by the dust so that they are too faint to be detected. Therefore, in the thesis, the Great Observatories Origins Deep Survey(GOODS), nowadays one of the deepest observations, has been used to do multiwavelength survey and thus identify those faint galaxies and AGNs to constrain the models of galaxy formation and evolution.

Chapter 2

High-Redshift AGN in GOODS

In this chapter, the major observational results of seeking high-redshift AGNs ($z \geq 4$) are presented in detail. Firstly, the reasons for selecting an optical faint sample are illustrated in the Section 2.1. The GOODS project, one of the deepest multi-wavelength surveys nowadays available, is introduced in the Section 2.2. Then, the AGN selection methods used in the GOODS are emphasized in the Section 2.3 and the GOODS database used in the thesis is described in the Section 2.4. Optical selection methods(colors and morphology), as the key point for the whole searching strategy in this thesis, are explained carefully in the Section 2.5. The addition of near infrared photometry is described in the Section 2.6. In the Section 2.7, the color-color diagrams of selection candidates are shown. The optical spectra used for the final AGN identification are given in the Section 2.8. Compared to the optical method, X-ray selection is described in the Section 2.9. The improved methods of color selection are added in the Section 2.10. Finally, the latest results for the luminosity function are shown in the Section 2.11. Thus, given the observational data catalogs, the whole process for searching the high redshift AGN are fully exhibited. As the final aim of the strategy, the optical luminosity function of high redshift AGN is extended to its faint end.

2.1 Scientific Goal

The AGN observations play a vital role in investigating the growth of massive black holes and their co-evolution with galaxies. Searching high redshift AGNs is the first step to catch them in the early phases of their evolutionary history and establish a connection with the formation of galactic structures.

Recently, the Sloan Digital Sky Survey(SDSS) has produced a breakthrough, discovering AGNs up to $z = 6.43$ (Fan et al. 2003) and building a sample of six QSOs with $z > 5.7$. The SDSS, however, is sensitive only to very luminous QSOs($M \leq -26.5$) and provides no information about the faint end of the high redshift QSO luminosity function, which is particularly important to understand the interplay between the formation of galaxies and the low-mass dark matter halos, where the feedback processes from the star formation and/or AGNs energy ejection are particularly influenced, and to measure the QSO contribution to the UV ionizing background(Madau, Haardt & Rees 1999).

It is also important to study the Spectral Energy Distribution(SED) of AGNs in various regimes of redshift and bolometric luminosity in order to disentangle the mechanisms of generation of the energy and its reprocessing. For example, in Figure 2.1, we can see the relationship between the X-ray and optical flux for AGNs at $z \sim 4.7 - 5.4$, mostly taken from the SDSS (Vignali et al. 2003). A relatively tight correlation is found indicating that the same engine(namely accretion onto a supermassive black hole) is powering the ultraviolet and X-ray emission. Beside this, the optical to X-ray slope α_{ox}, which can be defined as:

$$\alpha_{ox} = \frac{log(f_{2kev}/f_{2500\mathring{A}})}{log(\nu_{2kev}/\nu_{2500\mathring{A}})} \tag{2.1}$$

where$f_{2500\mathring{A}}$ and f_{2kev} are the rest-frame densities at 2500$\mathring{A}$ and 2keV respectively, does not show significant variations between high and low redshift, suggesting that the mechanism driving the QSO broadband emission is similar in the local and early universe.

From Chandra observation of the optical selected sample at high redshift, it has been found that the ratio of X-ray to optical flux is to be

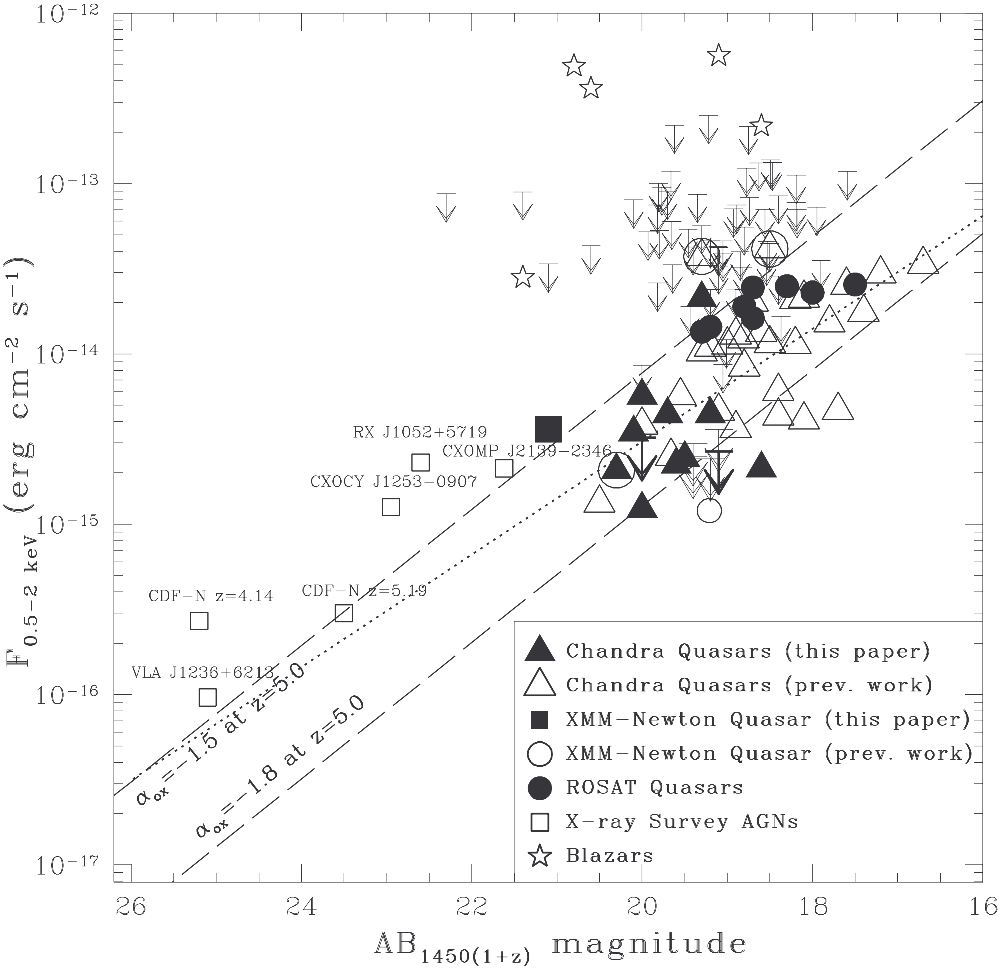

Figure 2.1: Relationship between X-ray and optical flux of high-redshift AGN from Vignali et al. 2003. Object types are shown in the key. In particular, filled triangles are Chandra detections, a filled square is an XMM detection and CHANDRA RLQs are plotted as circled triangles. The large, thick, downward-pointing arrows indicate the X-ray upper limits and the ROSAT upper limits symbolized by the small downward-pointing arrows are at the 3σ confidence level. The slanted dashed lines show the α_{ox}=−1.5 and α_{ox}=−1.8 loci at $z = 5.0$ which is the average redshift of the QSOs in this plot. The dotted line shows the best-fit correlation for the whole sample of $z \geq 4$ optically selected RQQs.

strongly anti-correlated with the redshift and weakly dependent on the luminosity(Bechtold et al. 2003). However, it is apparent in Fig. 2.1 that very few data are available at faint fluxes($AB_{1450(1+z)} \leq 22$) and deeper observations are needed to test the validity of the Vignali relation in this regime.

A number of multi-wavelength observations of deep fields are becoming available in recent times. Here, we will concentrate on the possibility offered by the Great Observations Origins Deep Survey (GOODS).

2.2 Characteristics of GOODS

The Great Observatories Origins Deep Survey (GOODS) is a campaign to unite extremely deep, multi-wavelength observations to create a data set for exploring the distant universe. It surveys approximately 320 $arcmin^2$ divided into two fields: the Hubble Deep Field North(HDF-N) and the Chandra Deep Field South(CDF-S). Each field is about $10' \times 16'$. GOODS is deeper than SDSS and covers a much smaller area than SDSS but significantly larger than HDF. The GOODS field layout[1] is shown in the Figure 2.2 and Figure 2.3.

For this general purpose, GOODS links nowadays the most powerful telescopes, including both space telescopes and ground-based telescopes to carry out the deepest and the most sensitive observation(Dickinson et al. 2003). In this section, brief description is summarized.

The instruments are listed below:

(1) Space telescopes include Hubble Space Telescope(HST), Chandra, XMM-Newton and Spitzer Space Telescope;

(2) Ground-based Facilities involved are Very Large Telescope(VLT) of ESO, Keck Telescope, Hawaii KPNO and CTIO-4m telescope, VLA, SCUBA, etc.

The main scientific projects with GOODS are:

(1) The assembly of galaxies including stellar masses and populations, star formation, galactic evolution and identification of high redshift objects;

(2) AGN research, especially for identification of obscured AGN;

(3) Source counts and extragalactic background;

---

[1] cited from the web-page of www.eso.org/science/goods/fields.html

(4) Large scale structure and dark matter research.

Initial results of the GOODS observations have been presented by Giavalisco et al.(2004a). High redshift galaxies at redshift $z \sim 6$ have been studied(Dickinson et al. 2004); The fundamental properties of the Lyman break galaxies have been investigated(Idzi et al. 2004); The physical formation of Hubble sequence have been proposed by searching the proto-disks and proto-ellipticals(Conselice et al. 2004); Identification the supernova type Ia at redshift $z > 1$ and constraint on the dark energy evolution have been done(Riess et al. 2004); The space density of the high redshift QSOs have also been initially assessed(Cristiani et al. 2004a).

2.3 AGN Selection Strategy in GOODS

In the Chapter 1, the general methods of AGN selection are mentioned. Here we focus on the specific selection strategy in the GOODS. The two common ways for selecting high redshift AGNs are:

- The X-ray selection:

  X-ray deep surveys $\longrightarrow$ Sources detection $\longrightarrow$ Identification Optical/IR corresponding sources $\longrightarrow$ follow-up spectroscopy $\longrightarrow$ X-ray luminosity function.

  Examples of this type of approach are given in Ueda et al.(2003) and specifically for the GOODS-South field, in Szokoly et al.(2003).

- The optical selection:

  Optical deep survey $\longrightarrow$ Color selection of candidates $\longrightarrow$ Follow-up spectroscopy $\longrightarrow$ Optical luminosity function.

The two selections are different and relatively independent so that the corresponding results do not necessarily coincide. As an example one can compare the results of the optical selection carried out in the 2dF QSO Redshift Survey(Croom et al. 2004) with the X-ray selected samples(Ueda et al. 2003). Clearly, in general, optical selection techniques tend to be less sensitive to low-luminosity objects, where the effects of stellar dilution can

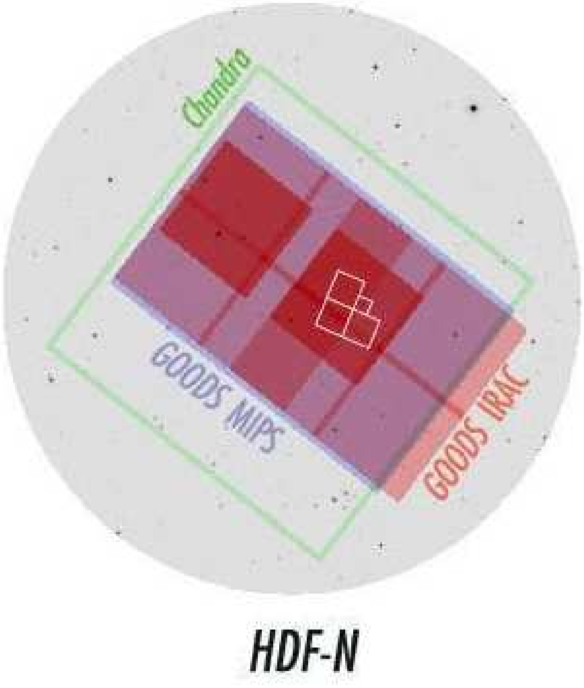

Figure 2.2: The layout of HDF-N

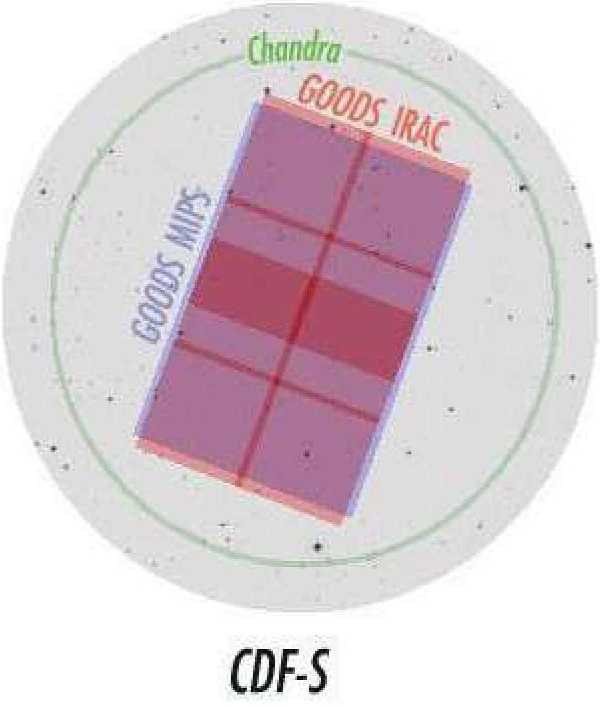

Figure 2.3: The layout of CDF-S

be large (Moran, Filippenko & Chornock 2002). Moreover, absorption effects may affect optical data much more strongly than hard X-ray observations. Conversely, reaching faint X-ray fluxes can be technologically much more demanding than carrying out deep optical observations. Recently, it is noticed that at low redshift selection by optical line emission recover most AGN selected by hard X-ray while selection by hard X-ray might lose a significant fraction of highly obscured Compton-thick population with optical emission lines(Heckman et al. 2005). On the other hand, three unobscured QSOs selected by ROSAT survey has also been confirmed from the optical spectra as type 2 population(Wolter et al. 2005). It is therefore important to explore complementary selections and compare results obtained with different techniques in order to obtain a view of the AGN luminosity function possibly unaffected by selection biases. The GOODS allows us to adopt this multiple approach. In this thesis, the optical selection of high redshift AGNs has been operated independently, then, the results are compared with the sources obtained by X-ray selection.

2.4 Database

As listed in the section 2.2, there are more and more instruments and observations involved in the GOODS project. Among those plentiful resources, the database used in this chapter are introduced below.

The optical photometry data have been obtained with the Advanced Camera for Surveys(ACS) onboard HST as described in Giavalisco et al. (2004a). The HST/ACS observations consist of imaging in F435W, F606W, F775W and F850LP passbands. The total exposure times are 7200, 3040, 3040 and 6280 seconds with the magnitude limits(10σ point source sensitivity within aperture 0.2 arcsecond) of 27.8, 27.8, 27.1 and 26.6 mag respectively. The catalogs for selection of high redshift AGNs have been generated using the SExtractor software(Bertin & Arnouts 1996), performing the detection in the z_{850} band first, then using the isophoto defined as apertures for photometry in the other bands(the so-called “dual-image mode”).

The HDF-N and CDF-S fields have X-ray observations of 2 and 1 Ms respectively(Alexander et al. 2003, Giacconi et al. 2002), providing the deepest views of the universe in the 0.5-8kev. The flux limit($S/N = 5$) is $1.7 \times 10^{-16} erg cm^{-2} s^{-1}$ of 0.5-2kev and $1.2 \times 10^{-15} erg cm^{-2} s^{-1}$ of 2-8kev in the north field, $2.2 \times 10^{-16} erg cm^{-2} s^{-1}$ of 0.5-2kev and $1.5 \times 10^{-15} erg cm^{-2} s^{-1}$ of 2-8kev in the south field.

The deep multi-color imaging survey(Capak et al. 2004) of Hawaii 2.2m telescope provides the near infrared catalog to the GOODS in the HDF-N. The survey area of the infrared HK' band is $0.11 deg^2$, which is lager than the area of the ACS and the limit magnitude of HK' band is about $22.8(5\sigma)$. For the CDF-S, near infrared imaging observations are being carried out in J, H, Ks bands, using the Infrared Spectrometer And Array Camera(ISAAC) instrument mounted in VLT at ESO. This data release includes 21 fully reduced VLT/ISAAC fields in J and Ks bands and 12 fields in H band , covering 131 $arcmin^2$ of the GOODS/CDFS region.

The catalogs of optical spectroscopy are also including in the database. In the HDF-N, using Deep Imaging Multi-Object Spectrograph (DIMOS) and the Low-Resolution Imaging Spectrometer(LRIS) on the Keck II telescope, the treasury redshift survey(Wirth et al. 2004) with the magnitude limit of $R_{AB} = 24$ has been carried out and a large extensive sample has been obtained(Cowie et al. 2004). In the CDF-S, the optical spectroscopic follow-up program compiles the spectral catalog(Szokoly et al. 2003) particularly for both type 1 and type 2 AGNs.

2.5 Optical Selection

2.5.1 Color Characteristics

Optical photometry survey, with high efficiency, offering not only the huge number of sources but also abundant sorts of objects in the sky, gives the astronomers the excellent chance to choice the special type which they are peculiarly interested. In this section, the B(F435W), V(F606W), i(F775W) and z(F850LP) passband images of HST/ACS deep survey[2] are available. Of these deep images, there are at least three objects included: stars, galaxies

---

[2] The details of HST/ACS observation are described in the Appendix A.1

and AGNs. Therefore, selection methods adopted to distinguish among them are needed.

Our aim is to select AGNs within the magnitude interval $22.45 < z_{850} < 25.25$ of the redshift range $3.5 < z < 5.2$ from those images. The optical magnitudes(B, V, i and z) of each source in those images have been measured by the SExtractor[3]. The different kinds of objects at different redshifts may have different optical colors so that it is possible to use the special colors which are extremely sensitive to AGNs to constrain the objects and select the AGN candidates.

The outline of this selection method is the following:

Different spectra properties at different redshift $\longrightarrow$ Color characters $\longrightarrow$ Color selection criteria $\longrightarrow$ Optical photometry candidates

The description above is so-called Lyman-break technique(Steidel & Hamilton 1992; Steidel et al. 1996) which is widely used in the deep surveys for search high redshift AGNs and galaxies. The similar photometry redshift technique is also considered both in the HDF-N and CDF-S(Arnouts et al. 1999, 2002). In this section, in order to explain this selection method clearly, the example is given below.

Three spectra of typical high redshift AGN accompanying with the B, V, i and z passbands of HST/ACS are shown in the Figure 2.4, 2.5 and 2.6. The spectra have been handled by three steps: Initially, the optical composite spectrum emitted from the AGNs which shine in the local universe is needed. Composite quasar spectrum from SDSS(Vanden Berk et al. 2001) is an good example. In this context the template spectrum taken from Cristiani & Vio (1990) is selected to be the target; Then, this spectrum can be extended in the region shortward of the Lyman α emission with a power law continuum $f_\nu = \nu^{-0.7}$; Finally, the spectrum is multiplied by the transmission of the intergalactic medium for the sake of moving it into high redshift universe, assuming that the continuum and emission lines do not have evolution with redshift. In general, the emission of higher redshift AGN may transmit through more HI clouds to arrive the place of the observer so that the spectrum has shown more powerful Lyman alpha absorption.

Therefore, taking into account the absorption and redshift effects, in the

---

[3] The optical photometry is described in the Appendix A.2.

Figure 2.4, the absorbed part of the spectrum at redshift 3.5 begins to fall into the B band in the observer's frame. When the spectrum shifts to the redshift 4.5 in the Figure 2.5, the flux in B band is fully absorbed. If the spectrum continually moves toward redshift 5.0 in the Figure 2.6, the fluxes of both B and V band are strongly absorbed by Lyman α forest.

In the images of Figure 2.7, we see that the high redshift AGNs are shown in the i and z band because the fluxes in those bands avoid the Lyman α absorption. On the contrary, the AGNs in the V band are so faint and those in the B band even disappear due to the absorption catastrophe.

From this example, we see, the different passband fluxes affected by the Lyman α absorption at different redshifts provide the diversities of the spectra and colors. This kind of property gives us the hint for making the color criteria to pick out the AGNs harbored at high redshift universe among various objects in the survey images and thus determining the photometry redshift values.

By quantification, a set of color selection criteria has been elaborated in order to select AGNs at progressively higher redshift in the range between 3.5 and 5.2(Cristiani et al. 2004a):

$$i - z < 0.35 \quad \text{AND} \quad 1.1 < B - V < 3.0 \quad \text{AND} \quad V - i < 1.0 \tag{2.2}$$

$$i - z < 0.35 \quad \text{AND} \quad B - V > 3.0 \tag{2.3}$$

$$i - z < 0.5 \quad \text{AND} \quad B - V > 2.9 \quad \text{AND} \quad V - i > 0.8 \tag{2.4}$$

$$i - z < 1.0 \quad \text{AND} \quad V - i > 1.9 \tag{2.5}$$

These selection criteria are purposefully less stringent than those typically used to identify high redshift galaxies, since our goal is to identify a complete sample of high redshift QSOs. In particular, the selection criteria identify a broad range of high AGN, not limited to broad-lined(type-1)QSOs. Beyond the redshift $z \simeq 5.2$ the i-z color starts increasing and infrared bands would be needed to efficiently identify QSOs with an "i-dropout" technique. Below $z \simeq 3.5$ the typical QSO colors in ACS bands move close to the locus of stars and low redshift galaxies. QSOs with $z \geq 5.2$ or $z \leq 3.5$ may still be included in our selection as a consequence of photometric errors or peculiar SEDs. The criteria have been applied independently and produced four lists

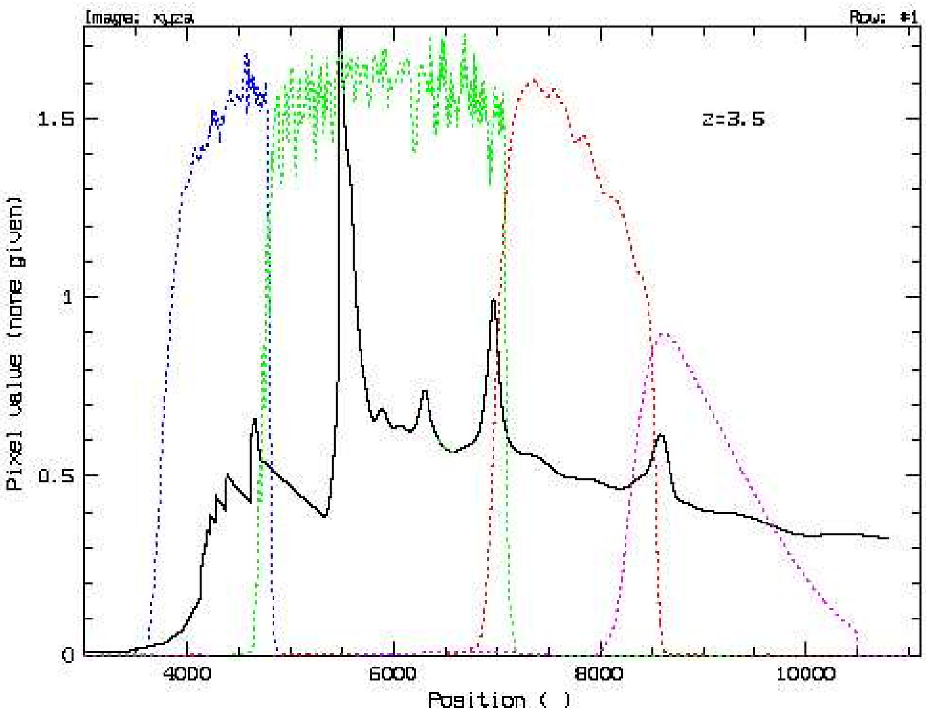

Figure 2.4: The AGN spectrum at redshift 3.5. The flux of the spectrum has arbitrary unit.

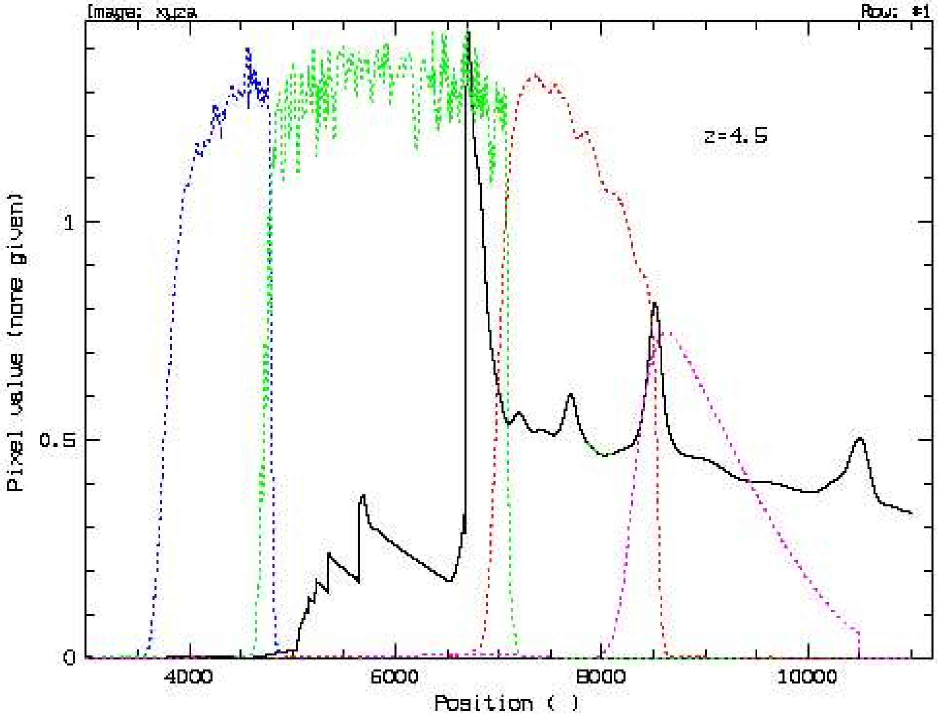

Figure 2.5: The AGN spectrum at redshift 4.5. The flux of the spectrum has arbitrary unit.

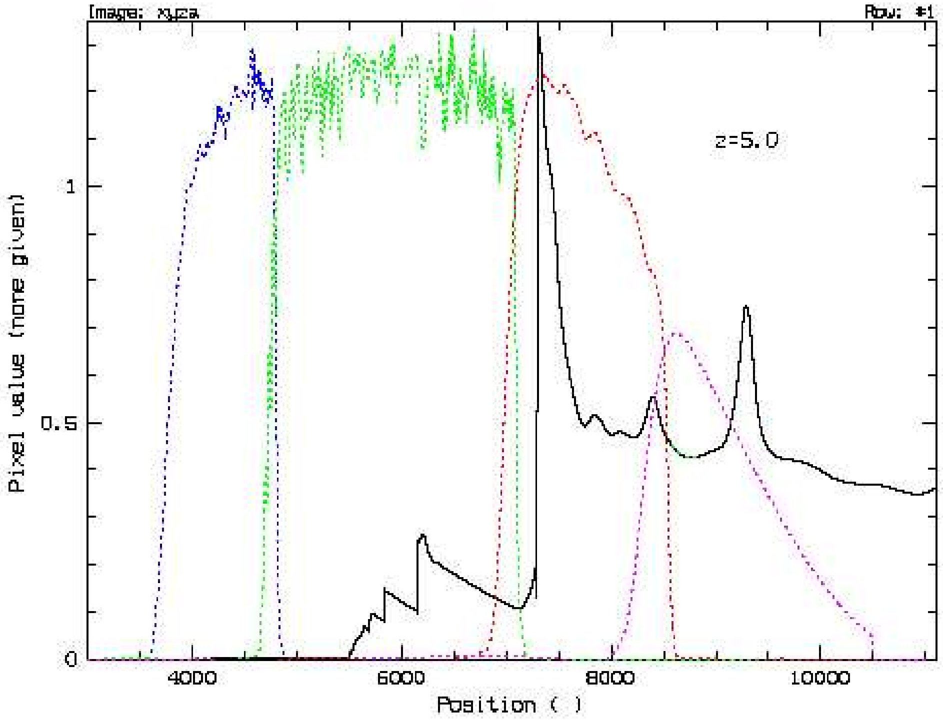

Figure 2.6: The AGN spectrum at redshift 5.0. The flux of the spectrum has arbitrary unit.

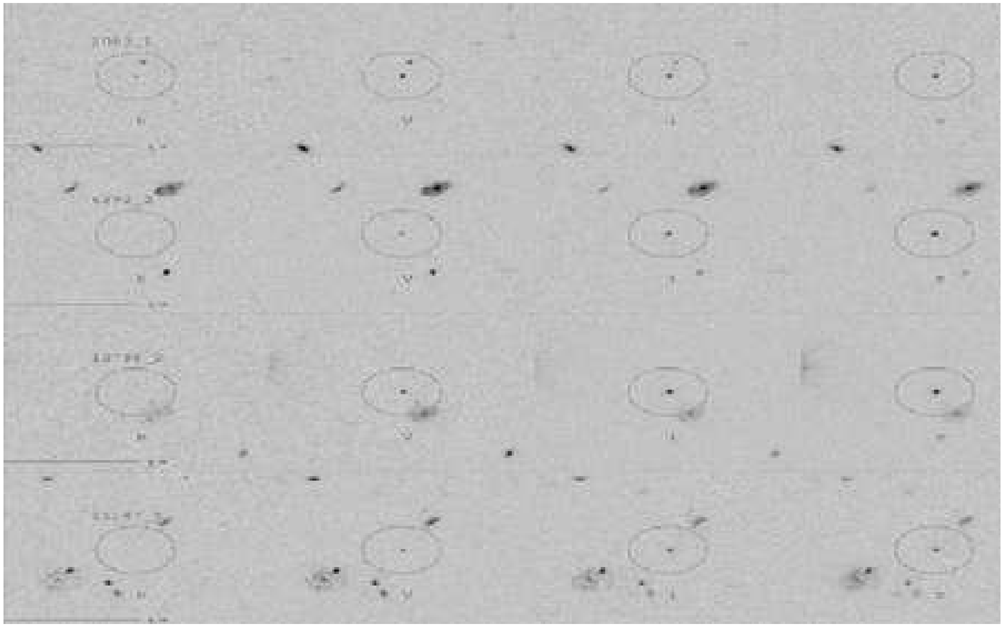

Figure 2.7: The four high redshift AGN samples(same object lies in the horizontal grids) presented in B, V, i, and z band(vertical grids respectively).

with objects in common. After merging the lists, in the HDF-N, we have 557 candidates, and in the CDF-S, 645 candidates are selected.

2.5.2 Colors and Morphology

For assurance of completion, the color criteria might select all AGN candidates which are contented with the color characters mentioned above. However, among those candidates, although most of them have similar colors of high redshift AGN, they are not AGNs at all. Before the spectral identification, morphology as an additional condition has been taken into account since the high redshift AGNs look like the points while local galaxies are elliptical or spheroidal. Thanks for the SExtractor, it gives the certain parameter to describe the shape of each object. Thus, we can distinguish the high redshift AGNs from the local galaxies using morphology selection. Practically, the optical selection used in this thesis is the coalition with colors and morphology together. As the conclusion, from the B, V, i and z band deep survey of HST/ACS, after optical selection, we have obtained the high redshift AGN candidates, 25 in HDF-N and 29 in CDF-S.

2.5.3 Discussion

The high redshift candidates have been selected from the optical survey data. Consequently, it is needed to give the roughly statistic distribution of these candidates in each passband. As an example, in HDF-N, the distributions of high redshift AGN candidates in B, V, i and z band are shown respectively in the Figure 2.8, 2.9, 2.10 and 2.11. The limit magnitudes of B_{435}, V_{606}, i_{775} and z_{850} of HST/ACS are 27.8, 27.8, 27.1 and 26.6 respectively for 10σ point source sensitivity with aperture 0.2".

The candidates seen in V, i and z band are so faint, nearly reaching the magnitudes limit. However, in the Figure 2.8, most candidates in the B band are distributed below the limit magnitude. These suspicious values are produced by the so-called dual-image mode(Vanzella et al. 2001) of SExtractor for the magnitude measurement. The procedure is: The B, V, i and z images are firstly obtained in the ACS deep survey; Then, the z band image which is the reddest one is chosen as the elementary mode; After the magnitudes of objects in z band have been measured, the corresponding positions of the objects in the other bands can be decided with the same isophoto apertures; Finally, based on these positions, the photometry in B, V and i band can be carried out.

During this procedure, suppose one source is measured in the z band but its fluxes in the other bands are too weak, the SExtractor will still give it the magnitude values in other bands which are below the limit magnitudes of ACS. This is the possible situation in the optical selection since generally the high redshift AGNs are faint objects and the B band fluxes of the high redshift AGN candidates are particularly weak due to the strong absorption of Lyman α forest. Thus, the optical selection candidates measured in B band by Sextractor contain much larger uncertainties, those values are unreliable.

2.6 Near-IR Magnitudes

The infrared radiation, as one part of SED for AGNs, gives us the evidence to understand the radiative process through the central energy released by the black hole accretion regime thus investigate the AGN structure and confirm the unified model. It is assumed that near infrared light, produced by dust reprocessing of the primary optical-UV emission, is original from the torus which is around the central black hole and supported by radiation pressure(Pier & Krolik 1992). The torus is proposed to be compact and extremely thick(Pier & Krolik 1993) or moderately thick and extended(Granato & Danese 1994). It could be also interesting to study the infrared emission of AGNs at high redshift universe.

On the other hand, from the high redshift spectra in the Fig. 2.4-2.6, it is shown that a part of AGN continuum is strongly absorbed by Lyman α forest. The measurement of the continuum spectral slope in the optical band might include the large error. This uncertainty of the slope will affect the K-correction and make distortion to the luminosity function of high redshift AGN. However, if the near infrared fluxes can be observed, the spectrum will be extended and the uncertainty of the spectral shape will be limited.

For instance, in the HDF-N, we use the the infrared catalog from Hawaii deep multi-color imaging survey(Capak et al. 2004). The data are observed

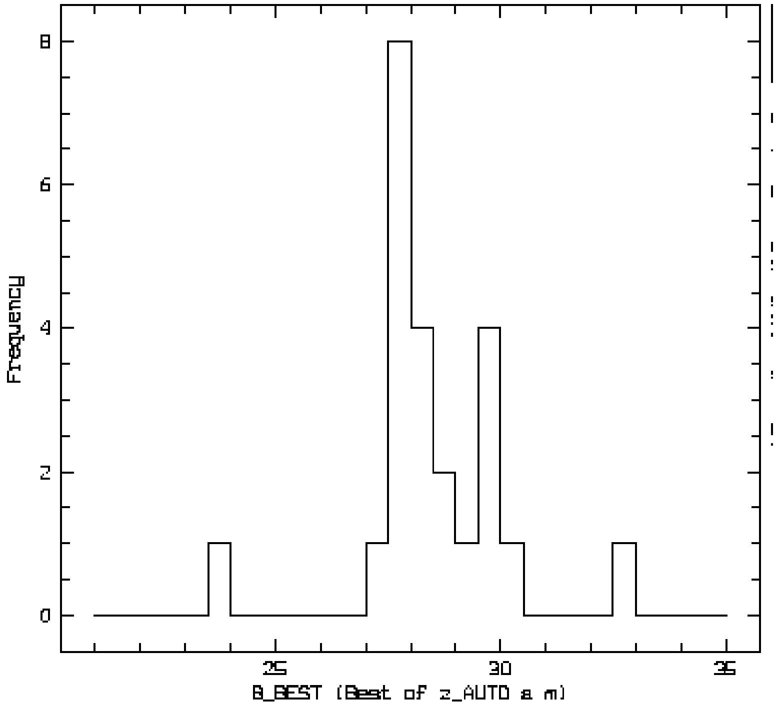

Figure 2.8: The candidates distribution of B band

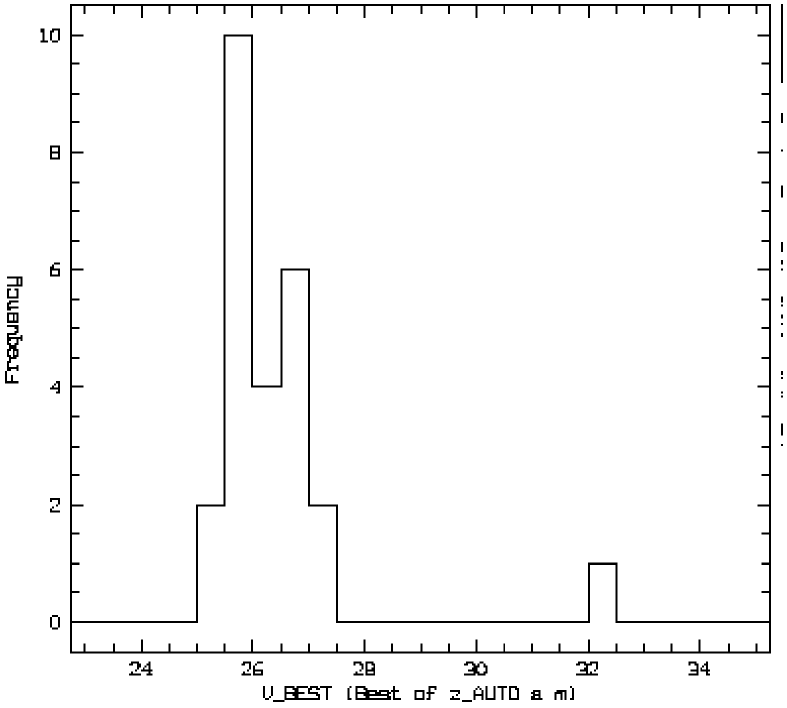

Figure 2.9: The candidates distribution of V band

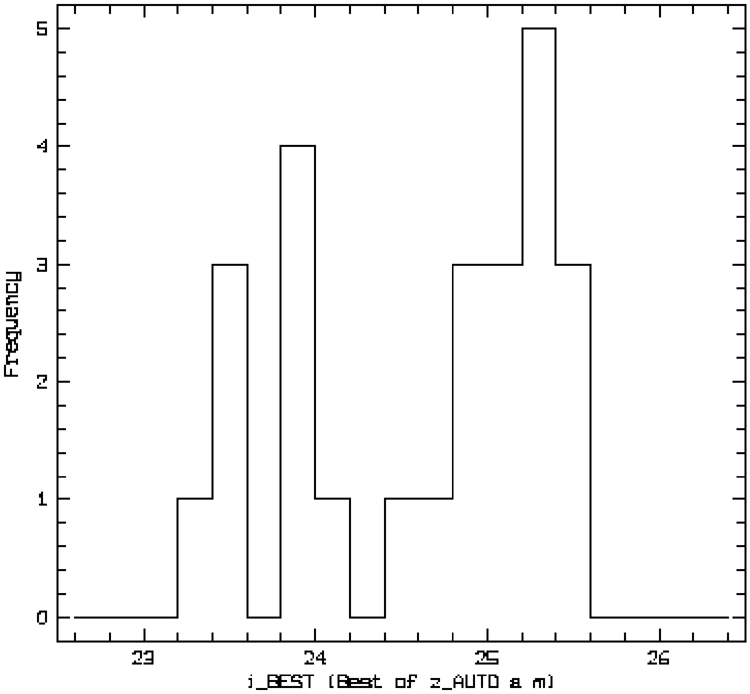

Figure 2.10: The candidates distribution of i band

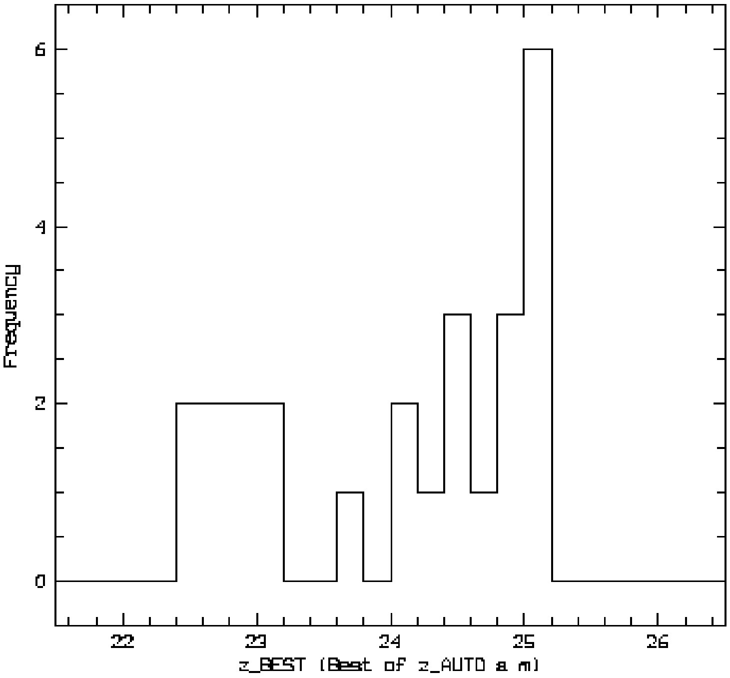

Figure 2.11: The candidates distribution of z band

by the University of Hawaii 2.2m telescope. The catalog is divided into R and z' part. The survey area of the infrared HK' band is $0.11deg^2$, which is lager than the area of the ACS deep survey of HDF-N and the limit magnitude of HK' band is $22.8(5\sigma)$.

The objects have been measured independently by the infrared and optical band respectively. Therefore, matching the sources in the two catalogs needs to compare the coordinates of them in the two images(infrared one and optical one). Actually, the key point is to decide the proper matching radius which is around the center of coordinates for each object in optical image. The infrared point falling within the proper radius can be viewed as the counterpart. The processes are listed below:

(1) Take an initial matching radius;

(2) Compare the coordinates of each object in the two images and get the difference of the coordinates, which are named DRAC(difference of RA) and DDEC(difference of DEC);

(3) The distribution of DRAC and DDEC should be Gaussian, otherwise, repeat (1) and (2). For example, in the Fig. 2.12 and 2.13, we have two distribution shapes of DRAC by two matching radius. In the Fig. 2.12, the distribution is not Gaussian due to the bigger matching radius. In the Fig. 2.13, the Gaussian distribution is shown because of taking the proper matching radius;

(4) Take the 3σ of the Gaussian distribution as the new matching radius and get the DRAC and DDEC;

(5) Due to the system error, the Gaussian distribution will have the distortion. For example, in the plane of the DRAC and DDEC shown in the Fig. 2.14, the objects do not scattered around the center. Therefore we need to find the median value of the distribution of DRAC and DDEC and shift the distribution to the center.

(6)Then, we get the corrected DRAC and DDEC. The result are shown in the Fig. 2.15;

(7) Calculate the parameter DIST:

$$DIST = \sqrt{DRAC^2 + (DDEC \times cos\delta)^2} \tag{2.6}$$

and use DIST to be the final matching radius. The distributions of uncor-

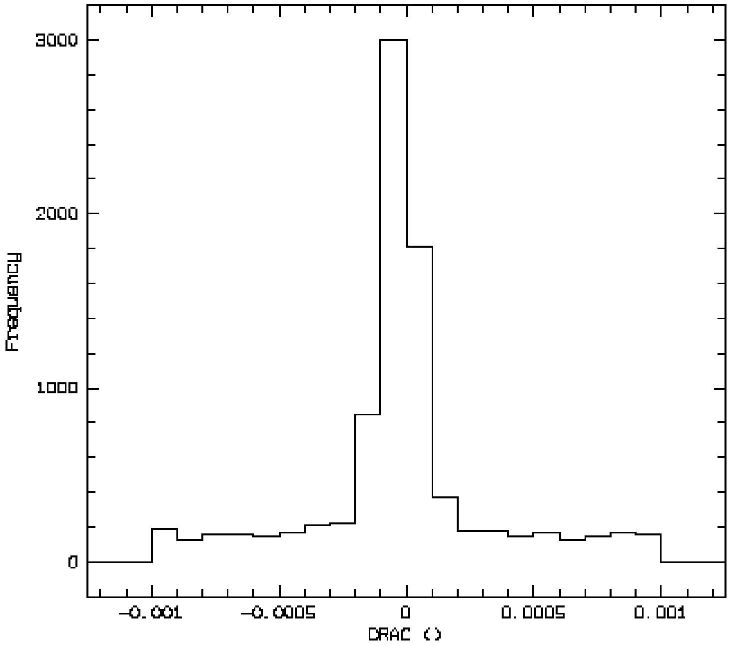

Figure 2.12: The non-Gaussian distribution by the difference of the coordinates with the big matching radius

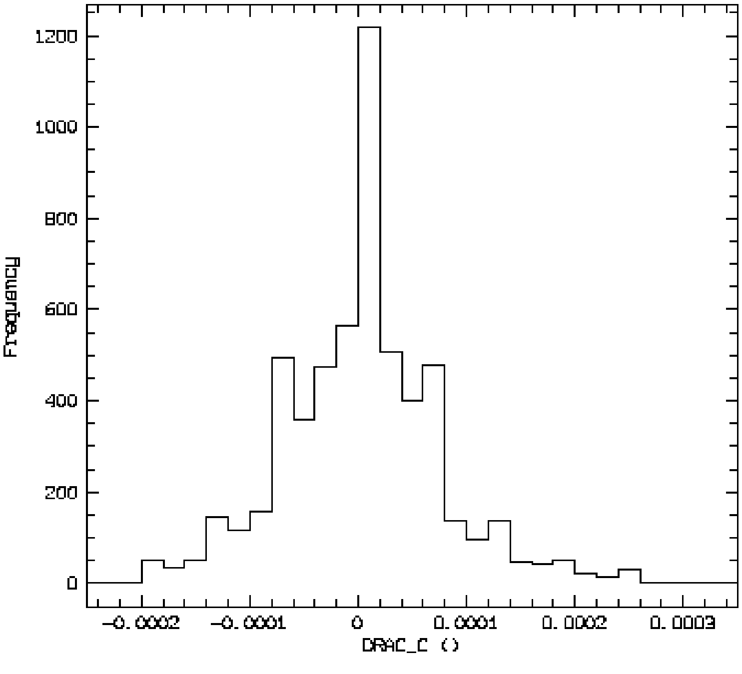

Figure 2.13: The Gaussian distribution by the difference of the coordinates with the proper matching radius

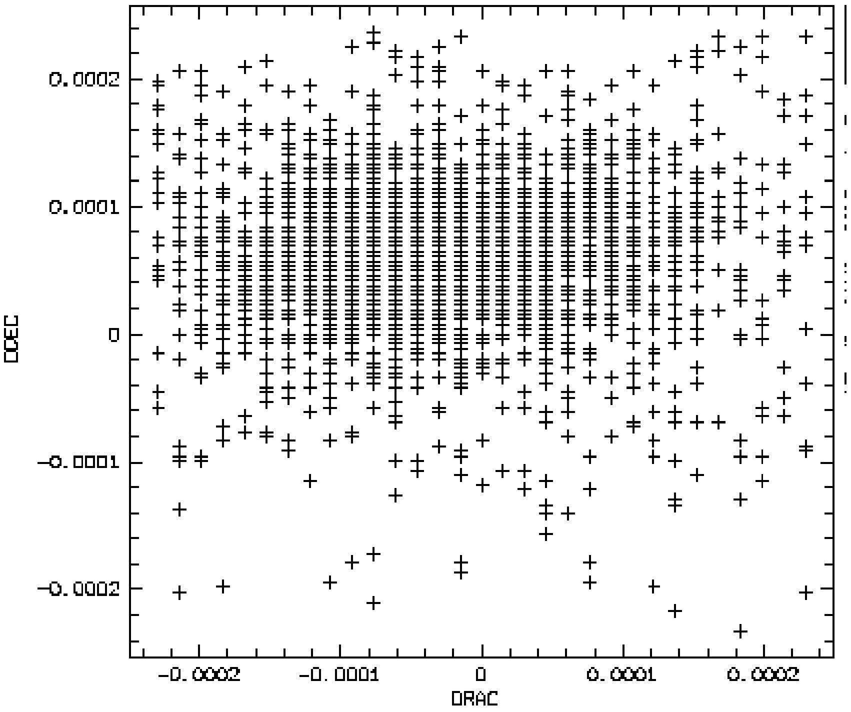

Figure 2.14: the difference of the coordinates which are to be corrected

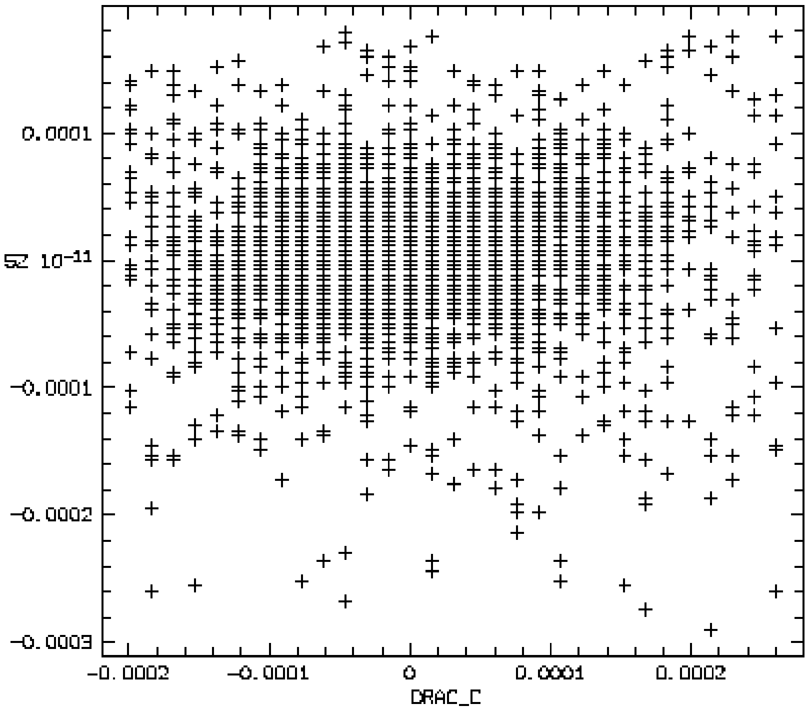

Figure 2.15: The corrected difference of the coordinates

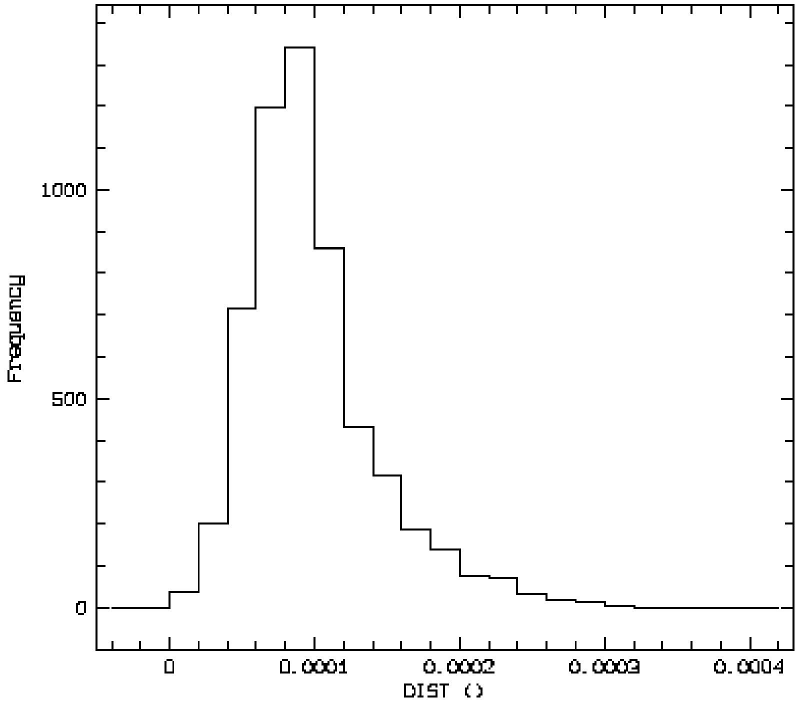

Figure 2.16: the matching radius which is to be corrected

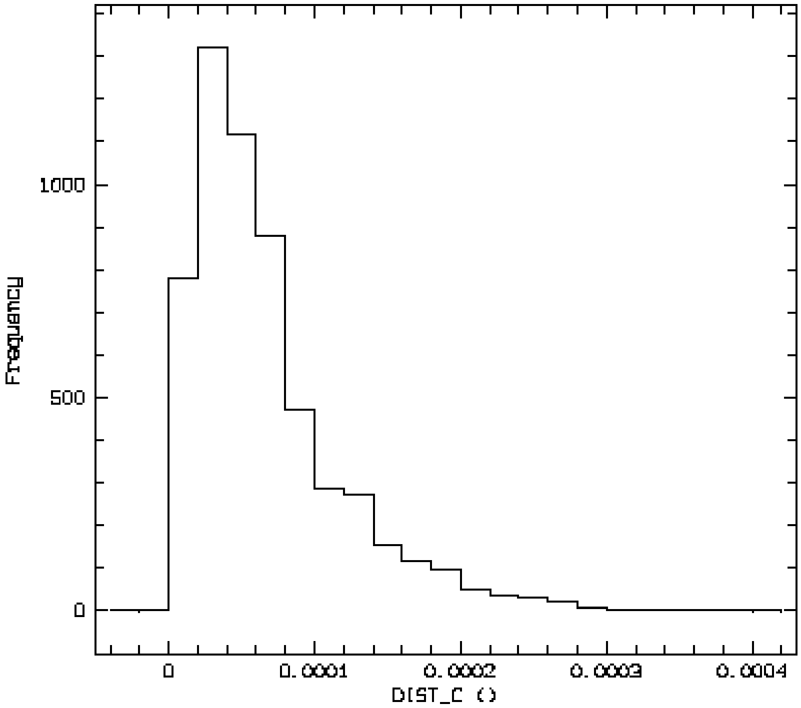

Figure 2.17: The corrected matching radius

rected DIST and corrected DIST are shown in Fig. 2.16 and 2.17 respectively. We can see that the corrected DIST is more accurate than the one that has no correction.

(8) Check the false probability. It is equal to the area of the error-box multiplied by the number of objects per unit area.

The final matching radius ranges from 0.00024 to 0.00039 degree and the false probability is far less than 1 so that the matching radius is reliable. This matching skill presented here is similar to the performance of Padovani et al.(2004).

It is noted that generally the seeing due to the turbulence of the atmosphere in one ground-based observatory is below 1 arcsecond. Therefore, at the beginning of this procedure, we use the seeing value as the initial matching radius to avoid the calculation which may be repeated from (1)-(3) so many times.

2.7 Color-Color Diagram

Before the spectral identification, it is useful to investigate the color characteristics of these high redshift AGN candidates through the color-color diagram and thus deeply understand the color criteria operated in the Section 2.5.

As an example, Fig. 2.18(Cristiani et al. 2004a) shows the clues for the seeking of high redshift AGNs. The objects lie in the upper-left region of the diagram could be M and A stars. The dashed line connecting the triangles shows the expected locus of AGNs at $z \geq 3.5$. The continuous and dotted lines show the colors of Lyman break and Seyfert 2 galaxies, derived from the SEDs of Schmitt et al.(1997) and Arnouts et al.(1999) respectively, convolved with the model of IGM absorption(Madau, Haardt & Rees 1999). The corresponding symbols, open triangles, circles and squares, start on the left at z=3.5 and move to the right in steps of $\Delta z = 0.1$. The observed colors of five QSOs are marked with filled circles and the corresponding redshifts. Thus, the high redshift AGNs are located at the place of the lower-right part which is divided by the dot-dashed line in the diagram.

The similar color-color diagrams can be drawn using the HDF-N results

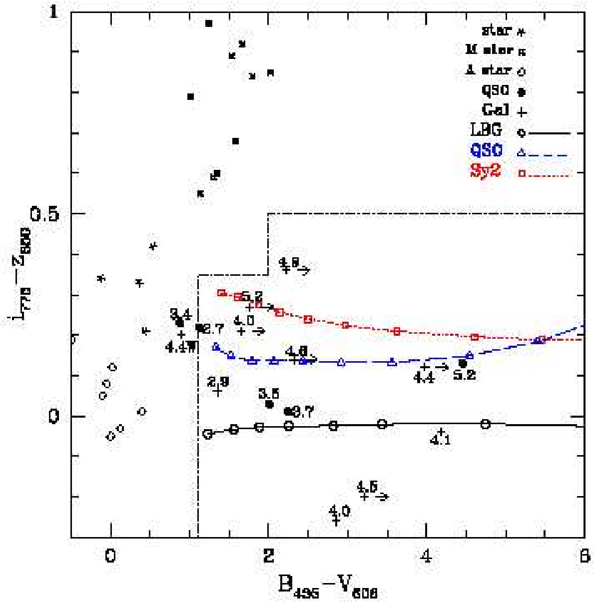

Figure 2.18: An example of color-color diagram for the selection of AGNs at $z > 3.5$

selected from the criteria shown in the section 2.5. Since most HK' band magnitudes have been obtained, the color diagrams can be extended to the near infrared region. To illustrate the color characters of these candidates, B-V vs. i-z (Fig. 2.19), V-i vs. i-z (Fig. 2.20), i-z vs. z-HK' (Fig. 2.21) and V-i vs. z-HK' diagram(Fig. 2.22) are given respectively. It is noted that the infrared magnitudes of 5 candidates have not been found in the nowadays catalog of Capak et al.(2004). The possible reason could be: compared with the ACS deep observation, the emission of those candidates in the IR band are so weak that their magnitudes are too faint and below the limit of the shallow IR survey. Therefore, we take the limit magnitude 22.8(5σ) of HK' band to replenish those candidates which lack the near infrared magnitudes. These candidates are taken arrows to sign the errors in the diagrams.

Despite of the merits above, however, it is noted that the near infrared survey and ACS observation are independent and not consistent with each other to be a whole unit system. Moreover, all the candidates have not been identified with the spectra. Therefore, it is not available to give the clear and meticulous boundary for setting apart AGNs among the candidates in

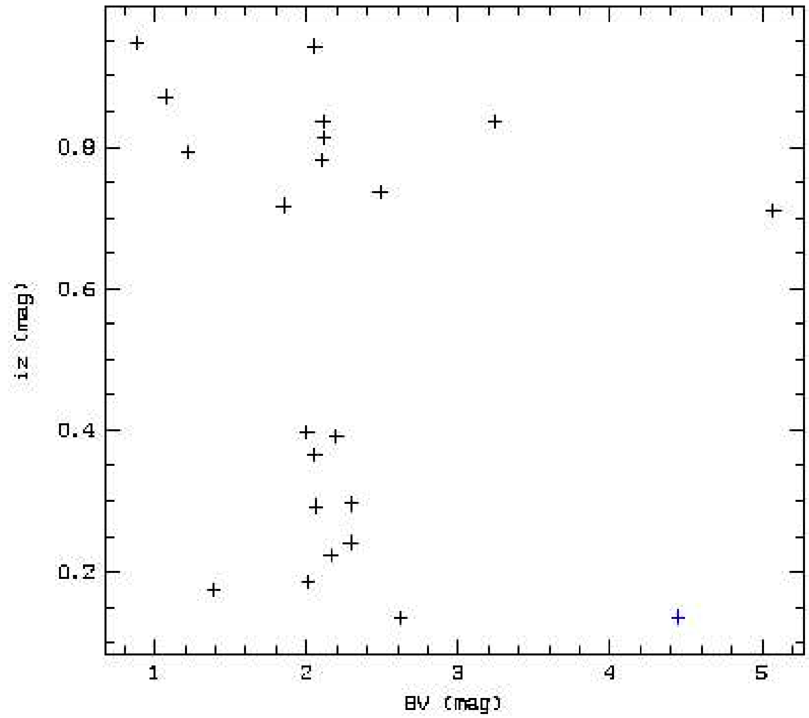

Figure 2.19: The B-V vs. i-z diagram

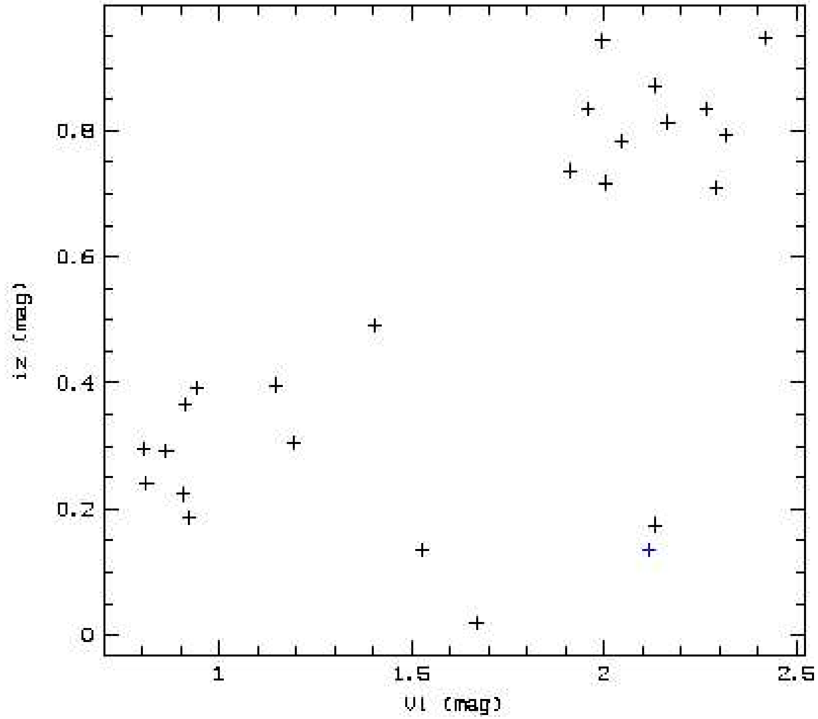

Figure 2.20: The V-i vs. i-z diagram

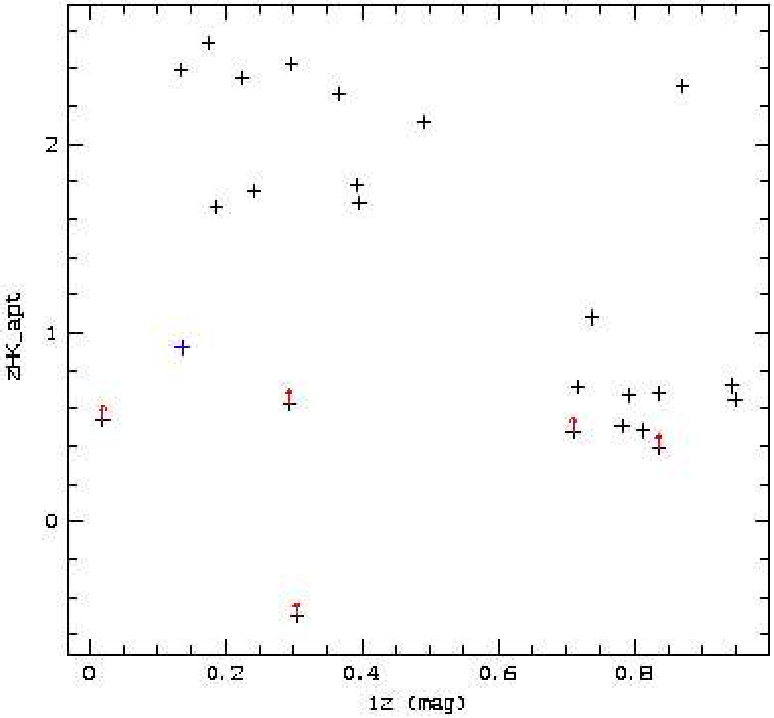

Figure 2.21: The i-z vs. z-HK diagram

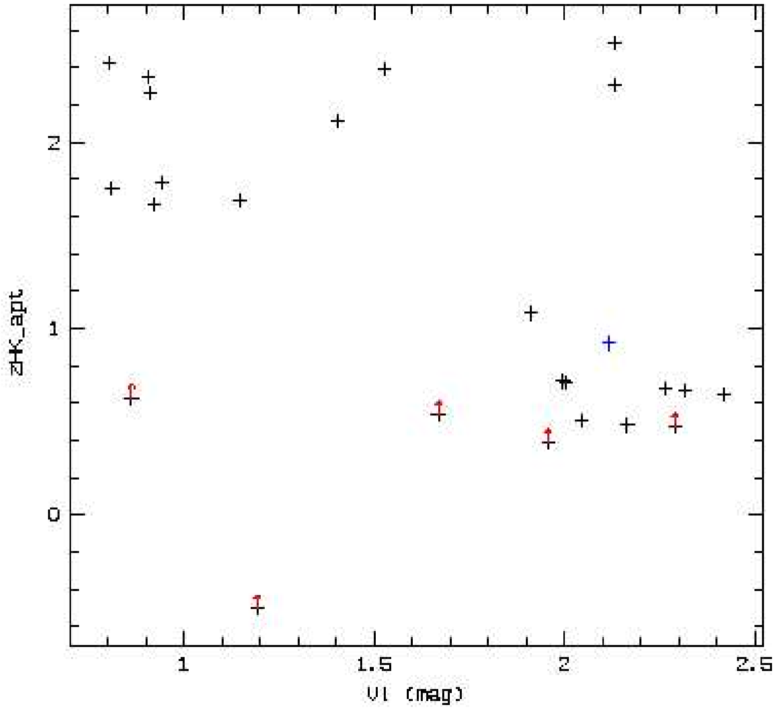

Figure 2.22: The V-i vs. z-HK diagram

those color-color diagrams.

2.8 Spectral Identification

The high redshift AGN candidates obtained by color selection in the GOODS HST/ACS observation need to be identified by the optical spectra using enormous ground-based telescopes[4].

In the HDF-N, the multi-slit spectroscopy has been used by the DEIMOS spectrograph in Keck II telescope(Wirth et al. 2004) which provides the limit magnitude of $R_{AB} = 24.4$. These nowadays high quality data plus the former observations which are centered in the HDF-N(Cohen et al. 1996, 2000; Dawson et al. 2001) give us the possibility to determine the spectral redshifts of our high redshift AGN candidates. In the CDF-S, the spectroscopy survey particularly for the X-ray sources has also been carried out(Szokoly et al. 2003) using VLT FORS1/FORS2 spectrograph with the limit magnitude of $R = 26$.

We search the coordinates of our candidates in the spectral catalogs. This method is similar to the skill used in the section 2.6. Two candidates, one at redshift 5.19 in HDF-N and one at redshift 4.76 in the CDF-S, are defined as AGN.

Table 2.1: High redshift candidates in HDF-N

RAC degree	DEC degree	z mag AB mag	V-i AB mag	i-z AB mag	B-V AB mag	B-z AB mag	K AB mag	z_{sp}	X-ray Flux $ergs/s/cm^{-2}$
189.0075378	62.1934090	25.205	0.83	0.14	2.08	3.07	*	*	*
189.0907135	62.1889038	24.068	2.17	0.81	71.94	74.93	*	*	*
189.1998444	62.1615791	23.761	2.07	0.15	4.81	7.03	*	5.19	0.50×10^{16}
189.2307281	62.2038078	24.098	1.91	0.71	72.27	74.90	*	*	*
189.2992096	62.1926575	25.141	1.51	0.11	72.08	73.86	24.54	*	*
188.0053711	-27.7422810	25.206	2.19	0.15	71.17	73.79	*	*	*
188.0788155	-27.8840961	24.561	2.56	0.63	71.18	74.44	*	*	*
188.0944328	-27.8603153	25.160	1.49	0.47	71.79	73.84	*	*	*
188.1220474	-27.9387398	24.984	1.72	0.14	72.06	74.02	*	4.76	2.72×10^{16}
188.1682701	-27.7419453	25.223	0.53	0.01	3.10	3.75	*	*	*

---

[4] The instruments and methods used in this section are mentioned in the Appendix A.2

2.9 X-ray Selection

Since high redshift AGNs are powerful X-ray sources, except the optical selection, X-ray observation is another useful technique for searching them, especially for detecting the obscured population. The deep X-ray data observed by Chandra (Alexander et al. 2003; Giacconi et al. 2002) are available, we can use X-ray selection to obtain high redshift AGN candidates and carry out the spectral program to identify them. The work in the HDF-N has already been performed by Barger et al. (2003). One high redshift AGN has been confirmed at $z = 5.19$. In the CDF-S, another AGN has been discovered at $z = 4.76$. Both of them are existing in our optical candidates and they are exactly the same AGNs which we select by optical observations.

2.10 Improved Selection Criteria

Before conclusion, it is useful to review the whole process of color selection for high redshift AGNs. The original criteria may select the complete candidates, however, they may not so effective to be strict with the candidates among the numerous objects. In this section, it is proposed to modify the color selection criteria as:

$$i - z < 0.6 \quad \mathrm{OR} \quad \mathrm{non-detected \quad in \quad B \quad band} \tag{2.7}$$

$$i - z < 0.2 \quad \mathrm{OR} \quad B - z > 5.1 \tag{2.8}$$

The new selection results are listed in the table 2.1. The B-V and B-z values larger than 70 indicate that the sources in the B band are so faint and non-detected. These candidates selected by the new criteria are included in the old dataset which selected by the former selection criteria. The coordinates and the colors of the candidates have a minor difference due to the different observation circles of HST ACS(The former one is the circle 12 while the later one is the circle 13). Then we put all the candidates of high redshift AGN both in the HDF-N and CDF-S together and draw the color-color diagram in the Fig. 2.23. The line shows the trace of AGN positions from the low redshift to the high redshift, similar to the Fig. 2.18.

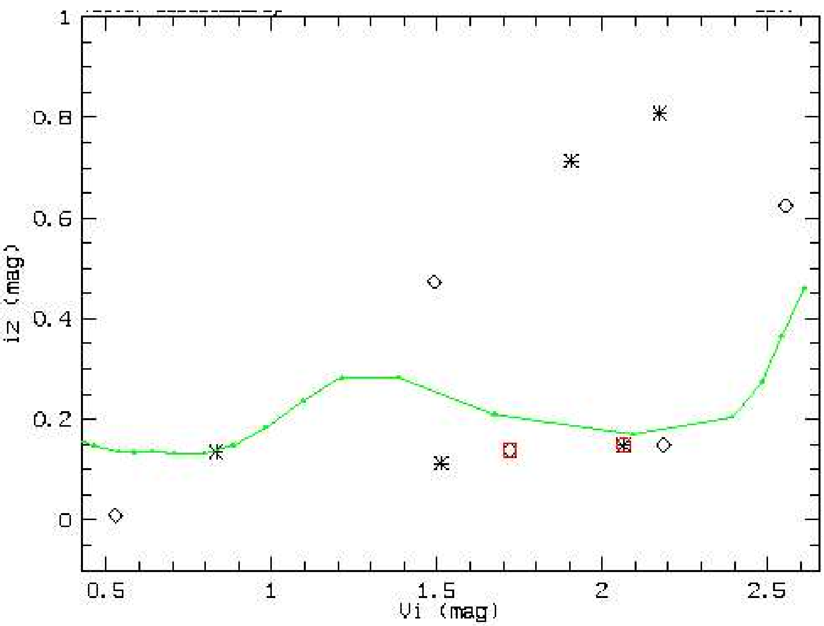

Figure 2.23: V-i vs i-z diagram produced by the new selection criteria. The candidates of HDF-N are marked by stars and the diamond symbols are the candidates in CDF-S.

2.11 Luminosity Function

Based on the observational data of SDSS(Fan et al. 2001), Combo-17(Wolf et al. 2003), the second Palomar survey(Kennefick, Djorgovski & de Carvalho 1995) and the GOODS result, the luminosity function[5] of AGN at $z = 4 \sim 5$ is shown in the Fig 2.24(Cristiani et al. 2004b). The curve has been flattened at the faint end by the GOODS sample. Recently, Fontanot et al. (2006) point out that the pure density evolution model is well agreement with the observations and the QSO contribution to the UV background is insufficient to ionize the IGM at these redshifts.

We assume AGNs are hosted in the newly formed halos with a constant SMBH/DMH mass ratio ϵ and accretion at the Eddington rate. The bolometric luminosity function is given by(Cristiani et al. 2004a):

$$\Phi(L|z)dL = N_{ps}(M_H|z) \int_{t(z)-t_{duty}}^{t(z)} P(t_f|M_H, t(z))dt_f \epsilon^{-1} \frac{dL}{L_{Edd}} \tag{2.9}$$

---

[5] The methods to calculate luminosity function are described in the Appendix B.1.

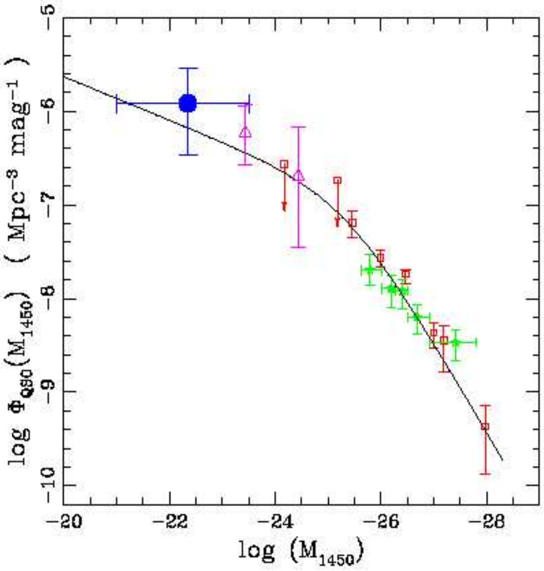

Figure 2.24: The AGN Luminosity function at redshift 4. Squares: data from the Palomar survey at $z \sim 4.4$. Stars: SDSS computed at $3.5 < z < 5$ assuming a power-law decline and rescaled to z=4.3. Triangles: Combo-17 for $4.2 < z < 4.8$. Circle: GOODS data. The solid line shows the prediction of the Pure Density Evolution of double power-law fit of QSO luminosity function by Boyle et al. (2000).

The abundance of DMHs is computed using the Press & Schechter formula. $P(t_f|M_H, t(z))dt_f$(Lacey & Cole 1993) is the distribution of the halo M_H formation at time t_z and $L_{Edd} = 10^{4.53}L_\odot$ is the Eddington luminosity of one $M_\odot$ black hole. Thus the luminosity function above is the space distribution of AGNs which are associated with the dark halos multiplied by the certain probability P during the AGN duty cycle t_{duty}. However, this kind of model is known to overproduce the number of high redshift AGNs(Haiman, Madau & Loeb 1999).

One possible solution(Lidz et al. 2005) is the following: on average bright and faint QSOs reside in similar host halos. The bright end of QSO luminosity function consists of QSOs radiating at their peak luminosities, while the faint end consists mainly of very similar sources, but at dimmer phases in their evolution due to black holes growth. Thus, these bright QSOs spend a significant amount of time at low luminosity stages and already account for the faint end of luminosity function, hence one overproduces the abundance of faint QSOs.

Another explanation to the flattened luminosity function of high redshift AGN is so-called anti-hierarchical baryon scenario (Granato et al. 2004) which will be presented in the following chapter. In that model, at high redshift, the dark matter halo is so small that the shallow potential well can not constrain the strong feedback of AGN and supernova. The AGNs shine with a time delay after dark matter halo formation. Therefore, the space density of AGNs which reside in the low-mass dark halos would be smaller thus the luminosity function would be flattened at the faint end.

It is also noticed that the similar works which pay attention to the low luminosity AGNs at high redshift space are being studied. For example, a survey for low luminosity quasars($M_b < -23.0$) at redshift $z \sim 5$ has been carried out(Sharp et al. 2004). The detect single quasar($4.8 < z < 5.2$) is indicative of a possible turn over in the luminosity function at faint magnitudes.

Thus, from the luminosity function of high redshift AGN, it is shown, at early epochs the AGN formation or the feeding of super massive black hole is strongly suppressed in relatively low-mass dark halo, as a consequence of feedback from star formation and/or photoionization heating of the gas by the UV background, accomplishing a kind of inverse hierarchical scenario. The detail of this kind of model and the calculation of the luminosity function will be presented in the next chapter.

Chapter 3

Luminosity Function of High-z AGN

In this chapter, AGN phase as one of significant stages for galactic formation and evolution is stressed. Dark matter halos form at the rate predicted by the canonical hierarchical clustering scenario. However, it is not guaranteed that baryons have to follow the same track. AGN luminosity function has been theoretically derived using the anti-hierarchical baryon collapse model by Granato et al. (2004) in which more complex situations of baryons are concerned.

All the physical ingredients for preparation are presented in the section 3.1. In the section 3.1.1, both Press-Schechter and Sheth-Tormen mass function and their derivative form are reviewed. The density profile and circular velocity of dark halo are presented in the section 3.1.2. The relationship between black hole mass in the center of host galaxy and the velocity dispersion of the bulge are described in the section 3.1.3. The procedures of black hole growth are given in the section 3.1.4. In the section 3.1.5, feedback processes of supernova and AGN are mentioned. AGN lifetime is discussed in the section 3.1.6. Bolometric correction is placed in the section 3.1.7.

The section 3.2 includes the models of galactic formation and evolution. The monolithic model and hierarchical model are introduced in section 3.2.1 and 3.2.2 respectively. Coevolution of galaxies and AGNs is demonstrated in the section 3.2.3. The regime of anti-hierarchical baryon collapse model is drawn in the section 3.2.4., in which the concept of time delay from the beginning of black hole growth to the unobscured AGN shining phase is particularly put forward.

Predicted by the anti-hierarchical baryon collapse model, AGN luminosity function as a part of the whole strategy is investigated in detail in the section 3.3. The analytic formula and the output of the code are shown in the section 3.3.1 and 3.3.2; The AGN luminosity functions of optical and hard X-ray band are performed in the section 3.3.3. The properties of the host galaxies are shown in the section 3.3.4. A short conclusion for the model of AGN-galaxy coevolution is drawn in the section 3.3.5.

In the section 3.4, other issues associated for high redshift AGN are added. The Spitzer observation of AGNs is described in the section 3.4.1; In the section 3.4.2, the multi-band observations are discussed to reveal the intrinsic properties of AGN; the NLSy1 with super-Eddington accretion, as the initial stage of AGN activity is also mentioned. These interesting topics could be treated as the future work.

3.1 Physical Ingredients

The physical processes of galactic formation and evolution are presented below:

(1) Formation and merging of dark matter halo;
(2) Shock-heating and radiative cooling of gas in the dark matter halo;
(3) Collapse of cold gas and star formation;
(4) Feedback due to supernova explore and stellar wind;
(5) Chemical enrichment of gas and stars ;
(6) Galaxy mergers;
(7) Luminosity evolution of stellar populations;
(8) Absorption of starlight by dust and re-emission in IR and sub-mm;
(9) Formation of supermassive black hole-AGN and feedback to IGM;

These processes are divided into two parts. The point (1) is about pure dark matter condition which provides the halo mass function and the density profile of the dark halo, while point (2) to (9) are including all kinds of physics of baryons. Most of them are taken into account for research of AGN luminosity function within the whole scenario of coevolution between AGNs and spheroid galaxies. In this section, some ingredients involved tightly with the thesis are discussed in detail.

3.1.1 Dark Halo Mass Function and Derivative Formula

The non-linear evolution of dark matter has been studied extensively with the halo models on large scale structure(Cooray & Sheth 2002). The Press-Schechter mass function(Press & Schechter 1974, Sasaki 1994) for spherical collapse presented in the Section 1.2 is given by:

$$N_{ps}(M,z) = \sqrt{\frac{2}{\pi}}\frac{\rho_0}{M}\frac{\delta_c}{D(z)}\left|\frac{1}{\sigma^2}\frac{d\sigma}{dM}\right|\exp\left(\frac{-\delta_c^2}{2\sigma^2 D(z)^2}\right) \tag{3.1}$$

where $\delta_c = 1.68$, ρ_0 is the mean comoving density and $D(z) = 1/(1+z)$ is the Peebles function for the growth of the perturbations. The primordial perturbation can be expressed by:

$$\sigma^2(M) = \int_0^{k_s} P(k) 4\pi k^2 dk \tag{3.2}$$

where $P(k) \propto k^{-2}$ is the power spectrum of the density fluctuation and k_s is linked by $M = 6\pi^2\rho_0 k_s^{-3}$(Mahmood, Devriendt & Silk 2005).

There is the general treatment of derivative dark halo mass function in which the merger rate is taken into account to link the black hole mass thus obtain the AGN luminosity function(Wyithe & Loeb 2002). However, in this context, another method shown below is valid to avoid the merging effect.

The total change of halo number density of a given mass in a certain time is(Sasaki 1994):

$$\dot{N}_{ps}(M,z) = \dot{N}_{form}(M,z) - \dot{N}_{dest}(M,z) \tag{3.3}$$

The first term $\dot{N}_{form}(M,z)$ means the pure formation rate and the second term $\dot{N}_{dest}(M,z)$ means a destruction rate due to mergers. In the following calculation, the destruction term is ignored thus only formation rate is taken into account. Therefore the formation rate is:

$$\dot{N}_{form}(M,z) = \sqrt{\frac{2}{\pi}}\frac{\rho_0}{M}\delta_c\left|\frac{1}{\sigma^2}\frac{d\sigma}{dM}\right|\exp\left(\frac{-\delta_c^2}{2\sigma^2 D(z)^2}\right) \tag{3.4}$$

which is also called derivative Press-Schechter formula.

The halo mass function has another form produced by Sheth & Tormen(1999, 2002) for ellipsoidal collapse approach:

$$N_{st}(M,z) = \frac{\rho_0}{M^2}|\frac{dln\nu}{dlnM}|\nu f(\nu) \tag{3.5}$$

where

$$\nu f(\nu) = A[1+(a\nu)^{-p}](\frac{a\nu}{2})^{1/2}\frac{e^{-a\nu/2}}{\sqrt{\pi}} \tag{3.6}$$

$\nu = (\delta_c/D(z)\sigma(M))^2$, $\sigma(M)$ has the form of equation 3.2, $A = 0.322$, $p = 0.3$ and $a = 0.707$. Similar of equation 3.3 and 3.4, the derivative Sheth-Tormen formula can be obtained as:

$$\dot{N}_{form}(M,z) = \dot{N}1_{form}(M,z) + \dot{N}2_{form}(M,z) \tag{3.7}$$

in which

$$\dot{N}1_{form}(M,z) = 0.2\frac{\rho_0}{M}\frac{\delta_c}{\sigma^2}e^{\frac{-0.35\delta_c^2(1+z)^2}{\sigma^2}}\frac{d\sigma}{dM} \tag{3.8}$$

and

$$\dot{N}2_{form}(M,z) = 0.88\frac{\rho_0}{M}\frac{\delta_c^{0.4}(1+z)^{-0.6}}{\sigma^{1.4}}e^{\frac{-0.35\delta_c^2(1+z)^2}{\sigma^2}}\frac{d\sigma}{dM} \tag{3.9}$$

The different profiles of Press-Schechter and Sheth-Tormen have been investigated by Springel et al. (2005) and Mahmood & Rajesh (2005). The direct comparison of two kinds of formation rates at different redshifts are shown in the Fig. 3.1 and 3.2. At low redshift, the two functions have no prominent difference. However, at high redshift, the strong divergence appears in the massive-halo part. Since the results of Sheth & Tormen are suitable for high redshift universe(Springel et al. 2005), during this context, the derivative Sheth-Tormen formula are selected for the calculation of AGN luminosity function.

3.1.2 Dark Halo Density Profile and Circular Velocity

Most scientists believe that the dark matter halo plays an important role on galactic formation and evolution although the existence of halos is still debated(Romanosky 2003). The virialized halo exhibits the density profile as(Navarro, Frenk & White 1997; Jing & Suto 2000):

$$\rho(r) = \frac{\rho_s}{cx(1+cx)^2} \tag{3.10}$$

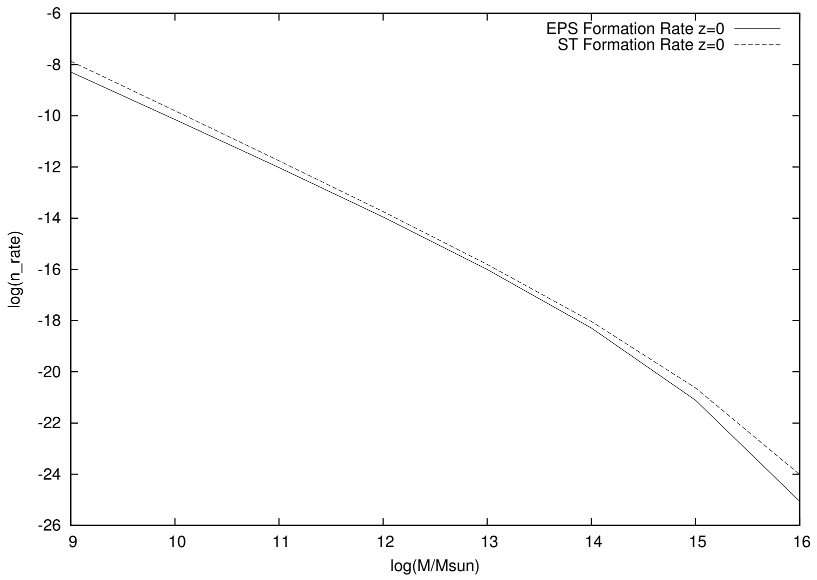

Figure 3.1: The formation rates of Sheth-Tormen and Press-Schechter at z=0

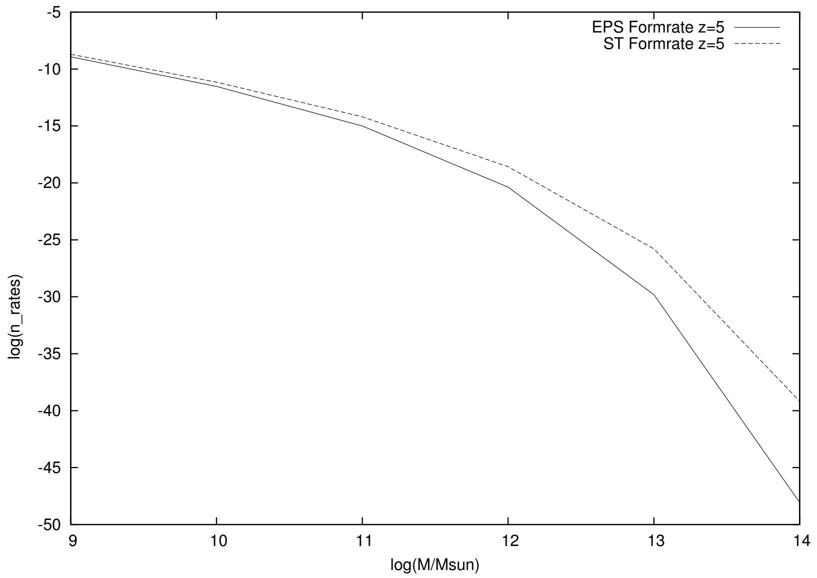

Figure 3.2: The formation rates of Sheth-Tormen and Press-Schechter at z=5

where $x = r/r_{vir}$, r_{vir} is the virialized radius and c is the concentration parameter. Bullock et al. (2001) found that c is the weak function of the mass as $c \propto M^{-0.13}$ while at fixed mass $c \propto (1+z)^{-1}$.

Numerical simulations have shown that the dark halos proceed one fast accretion via collapse or major mergers and one slow phase with minor change to the center, moreover, the potential well of the halo is built up during the fast accretion(Zhao et al. 2003; Romano-Diaz et al. 2005; Li et al. 2005). In the fast accretion phase the inner density profile of dark halo is $\rho(r) \propto r^{-1}$ while slow accretion leads to an outer profile as $\rho(r) \propto r^{-3}$(Lu et al. 2005).

This density profile of dark matter halo can be examined by observation. For instance, based on the virial theorem, the gas at the edge of this deep potential well is hot, thus the hot gas is ionized and emits X-ray due to bremsstrahlung(Makino, Sasaki & Suto 1998).

For a pure CDM model, a halo of mass M_{halo} at redshift z has the collapse viral radius(Barkana & Loeb 2001):

$$R = 31(\frac{M_{halo}}{10^{12}M_\odot})^{1/3}(\frac{\Omega_m}{\Omega_m^z}\frac{\Delta_c}{18\pi^2})^{-1/3}(\frac{1+z}{7})^{-1}kpc \tag{3.11}$$

and the circular velocity of the dark matter halo is described as(Loeb & Peebles 2003):

$$V_c = (\frac{GM_{halo}}{R})^{1/2} = 375(\frac{M_{halo}}{10^{12}M_\odot})^{1/3}(\frac{\Omega_m}{\Omega_m^z}\frac{\Delta_c}{18\pi^2})^{1/6}(\frac{1+z}{7})^{1/2}kms^{-1} \tag{3.12}$$

where $\Delta_c = 18\pi^2 + 82d - 39d^2$ with $d \equiv \Omega_m^z - 1$ and $\Omega_m^z - 1 = \Omega_m(1+z)^3/[\Omega_m(1+z)^3 + \Omega_\Lambda]$.

For simplicity, other dark matter profiles such as Moore et al. (1999a, 1999b) and Stoehr et al. (2002, 2003, 2005) are not discussed here.

3.1.3 $M_{BH} - \sigma$ Relation

Supermassive black holes are considered to be a common feature of not only elliptical galaxies but also AGNs. The strong correlation between black hole mass M_{BH} and the velocity dispersion σ within the galactic bulge has been found(Ferrarese & Merritt 2000; Gebhardt et al. 2000):

$$logM_{BH} = \alpha log\sigma + \beta \tag{3.13}$$

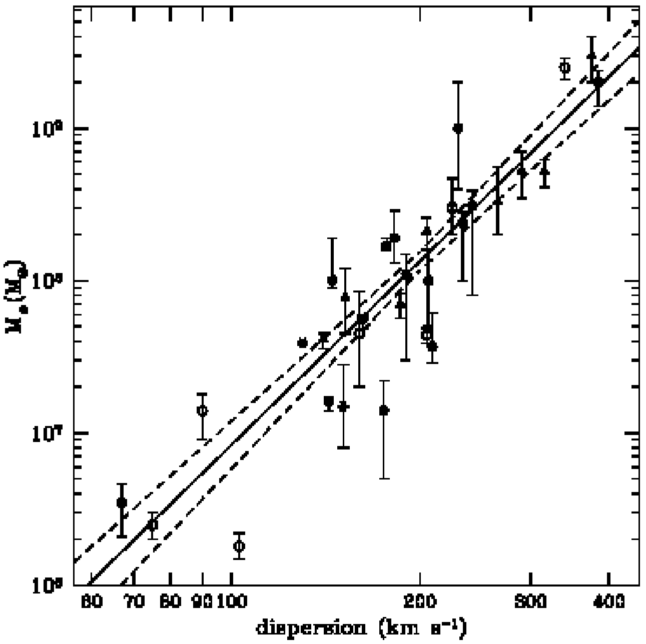

Figure 3.3: M_{BH}-σ relation. The solid line is the best fitting

where $\alpha = 4.02 \pm 0.32$(Tremaine et al. 2002). The relationship between M_{BH} and σ is shown as an example in the Fig 3.3 (Tremaine et al. 2002). This $M_{BH} - \sigma$ relation has also been examined for AGNs(Shields et al. 2003; Grupe & Mathur 2004; Onken et al. 2004; Nelson et al. 2004; Treu et al. 2004). It has been found that $M_{BH} - \sigma$ relation of local AGNs has a lower zeropoint, shallower slope and probably larger scatter than those of inactive galaxies(Greene & Ho 2006).

For measuring the black hole masses in normal galaxies, the methods are gas dynamics or stellar dynamics(Osmer 2003). As AGNs, the response of emission lines to a continuum change is delayed and spread out by light travel time, thus the size and structure of broad-line region can be obtained by observing the response variations. This is so-called reverberation mapping(Perterson 1993). Kaspi et al. (2000, 2005) found that the size of broad-line region is correlated strongly with the AGN continuum luminosity. Therefore, the measurement of optical(5100$\mathring{A}$) continuum luminosity and width of $H\beta$ emission line is widely used for estimation of black hole masses at low redshift($z < 0.75$). An improvement is to measure the strength and the width of $H\alpha$ instead of $H\beta$ emission line (Greene & Ho 2005). For intermediate redshifts($0.4 < z < 2$) the width of MgII($\lambda 2798\mathring{A}$) emission line and the continuum luminosity are given to estimate the black hole mass while the observation for the width of CVI($\lambda 1549\mathring{A}$) emission line and UV continuum luminosity is the powerful tool for those black holes at high redshifts($1.6 < z < 5$)(Vestergaard 2004; Kollmeier et al. 2005). The estimation formulas of black hole mass are listed below(Vestergaard 2004):

$$logM_{BH}/M_{sun} = log\Big\{\Big[\frac{FWHM(H\beta)}{1000kms^{-1}}\Big]^2\Big[\frac{\lambda L_\lambda(5100\mathring{A})}{10^{44}ergss^{-1}}\Big]^{0.7}\Big\} + 6.7 \tag{3.14}$$

and

$$logM_{BH}/M_{sun} = log\Big\{\Big[\frac{FWHM(CIV)}{1000kms^{-1}}\Big]^2\Big[\frac{\lambda L_\lambda(1350\mathring{A})}{10^{44}ergss^{-1}}\Big]^{0.7}\Big\} + 6.2 \tag{3.15}$$

To determine the velocity dispersion σ, in general, the spectral template of stars(G-K giants) is needed and it is compared with the target spectrum(Treu et al. 2004; Onken et al. 2004). For simplicity, the narrow emission line [OIII] and the CaII triplet absorption line are often selected(Nelson & Whittle 1996; Shields et al. 2003). At high redshift, the velocity dispersion σ is estimated from the CO emission line(Shields et al. 2006). It is noticed that determination of velocity dispersion is dependent on the size of the aperture used and the location of the aperture with respect to the galaxy/AGN core.

$M_{BH} - \sigma$ relation is consistent with the point of view that the growth of supermassive black holes and galactic bulges occurred simultaneously. Shields et al. (2003) found that $M_{BH} - \sigma$ relation does not evolve strongly with time below redshift 3. The simulation which includes feedback of supermassive black hole suggests that the normalization of the $M_{BH} - \sigma$ relation may experience a weak evolution with redshift but the slope is the same at all redshifts(Robertson et al. 2005). However, by a sample of soft X-ray selected Seyfert galaxies, Grupe & Mathur (2004) found that the black holes may grow by accretion in well formed bulges. Treu et al. (2004) had the AGN sample reaching at redshift 0.37 and drew the result that spheroids evolve faster than black holes in the past 4 Gyrs. The observation of $M_{bh} - \sigma$ relation for QSOs at redshift $z > 3$ has shown that giant black holes reside in undersized bulgers by an order of magnitude or more, indicating that the largest black holes evidently grow rapidly in the early universe without commensurate growth of their host galaxies(Shields et al. 2006). Furthermore, narrow line Seyfert 1 galaxies as a high accretion AGN subclass are particularly concerned on the $M_{BH} - \sigma$ plane(Mathur & Grupe 2005) and the authors argued that there is no single explanation for the origin of $M_{BH} - \sigma$ relation.

3.1.4 BH Growth

The supermassive black hole growth is the vital stage in AGN evolution. In general, the models which have been proposed include: gas accretion from the seed black holes(Small & Blandford 1992; Kawakatu, Umemura & Mori 2003; Granato et al. 2004; Springel, Di Matteo & Hernquist 2005a; Volonteri & Rees 2005; Vittorini, Shankar & Cavaliere 2005), accretion both dark matter and gas(Hu et al. 2005), black hole binary merging(Milosavljevic et al. 2002; Jaffe & Backer 2003), collapse from the dense gas in the first galaxies(Bromm & Loeb 2003) and star clusters collapse(Gurkan, Freitag & Rasio 2004).

During this thesis, the case of gas accretion has been considered as the way of black hole growth. Due to gas accretion, black hole growth will spend a period of time which is from the certain virial epoch of dark halo to the observed AGN shining phase. Therefore, this time delay plays a vital effect on the luminosity functions of AGN and this concept is the prominent difference with other AGN evolution models.

From the formula $L = \eta \dot{M} c^2$, it is worth knowing that cumulative black hole mass can be related to the luminosity which signals current source activity(Vittorini, Shankar & Cavaliere 2005):

$$M_{BH}(t) = \frac{1}{\eta c^2} \int^{t} L(t^{'}) dt^{'} \tag{3.16}$$

Therefore, although AGN lifetime is short compared with the cosmic timescale, the black hole mass can reach a large value of 10^{10} solar mass through accumulation of multiple accretion facts during several Gyrs.

For a single accretion event, Small & Blandford (1992) related the observed evolution of AGNs to the black hole growth with the accretion rate as a function of black hole mass and cosmic time. Black hole growth is viewed as a exponential form with the seed mass of 100 to 1000 solar mass(Kawakatu, Umemura & Mori 2003; Springel, Di Matteo & Hernquist 2005a; Vittorini, Shankar & Cavaliere 2005):

$$M_{BH} = M_0 exp(\lambda t/t_s) \tag{3.17}$$

where M_0 is the mass of the seed black hole. Salpeter timescale is defined as:

$$t_s \equiv \frac{\varepsilon M_{BH} c^2}{(1-\varepsilon)L} \tag{3.18}$$

where $t_s = \eta t_{edd} = 4.6 \times 10^7 yr$ for $\varepsilon = 0.1$ and $\lambda = \dot{m}/\dot{m_{edd}}$ is the accretion ratio.

As mentioned in the section 1.4.2, super-Eddington accretion could be a possible process at high redshift. In the model of Granato et al. (2004), the maximum value of accretion ratio is about 3 but the detail of accretion is unknown. If the Bondi-Hoyle formula of quasi-spherical accretion is selected, the accretion rate is about 40 times of Eddington rate(Volonteri & Rees 2005). Recently, it has been found that supermassive black holes spend most time in low efficiency, low accretion rate states while the growth of the mass is dominated by the short high accretion rate phases(Hopkins, Narayan & Hernquist 2005).

It is also noticed that the black mass will evolve as below if the accretion rate is lower than Eddington ratio(Springel, Di Matteo & Hernquist 2005a):

$$M_{BH} = \frac{M_0}{1 - \chi M_0 t} \tag{3.19}$$

where $\chi = 4\pi\alpha G^2 \rho/(c_s^2 + v^2)^{3/2}$, ρ and c_s are the density and sound speed of the gas, v is the velocity of the gas relative to the black hole, α is a dimensionless parameter. This set of parameters is also original from the Bondi-Hoyle formula.

In this thesis, it is always assumed that black holes grow as the exponential form of equation 3.17 due to super-Eddington accretion until it is quenched by the feedback of supernova and AGN. The time delay due to black hole growth as a single accretion event has been stressed.

3.1.5 Feedback from Supernova and AGN

Feedback from supernova and AGN are beginning to gain attention as important processes during the galaxy formation and evolution. Two opposite affects of the feedback have been investigated. The certain observation(Rejkuba 2002) and simulation(Fragile, Murray & Lin 2004; Fragile et al. 2004) suggest that shocks generated by the supernova or AGN jet propagate through an inhomogeneous medium and trigger the collapse of overdense clouds, which then become active star-forming regions. Alternatively, for example, the AGN has been calculated as the heating source of intracluster medium(Roychowdhury et al. 2004) and it can quench star formation and accretion on a short timescale (Springel, Di Matteo & Hernquist 2005a; Di Matteo, Springel & Hernquist 2005). In this thesis, the second opinion of feedback which gives the negative affect to the galactic formation and evolution is taken into account.

The kinetic energy released by supernova is one powerful feedback of the galaxy formation and evolution(e.g., Maclow & Ferrara 1999; Wada & Venkatesan 2003). The supernova feedback moves the gas from the cold to the hot phase at a rate(Granato et al 2004):

$$\dot{m}_{SN} = \frac{2}{3}\psi(t)\epsilon_{SN}\frac{\eta_{SN}E_{SN}}{\sigma^2} \tag{3.20}$$

where $E_{SN} = 10^{51} ergs$ is the kinetic energy released by one supernova explosion; η_{SN} is the number of supernova per solar mass of formed stars which is determined by the Initial Mass Function(IMF), for the IMF of Salpeter(1955), $\eta_{SN} = 6.3 \times 10^{-3}$ (Kang et al. 2004); $\psi(t)$ is the star formation rate and ϵ_{SN} is the fraction of the energy that is used to reheat the cold gas.

AGNs release the energy and preheat the surrounding environment. This feedback process should be also put inside the whole physics of galactic formation and evolution. Generally, the forms of AGN feedback(Begelman 2003) are kinetic energy, radiative heating, radiation pressure and energetic particles. The popular discussed features are kinetic energy(e.g., Bower et al. 2001) and radiative heating(Ostriker & Ciotti 2005). Of the kinetic energy, the feedback injected by the AGN outflow or jet tends to be trapped by the ambient medium, leading to a high feedback efficiency(Granato et al. 2004;

Levine & Gnedin 2005). For the radiative heating, the feedback via photoionization and Compton heating on the massive black holes at the center of spheroidal galaxies has been taken into account(Ciotti & Ostriker 1997, 2001; Sazonov et al. 2005). Compared with supernova, the AGNs potentially provide a larger energy output in shorter times (Cavaliere, Lapi & Menci 2002). In this thesis, the kinetic energy released by the AGN is considered as(Granato et al. 2004):

$$\dot{m}_{AGN} = 2.0 \times 10^3 \frac{\epsilon_{AGN} L_{edd,46}^{2/3}}{(\sigma/300kms^{-1})^2} \frac{M_{cold}}{M_{gas}} M_{\odot} yr^{-1} \tag{3.21}$$

where $M_{gas} = M_{cold} + M_{inf}$ is the mass of the gas in the cold phase plus that of the gas which has not yet fallen in the star-forming region, $L_{edd,46}$ is the Eddington luminosity in units of $10^{46} ergs\ s^{-1}$, ϵ_{AGN} is the adjustable value from 1 to 10.

3.1.6 AGN Lifetime

AGN lifetime is another fundamental element for understanding black hole and AGN evolution(Martini 2004) and it is determined by several methods as shown below.

(1) A minimum number of 10^5yr is needed to explain the proximity effect in the Lyman alpha forest(Bajtlik, Duncan & Ostrike 1988) while this effect in high redshift QSOs implies a lifetime of 10^7yr(Haiman & Cen 2002);

(2) The e-folding time given by Salpeter timescale(Salpeter 1964; Marconi et al. 2004) is about:

$$t_{salpeter} = \frac{\varepsilon t_{edd}}{(1-\varepsilon)\lambda} = 4.2 \times 10^7 yr (\frac{1-\varepsilon}{9\varepsilon})^{-1} \lambda^{-1} \tag{3.22}$$

where ε is the accretion efficiency and t_{edd} is the Eddington timescale shown in the section 1.4.2.;

(3) Wyithe & Loeb(2003a) studied the dynamic timescale of the galactic disk as:

$$t_{dyn} = 0.035 \frac{r_{vir}}{v_c} = 10^7 [\xi(z)]^{-1/2} \Big(\frac{1+z}{3}\Big)^{-2/3} yr \tag{3.23}$$

where $\xi(z)$ is nearly unity. AGN lifetime in this literature is identified using t_{dyn};

(4) The values above are consistent in the range of 10^6 to 10^8yr from the estimation of clustering(Martini & Weinberg 2001; Haiman & Hui 2001). Under the merging prediction of Lacey & Cole(1993), Croom et al. (2005) have shown that upper limits of QSO lifetime are smaller with increasing redshift: 6×10^8yr at $z = 2.48$; 1.0×10^9yr at $z = 1.7$ and 3×10^9yr at $z = 0.53$.

(5) Furthermore, since AGNs are powered by accretion from the surrounding gas and dust, recently, it is noticed that AGN lifetime has a possible correlation with luminosity(Adelberger & Steidel 2005). From the simulation(Hopkins et al. 2005a), the luminosity-dependent AGN lifetime for fitting AGN luminosity function is presented as(Hopkins et al. 2005b,c):

$$t_Q = 10^9 (L/10^9 L_\odot)^\alpha yr \tag{3.24}$$

where α is a function of the peak of luminosity.

However, in this thesis, the AGN lifetime used here has been simplified as a certain value of about 10^7 years for optical band and of about 10^8 years for X-ray band to fit the observational data.

3.1.7 Bolometric Correction to Optical and Hard X-ray Band

The bolometric luminosity function derived through the theoretical models should be transfered into X-ray and optical band luminosity functions with the bolometric correction thus one can compare them to the observational data. In general, the proper bolometric correction can be obtained from the multiband composite spectrum. The relations from bolometric luminosity L_{bol} to B band luminosity l_B and hard X-ray luminosity L_X are $L_{bol} = k_B \nu_B l_B$ and $L_{bol} = k_X L_X$.

The widely used values are given as $k_B = 11.8$ and $k_X = 35$ for broad-line AGN(Elvis et al. 1994). More deliberative values are proposed for optical AGNs as $L_{bol} = 9.74\lambda L_\lambda(4400\mathring{A})$ at $z < 0.5$, $L_{bol} = 4.62\lambda L_\lambda(1350\mathring{A})$ at $1.5 < z < 3.5$ and $L_{bol} = 4.65\lambda L_\lambda(1450\mathring{A})$ at $z > 3.5$(Vestergaard 2004). For those non-broad-line AGNs, the proper value of bolometric correction in hard X-ray band is about 85(Barger et al. 2005). Shankar et al. (2004) proposed the bolometric correction of hard X-ray which is the function of hard X-ray luminosity:

$$k_X = 17(\frac{L_X}{10^{43} ergs\ s^{-1}})^{0.43} \tag{3.25}$$

In the calculation of section 3.3, the parameter $k_B = 11.8$ and the equation 3.25 are used to derive optical and X-ray luminosity function respectively.

3.2 Galaxy Formation and Evolution

3.2.1 Monolithic Evolution

The evidence from the orbits of dwarf stars which proposes the motivation of collapsed galaxy was shown initially by Eggen, Lynden-bell & Sandage(1962). It means that in a deep potential well a galaxy may form from the cloud of primordial gas by rapid gravitational collapse. The scenario that single intense starburst at high redshift followed by passive evolution(Partridge & Peebles 1967a,b) is called monolithic formation. The dynamical model including energy loss, star formation, stellar mass loss and heavy element production was built for the spherical protogalaxy(Larson 1969; Larson 1974; Larson 1975). In these papers, fluid hydrodynamical approach was used to treat both gas and stars. The star formation occurs at early cosmic time and continues in the nucleus of the galaxy for a long period time. Quasar phenomenon as a stage in the formation of giant elliptical galaxy was also proposed. The N-body simulation in corporating the cooling, star formation, SN feedback and chemical evolution reproduced basic properties of elliptical galaxies well(Chiosi & Carraro 2002). Thus, the general picture of monolithic formation successfully interprets the fundamental plane(Djorgovski & Davis 1987; van Dokkum & Stanford 2003), the mass-to-light ratio versus central velocity dispersion(Burstein et al. 1997), color-magnitude relation(Bower, Lucey & Ellis 1992; Kodama et al. 1998) and gross chemical evolution properties(Gibson & Matteucci 1997) of both dwarf and giant ellipticals. Recent analysis from a Sloan Digital Sky Survey(SDSS) sample of over 2000 galaxies has reconstructed the concentration halo parameter c and derived scaling relations between stellar mass and the velocity dispersion, which are consistent with the numerical simulation and sufficient to recover the tilt of the fundamental plane(Lintott, Ferreras & Lahav 2006).

3.2.2 Hierarchical Collapse

Nowadays the hierarchical models of galactic formation and evolution are popularly accepted and achieve great success. It is therefore valuable to present a short review of this scenario in general and in the mean time pay attention to those problems which are the challenges to this canonical framework.

The pioneer computational work of galactic interaction was first concerned by Toomre & Toomre (1972). This article suggested the possibility of close encounters. Actually, as first step, the hierarchical galactic formation begins with the dynamics and distribution of pure dark matter halos. Small dark halos which are perturbed by initial density fluctuations dominate the early universe, then these small pieces merge each other into the big one. Second, the baryons are involved to trace the formation of dark halos. Through baryon physics such as cooling, star formation, stellar evolution, chemical evolution and so on, finally, the luminous galaxies are thought to occur in the center of virialized dark halos. Thus, under this picture, the small gas-rich spirals form primely at high redshift, then, these small spirals turn into the massive ellipticals by merging at low redshift(White & Rees 1978; White & Frenk 1991).

During this process, the dark halo distribution can be described by Press-Schechter mass function(Press & Schechter 1974) mentioned in the section 3.1.1. Subsequently, the merger rates in the hierarchical model are calculated in detail by Lacey & Cole (1993). The cartoon of merging tree is shown in Fig. 3.4(Haehnelt 2003). These kind of analytical or semi-analytical models(Mo & White 1996; Somerville & Primack 1999; Cole et al. 2000; Kang et al. 2004) have been built and their results fit well with the numerical simulations and observations(e.g. Kauffmann et al. 1999a, b; Diaferio et al. 1999).

Since merging is the key point of this scenario, from the measurement of close galactic pair(Zepf & Koo 1989; Patton et al. 1997; Carlberg et al.

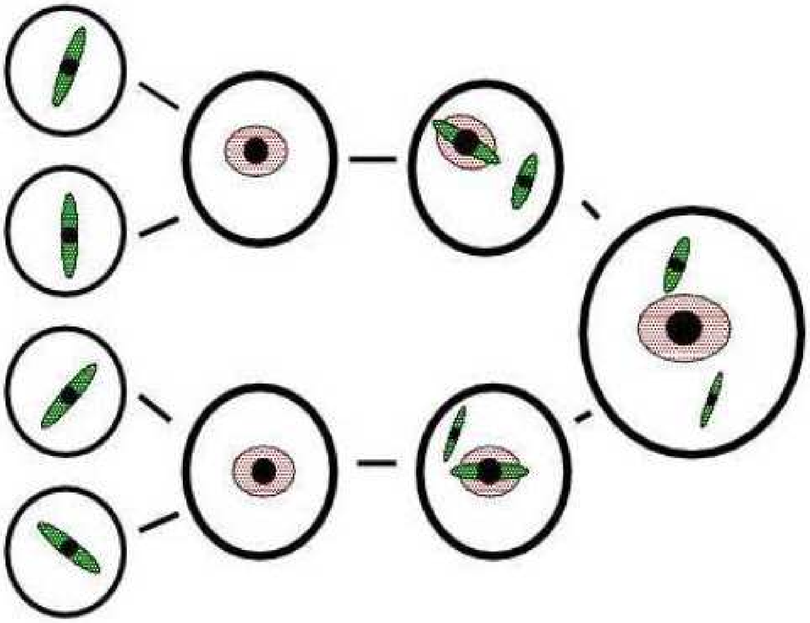

Figure 3.4: The "merger tree" model of galaxies within the dark matter halos

2000; De Propris et al. 2005), the merger rates has been found to change with redshift as $(1+z)^{2.8\pm0.9}$. On the other hand, the survey of merger remnants has been carried out(Rothberg & Joseph 2004). The photometric and kinematic data are used to demonstrate that the central phase-space density of mergers are equivalent to elliptical galaxies (Rothberg & Joseph 2005). These explorations give the merger hypothesis a further support.

However, it is well known that the stellar populations in the elliptical galaxies are generally old and have a passive evolution after a single starburst(Bernardi et al. 2003a,b, Bernardi et al. 2005). Particularly, more and more observational evidences show that elliptical galaxies with old stellar population are already assembled at early universe of redshift 2(Franx et al 2003; Fontana et al. 2004; Yamada et al. 2005). These evidences are consistent with the term of down-sizing which means more massive galaxies forming at higher redshift(Cowie et al.1996; Heavens et al. 2004; Kodama et al. 2004; Treu et al. 2005; Juneau et al. 2004; Caputi et al. 2005). It also indicates that at least the build-up of massive early-type galaxies was much faster at high redshift than has been expected from theoretical simulations of present hierarchical models(Cimatti et al. 2004). Another observation for a sample of near infrared selected galaxies in the GOODS suggests that at redshift $z \leq 1.5$ both hierarchical model and passive model are similar to the observation while at redshift $z \geq 1.5$ the hierarchical model shows a deficit of galaxies and passive model predicts an excess(Somerville et al. 2004). From the dynamics point of view, under the hierarchical model, disk end up with too small radii due to low angular momentum of baryons(Navarro & Steinmetz 2000).

There are two approaches to treat these problems under the hierarchical framework. The first one is to debate again the properties of dark halo. Here are two examples: The simulation preserves the inner density profile of dark halo during the merging history thus in the meantime also keeps the central concentration of stars, so that the central regions appears to be stable to avoid the merging effects(Gao et al. 2004); The merger timescale and merger fraction have been re-studied and the rapid and early merging can be also one of the formation mechanisms of the massive ellipticals(Conselice 2005).

The second approach to solve those difficulties is to consider the importance of AGN evolution phase, including AGN feedback and central black hole growth. For instance, AGN feedback argued as to quench star formation has been put in gas-rich mergers for creating red ellipticals at high redshift(Springel, Di Matteo & Hernquist 2005b); The specially phenomenological model for radio-mode AGN feedback (Croton et al. 2005; De Lucia et al. 2005) has been proposed to suppress condensation in massive galaxies, reproduce the downsizing behaviour within the hierarchical frame and provide an energetically solution for the cooling flow problem(Cowie & Binney 1977; Peterson et al. 2001; Tamura et al. 2001). For the further research, AGN activity and galaxy evolution are taken into account as a whole physical union and this topic will be discussed in the following section.

3.2.3 Coevolution between Galaxies and AGNs

The galactic nuclei as collapsed old QSOs(Lynden-Bell 1969) were first proposed as the early work about the link between galaxies and AGNs. More and more observations of QSO host galaxies provide the possibility of studying the AGN environment. Except those naked QSOs(Magain et al. 2005), after the subtraction for Point Spread Function(PSF) of central QSO, the luminosity profile of host galaxy can be estimated(Disney et al. 1995; Bahcall et al. 1997; Boyce, Disney & Bleaken 1999). It is important to notice that local AGNs are reside almost exclusively in the massive early-type galaxies(Kauffmann et al. 2003). The study of galaxy/AGN connection in nearby early-type galaxies has also been carried out by multiwavelength observation(Capetti & Balmaverde 2005; Balmaverde & Capetti 2005) and simulations(e.g. Cattaneo et al. 2005).

Due to the $M_{BH} - \sigma$ relation in the section 3.1.3, a correlation has been found between the mass of black hole and spheroid as $M_{bh}/M_{sph} = 2 \times 10^{-3}$ at $z < 1$(Magorrian et al. 1998; Marconi & Hunt 2003; Haring & Rix 2004). However, over a wide redshift interval $0 < z < 2$, the ratio has the redshift evolution as $M_{bh}/M_{sph} \propto (1 + z)^{2.07 \pm 0.76}$(McLure et al. 2005). It is believed that the $M_{BH} - \sigma$ relation is more fundamental than $M_{BH} - M_{sph}$ relation(Wyithe & Loeb 2005). A comprehensive discussion of the observational data is presented by Novak, Faber & Dekel (2005).

Given $M_{halo} - V_c$ relation in the section 3.1.2 and $M_{BH} - \sigma$ relation in the section 3.1.3, the tight relation between the bulge velocity dispersion σ defined within an aperture of size less than 0.5kpc and the galactic circular velocity V_c measured at 20-80kpc in which the rotation curve is flat, is equivalent to the one between M_{BH} and M_{halo}(Ferrarese 2002). This relationship provides a possible way to transfer the dark halo mass function to black hole mass function(Wyithe & Loeb 2003a; Granato et al. 2004).

Moreover, from the observational view, the connection between star formation rate and black hole accretion rate has been explored both in the luminous QSOs(Heckman et al. 2004; Hao et al. 2005) and in the low luminosity AGNs(Satyapal et al. 2005; Dudik et al. 2005; Wu & Cao 2006). These evidences indicate that both AGN shining and star formation in the bulge could be fed by the cooling gas in the mean time.

Thus, the central black holes shining as AGNs and their host galaxies can be seen as a whole entity into the model of galactic formation and evolution. This opinion was already proposed by Silk & Rees (1998).

As the result of investigation, several coevolution models are listed below:

(1) Simple scaling models and simulation(e.g., Haehnelt & Rees 1993; Di Matteo et al. 2003) in which the black hole mass scaling law with properties of galaxies or dark halos is given;

(2) Merger or interaction supply(Kauffmann & Haehnelt 2000; Volonteri, Haardt & Madau 2002; Menci et al. 2003; Croton et al. 2005);

(3) self-regulating models(Haehnelt, Natarajan & Rees 1998; Wyithe & Loeb 2003a; Di Matteo, Springel & Hernquist 2005; Hopkins et al. 2005a-g);

(4)Galaxy-QSO reciprocal regulation(Granato et al. 2004; Sazonov et al. 2005).

Particularly, the growth of supermassive black holes and the coevolution between galaxies and AGNs can be explained in a consistent way using hierarchical scenario(Kauffmann & Haehnelt 2000; Haehnelt & Kauffmann 2000). This model reproduced the black hole growth through mergers, the strong decline in number density of AGNs from redshift 2 to 0 and the $M_{BH} - \sigma$ relation. Based on the hierarchical scenario, the merger leads to the strong inflows and feed gas to central black hole thus power the QSO shining. Oppositely, the feedback of the QSOs expels gas thus quench star formation and further black hole growth(Di Matteo, Springel & Hernquist 2005). The simulation of joint evolution of quasars, galaxies and their large-scale distribution has been carried out(Springel et al. 2005). The evolutionary model has been built for starbursts, quasars and spheroidal galaxies in which the growth of supermassive black holes and the AGN feedback play the dominant role(Hopkins et al. 2005d). After building the model of self-regulated black hole growth, it is concluded that the evolution of the faint end AGN luminosity function is associated with the black hole growth, but not decided by the black hole mass distribution even they grow as an anti-hierarchical behaviour(Lidz et al. 2005; Hopkins et al. 2005e,f). Furthermore, Hopkins et al (2005g) present the properties and evolution of red massive galaxies from QSO luminosity function.

3.2.4 Anti-Hierarchical Baryon Collapse Model: Global View

Alternatively, from the review for the growth of the supermassive black holes by Merloni (2004) and Shankar et al.(2004), it has been found that the majority of the most massive objects were already in place at $z \sim 3$ and lower mass ones mainly grew at lower redshift. This evolution of black hole mass function shows an inversion of hierarchical scenario. The central supermassive black hole may rapidly grow by accreting cooling gas at first, reaching a sufficiently large mass, then, its feedback is able to suppress gas cooling, the system switches to a stable state corresponding to passively evolving ellipticals and the jet/outflow keep the surrounding gas to be hot(e.g. Churazov et al. 2005, Scannapieco, Silk & Bouwens 2005).

Some simple models(Monaco, Salucci & Danese 2000; Granato et al. 2001; Cattaneo & Bernardi 2003) for the joint formation of QSOs and the stellar populations of elliptical galaxies have also shown the typical anti-hierarchical properties. Such results are consistent with the observations of black hole mass functions, submm counts of spheroidal galaxies and B-band/X-ray luminosity functions of QSOs.

Recently, Granato et al. (2004) put forward a whole scenario[1] of coevolution of massive spheroidal galaxies and active nuclei at their centers. The regime is shown in the Fig. 3.5. In this model, the virialized formation rates of dark halo is given by the positive term of derivative mass function produced by Sheth & Tormen(2002), and the negative term corresponding to their disappearance due to merging is negligible, as presented in the section 3.1. The diffuse gas within the dark halo potential well falls into the star formation region at a rate of cooling and dynamic timescales. The cooled gas feels the feedback from supernova and the central AGN which heat and possibly expel the gas from the potential well. Furthermore, the radiation drag damps down the angular momentum of cool gas, making inflow into a reservoir around the central black hole. Viscous drag then causes the gas to flow from the reservoir into the black hole, increasing its mass and powering the nuclear activity until its feedback is strong enough to stop the star

---

[1] It is called Anti-Hierarchical Baryon Collapse Model by Danese et al. (2004).

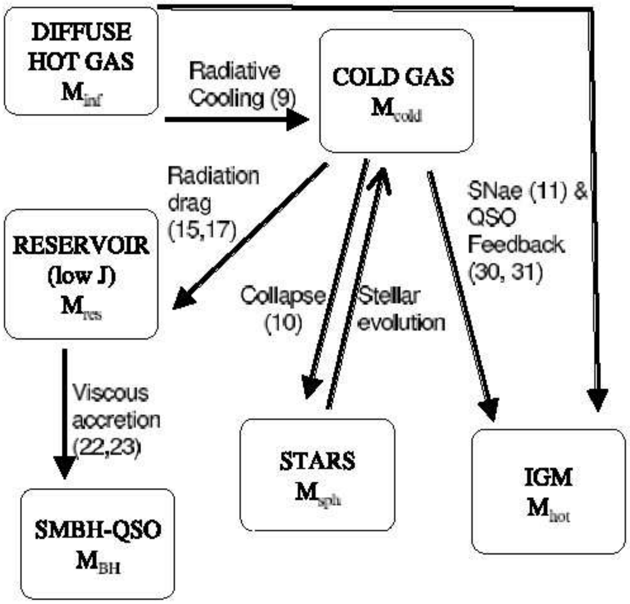

Figure 3.5: The model of coevolution between spheroidal galaxies and active nuclei produced by Granato et al.(2004).

formation and let the AGN shine unobscured.

Based on this scenario, the gas evolution is controlled by gravity, radiative cooling and the feedback of supernova and AGN. At high redshift, the mass of dark matter halo is small and the potential well is shallow so that the feedback of supernova and AGN is strong. The shallow potential well can not constrain the gas thus the massive protogalaxies form at earlier times with a faster star formation period, then evolve as passive way. Moreover, as mentioned in the section 3.1.4, due to strong feedback and the black hole growth, the central AGN shining will occur at later time after the dark halo virialized. In general, this time delay is a function of the halo mass and redshift. Hereafter, all of the calculations and results are under the framework of this model.

3.3 AGN Luminosity Function

X-ray and optical luminosity functions of AGN play a vital role on the tracing of black hole growth and AGN evolution. The general descriptions are described in the Appendix B. The recent observational results are presented in the Section 1.4.5. The GOODS observations push the results to the high redshift and low luminosity part as shown in the section 2.12. In this section, the theoretical luminosity function of AGN will be derived under the model of Granato et al. (2004).

Two important points should be mentioned as the vital differences to other coevolution models. First, as discussed in the section 3.1.5, the shallow potential wells are difficult to constrain the cold gas due to powerful feedback of AGNs and SNe; Second, as shown in the Fig. 3.6, at certain virialized time, the seed black hole begins to grow in the center of dark halo. From the moment of black hole being observed as AGN to the time of black hole growth reaching the peak of the mass, it is called the AGN lifetime or AGN visible time. From the time of halo virialization to the time of black hole growth reaching the peak, it is called the time delay. Therefore, AGN shining phase is not beginning at the epoch of halo virialization, but after the time delay of black hole growth.

3.3.1 Analytic Formula

In general, the AGN luminosity function can be derived as shown in the equation B.20 and B.21. However, if we assume that AGN lifetime is far smaller than the Hubble time as shown in section 3.1.6, we can rewrite the AGN luminosity function as(Mahmood, Devriendt & Silk 2005):

$$\phi_{AGN} = \frac{dn(z,L)}{dL} = \frac{d^2N_{st}}{dM_{halo}dz}\frac{dM_{halo}}{dM_{BH}}\frac{dM_{BH}}{dL}\frac{dz}{dt}\tau_{AGN} \tag{3.26}$$

The derivative formula of Sheth-Tormen has been defined by the equation 3.7, 3.8 and 3.9. If ΛCDM cosmology is selected, the dz/dt can be calculated as:

$$\frac{dz}{dt} = -H_0(1+z)\sqrt{\Omega_m(1+z)^3+\Omega_\Lambda} \tag{3.27}$$

where $H_0 = 72kms^{-1}Mpc^{-1}$ is the Hubble constant, $\Omega_\Lambda = 0.7$ and $\Omega_m = 0.3$.

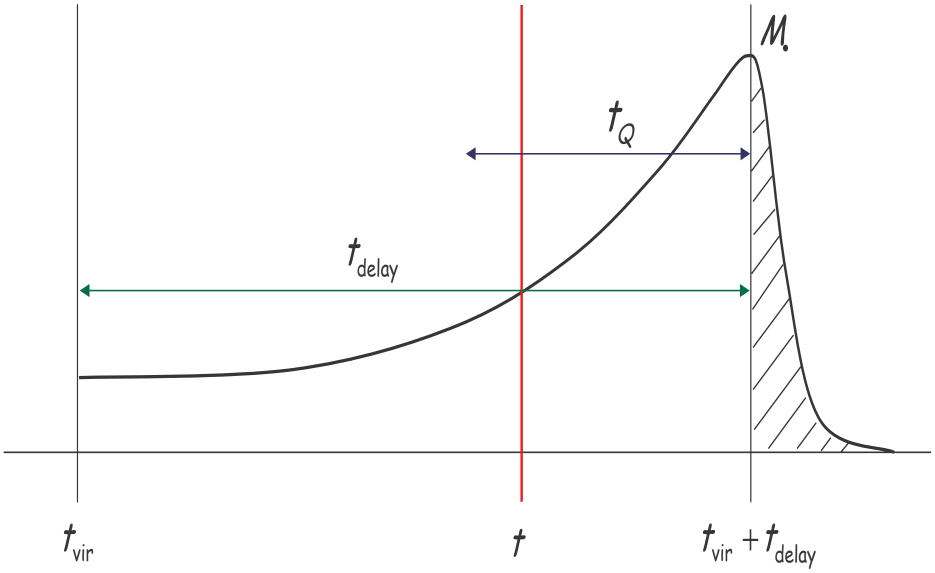

Figure 3.6: The cartoon of black hole growth. The BH seed of $10^2 M_\odot$ begins to grow at the virilized time, after a time delay, it reaches the peak of 10^6-$10^8 M_\odot$. T_Q is the lifetime in which BH shine as AGN.

The translation from dark halo rates to black hole formation rates can be approximated by the law which is derived from the result of Shankar et al. (2006):

$$M_{bh} = 8.0 \times 10^6 \frac{(M_{vir}/2.2 \times 10^{11} M_\odot)^{3.97}}{1 + (M_{vir}/2.2 \times 10^{11} M_\odot)^{2.7}} \frac{1 + z_{vir}}{7} M_\odot \tag{3.28}$$

Fig 3.7 shows the relation between black hole mass and dark halo mass. However, we find the scatter around this relationship and the value varies from halo to halo. Therefore, it is assumed that the $M_{vir} - M_{bh}$ relation holds on the average number with a Gaussian dispersion ΔM_{bh}. Then, the translation could be:

$$\frac{d^2 N_{bh}}{dt_{vir} dM_{bh}} = \int dM'_{bh} \left|\frac{dM_{vir}}{dM_{bh}}\right| \frac{d^2 N_{ST}}{dt_{vir} dM_{vir}} \frac{e^{-(M'_{bh} - M_{bh})^2/2(\Delta M_{bh})^2}}{(2\pi (\Delta M_{bh})^2)^{1/2}} \tag{3.29}$$

Due to accretion of the central black hole, up to the peak, the black hole light curve can be approximated by the simple exponential form:

$$L(t) = \frac{\lambda M_{bh} c^2}{t_{edd}} e^{(t - t_{vir} - \Delta t_{peak})/\tau_{ef}} \theta_H (t_{vir} + \Delta t_{peak} - \Delta t_{vis} \leq t \leq t_{vir} + \Delta t_{peak}) \tag{3.30}$$

where $t_{edd} = 4.6 \times 10^8 yr$ is the Eddington timescale, $\tau_{ef} = \eta t_{edd}/(1-\eta)\lambda$ is the e-folding time in terms of the black hole mass-energy conversion efficiency η and of the Eddington ratio λ. The function ($\theta_H(x) = 1$ if x is true; $\theta_H(x) = 0$ if other cases) specifies that the QSO shines unobscured only during the time interval Δt_{vis} before the peak of its light curve. It is noted that the Δt_{peak} is corresponding to the time delay t_{delay} as shown in the Fig. 3.6 and Δt_{vis} is the QSO lifetime.

The luminosity function is computed by summing up the contribution of all sources which virialize at epoch $t_{vir} \leq t$ and have the right delay to shine at the time t with luminosity L:

$$\Phi(L,t) = \int_{t_-\Delta t_{peak}}^{t-\Delta t_{peak}+\Delta t_{vis}} dt_{vir} \int dM_{bh} \frac{d^2 N_{bh}}{dt_{vir} dM_{bh}} \delta_D (L - \frac{\lambda M_{bh} c^2}{t_{edd}} e^{(t-t_{vir}-\Delta t_{peak})/\tau_{ef}}) \tag{3.31}$$

Compared with the Eqs. (3.26), this expression is including the concept of the time delay which as a function of halo mass is shown in the Fig 3.8 from the model. Using the bolometric correction described in the section 3.1.7, we can transfer the bolometric luminosity to the luminosity of X-ray and optical band.

In addition, from the black hole formation rates it is convenient to compute the black hole mass function as:

$$\Psi(log M_{bh}, t) = \int_0^t dt_{vir} \frac{d^2 N_{bh}}{dt_{vir} dlog M_{bh}} \tag{3.32}$$

3.3.2 Output of Coevolution Model: AGN properties

Based on the model of Granato et al. (2004), the baryonic content in a given halo is partitioned in three gaseous phases: a hot diffuse mass infalling or cooling to the center; cold gas condensing into stars; low angular momentum gas stored in a reservoir around black hole and providing accretion materials. The mass rate of the inflow gas toward the center is divided by two components: accretion rate of central black hole and the mass rate of reservoir. The accretion materials first accumulate in the reservoir and then flow into the black hole by viscosity. The accretion mechanism is followed by Burkert & Silk (2001). The timescale is dependent on the viscous drag under the onset of turbulence. The final accretion rate is the minimum value between viscous

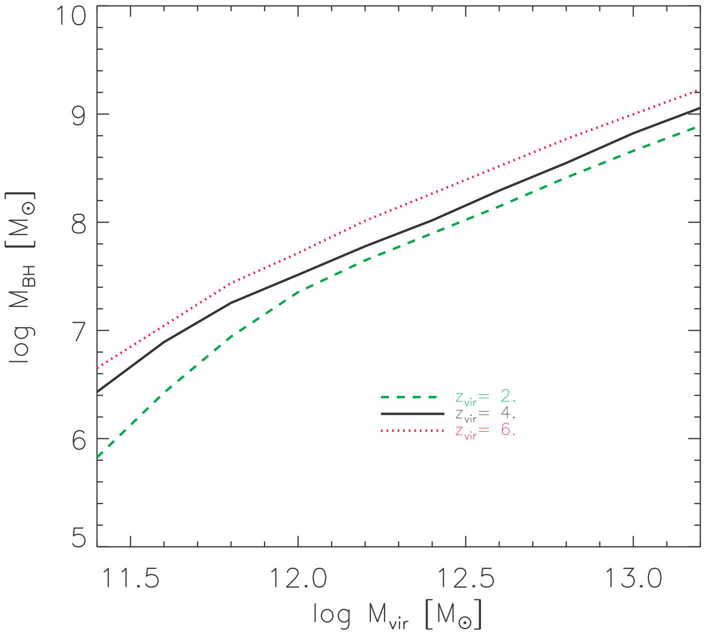

Figure 3.7: Relation between Dark Halo Mass and Black Hole Mass

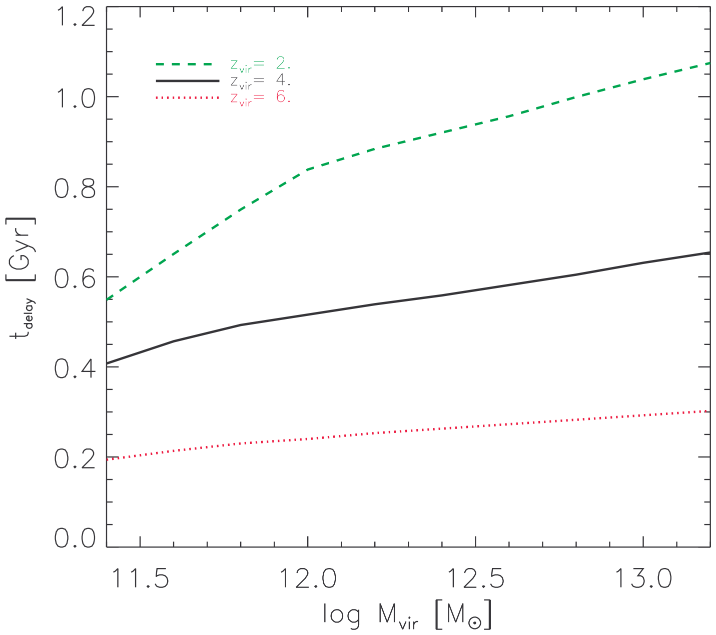

Figure 3.8: Time Delay as the function of dark halo mass

accretion and a few times of Eddington accretion. It is noted that this kind of accretion is also tightly associated with $M_{BH} - \sigma$ relation, therefore, the growth of black hole may be not limited by the Eddington limit, but decided by both accretion viscosity and galactic formation. The viscosity accretion rate is shown as:

$$\dot{M}_{bh}^{visc} = 5.0 \times 10^3 k_{accr} (\frac{V_{vir}}{500kms^{-1}})^3 \frac{M_{res}}{M_{bh}} (1 + \frac{M_{bh}}{M_{res}})^{1/2} \tag{3.33}$$

where $10^{-4} < k_{accr} < 10^{-2}$. The final accretion rate is decided by:

$$\dot{M}_{bh} = min(\dot{M}_{bh}^{visc}, \lambda \dot{M}_{bh}^{Edd}) \tag{3.34}$$

and $\dot{M}_{bh}^{Edd}$ is the Eddington rate.

The output of the model by Granato et al. (2004) provides the accretion rate, mass of reservoir and black hole mass growth in each dark halo mass from $10^{11.4} - 10^{13.4} M_\odot$ and each redshift bin from 1.5 to 11. The output example is shown in Fig 3.9, the black hole growth, the mass of reservoir and the accretion rate are evolved as the function of galactic time.

3.3.3 Results Presentation

After the prepared description, the AGN luminosity function of X-ray and optical band from redshift 1.5 to 6 are obtained(Lapi et al. 2006). Fig 3.10 is the optical luminosity function at $z = 6$. At redshift above 6, the luminosity function dramatically drop off due to much lower abundances of massive halos.

The particular data taken from the GOODS observation described in the Chapter 2 is shown in the Fig 3.11. The flattening of the luminosity function at the low end is due to both the flatter slope of dark halo formation rate and the time delay.

Different values of AGN lifetime(visibility timescale) give the different results. Fig 3.12 shows the difference as an example of optical band at $z = 3$. The visibility time turns out to be a factor of 5-10 shorter than the time delay, indicating a dust dominated phase as witnessed by submm observations before the QSO shine.

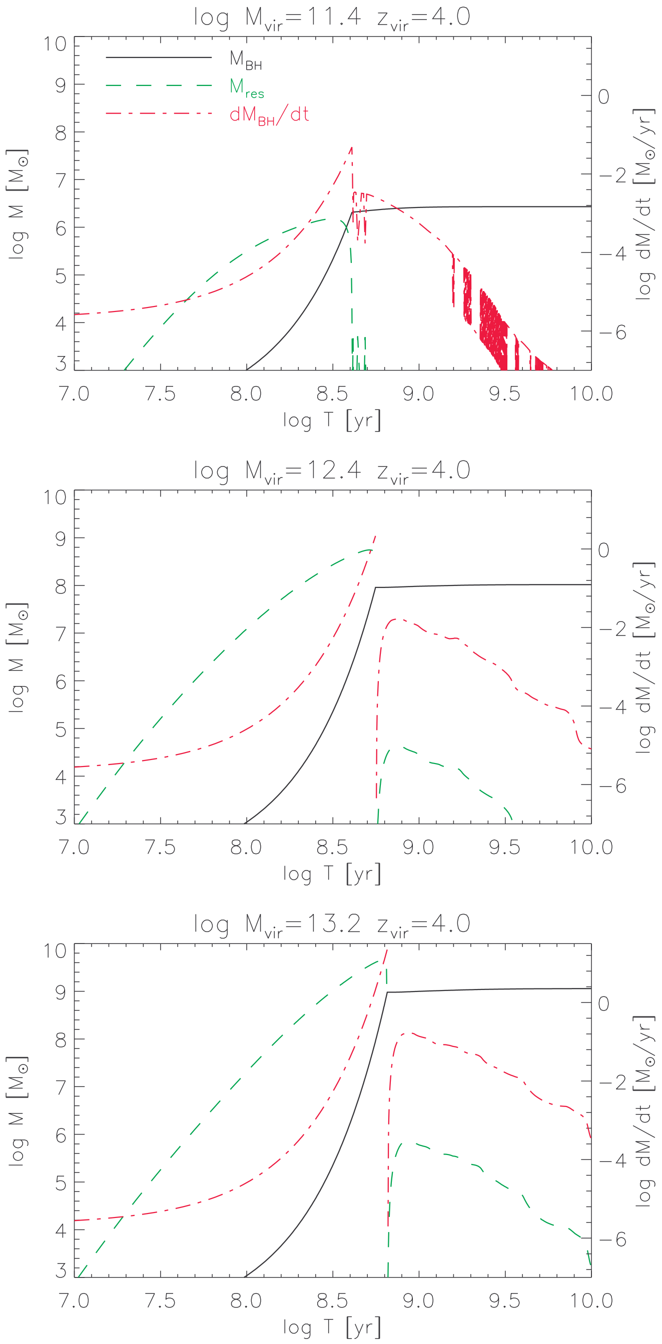

Figure 3.9: Evolution of BH growth, accretion rate and reservoir as a function of galactic age. Three values of M_{vir} at $z_{vir} = 4$ are given as examples.

The fitting is ensured by the dispersion of 0.3 dex associated to the $M_{bh} - M_{halo}$ relation. Fig 3.13 shows the effects with different scatter. The cut-off of halo mass would yield a drastic drop so that introducing a Gaussian scatter is required for a global fit. It is also noted that $M_{bh} - M_{vir}$ formula with the scatter of 0.3dex is original from $M_{bh} - \sigma$ relation as mentioned by Wyithe & Loeb (2005). It could be redshift dependent, implying the imprint of halo evolution on the black hole mass.

The optical luminosity function at $z = 2$ and $z = 1.5$ are shown in the Fig 3.14 and Fig 3.15 respectively. Since hard X-ray photons produced by the QSOs are much less absorbed than UV photons, the hard X-ray emission from the growing black holes is more easily detected. Therefore, the X-ray luminosity functions in the Fig. 3.16 and Fig. 3.17 need the visible time about 3.0×10^8yr, which is larger than that of optical band.

The last plot in Fig 3.18 is about the black hole mass function. The result agrees well with observations, showing that at $0.5 \le z \le 1.5$ QSO of relatively low luminosity($L_X \le 3 \times 10^{44} ergs/s$) provide about 60 percent of the X-ray background(Ueda et al. 2003).

During the process, we allow the Eddington ratio to be a varied parameter with redshift to fit the data as: $\lambda = 4$ for $5 \le z \le 6$, $\lambda = 1.7$ for $3 \le z \le 5$, $\lambda = 1$ for $2 \le z \le 3$ and $\lambda = 0.8$ for $1.5 \le z \le 2$. The empirical fit is $\lambda(z) = 0.75(1 + z) - 1.15$. The super-Eddington accretion is discussed in the section 3.1.4. Since the QSOs at high redshift are bright to be observed so that the value of accretion ratio must be large to fit the observation. It is also indicate that at high redshift universe the accretion for black hole growth and galactic formation could be violent with the small timescale. The mean accretion rate increasing with the redshift has been also noticed by investigation the model of cosmological accretion history(Miller et al. 2006). The observational example for the super-Eddington accretion is given in the Section 3.4.2.

As mentioned in the section 2.11, faint end of AGN Luminosity function is still under debate especially at high redshift(Schirber & Bullock 2003; Lidz et al. 2005). It is noted that the unified model for coevolution of AGN and galaxies has been studied by Hopkins et al.(2005a-g) as a series of papers. The AGN lifetime as the function of instantaneous and peak luminosity is derived from the simulations. AGN luminosity functions are divided into bright end which is traced by peak activity, and faint end which consists of QSOs that are either undergoing exponential growth to much larger mass and luminosities or in sub-Eddington states going into or coming out a period of peak activity. From this result, the evolution of faint end luminosity function is associated with the black hole growth, but not decided by the black hole distribution even they grow as an anti-hierarchical behaviour. However, in our model, we derive AGN luminosity from the dark halo distribution and black hole mass function. Therefore, during the whole life of AGN activity, at certain redshift, the luminosity and black hole mass has the extreme relation of one-to-one. The AGN lifetime is a given value to fit the AGN luminosity function. The time delay and feedback processes reproduce the downsizing behaviour.

In this model, we successfully fit the AGN luminosity functions at redshift 1.5-6, indicating that the number of dark halo or black hole at high redshift should be suitable to give the complete information about the AGN activity. In fact, the key point of this program is to arrange the mass distribution and luminosity distribution by a proper way.

3.3.4 Host galaxy properties

The model interfaced to the code GRASIL[2](Silva et al. 1998) provides also galactic properties including dust effects. In halos with mass less than $10^{12}M_{\odot}$, the interplay between black hole growth, accretion and feedback limits the star formation rate and a substantial amount of stars is formed even after the peak of black hole activity. Oppositely, for those galaxies in the halo larger than $10^{12}M_{\odot}$, the feedback from AGN will stop star formation in a short time during the peak of black hole activity. Since there would be full of gas and dust in the halo before the peak of AGN activity, almost all the associated power is emitted in the infrared and submm band. The galaxy issues can be reproduced as performed by Silva et al. (2005) so that the AGN luminosity functions and the host properties are consistent each other. More details will be presented in the next Chapter.

---

[2] http://web.pd.astro.it/granato

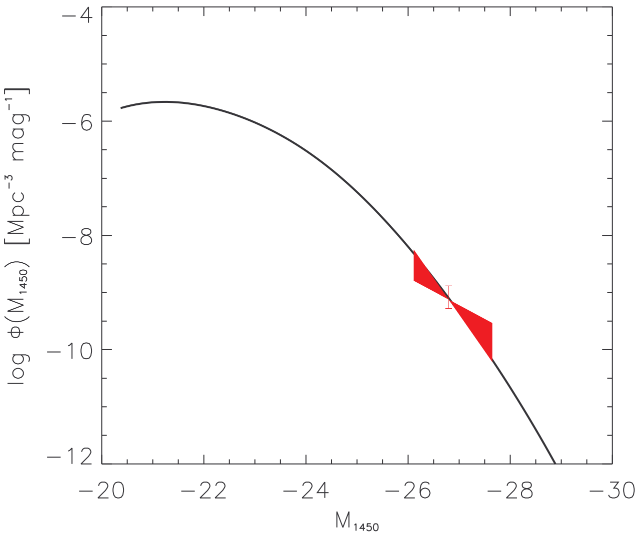

Figure 3.10: AGN luminosity function of optical band at $z = 6$ with visible time of 5.0×10^7 yr. The data are taken from Fan et al. (2004).

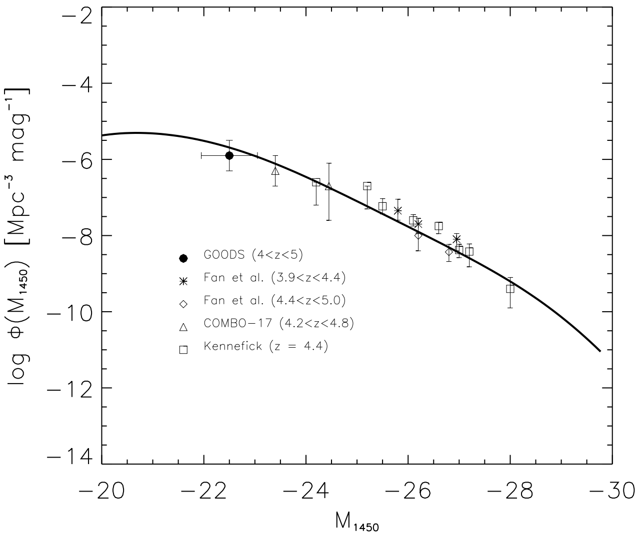

Figure 3.11: AGN luminosity function of optical band at $z = 4.5$ with visible time of 5.0×10^7 yr. Data points are from Kennefick et al. (1995, open squares); Wolf et al.(2003, triangles); Cristiani et al. (2004, circles); Fan et al. (2001, diamonds and asterisks).

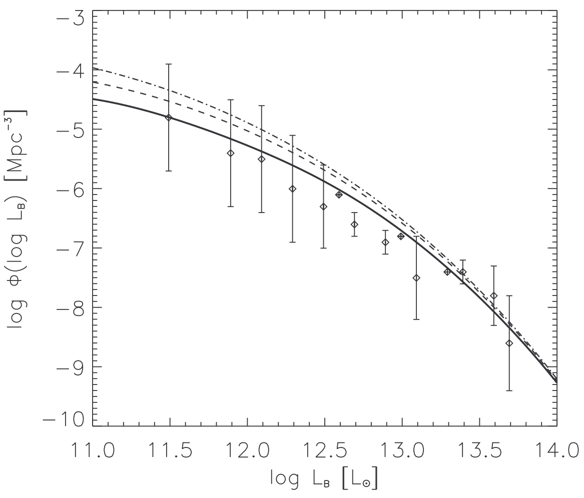

Figure 3.12: AGN luminosity function of optical band at $z = 3$ with visible time of 5.0×10^7 yr(Solid line). The data are taken from Pei (1995). Dashed line is with visible time of 1.0×10^8 yr and dot-dashed line is with visible time of 3.0×10^8 yr. The observational data are taken from Pei (1995).

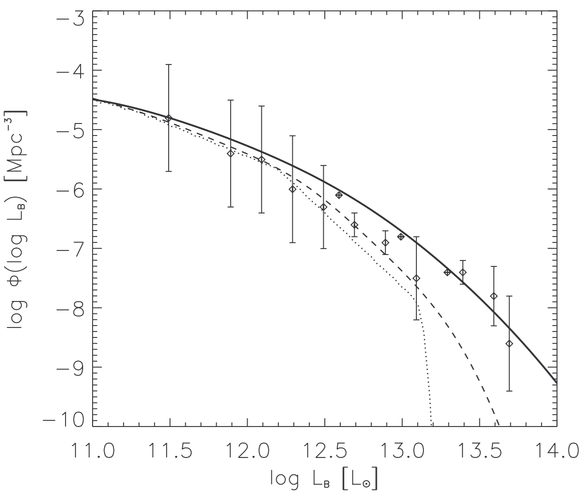

Figure 3.13: AGN luminosity function of optical band at $z = 3$ with visible time of 5.0×10^7 yr. The data are taken from Pei (1995). Solid line is for the scatter of 0.3 dex, Dashed line with 0.15 dex and dot line with no scatter at all.

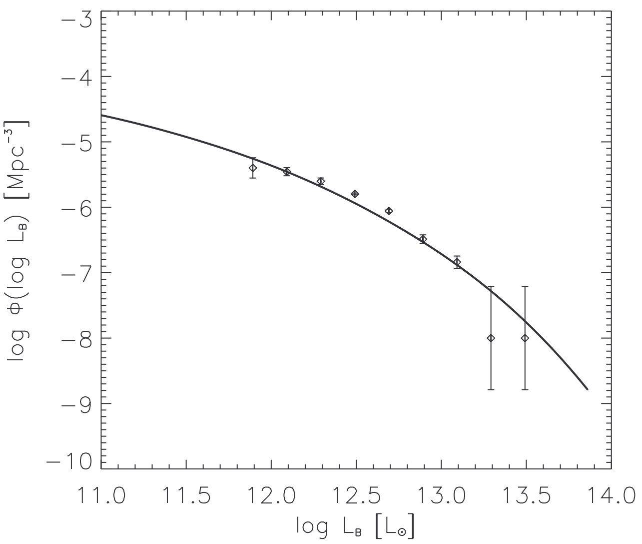

Figure 3.14: AGN luminosity function of optical band at $z = 2$ with visible time of 1.0×10^8 yr. The data are taken from Croom et al. (2004).

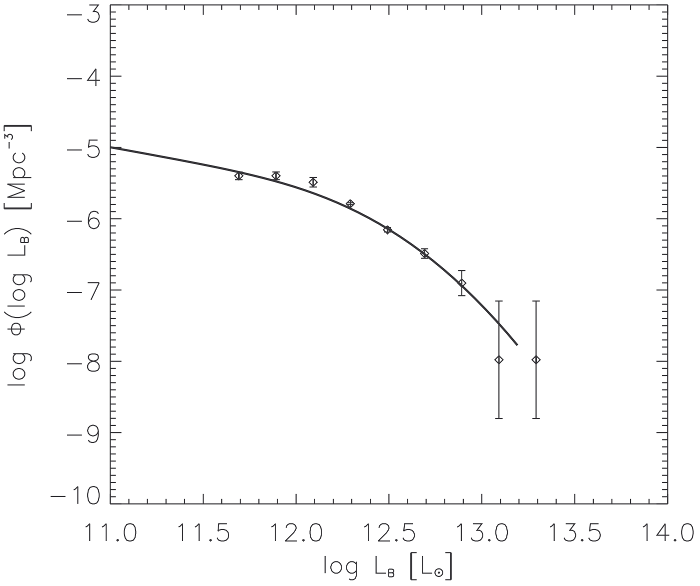

Figure 3.15: AGN luminosity function of optical band at $z = 1.5$ with visible time of 1.0×10^8 yr. The data are taken from Croom et al. (2004).

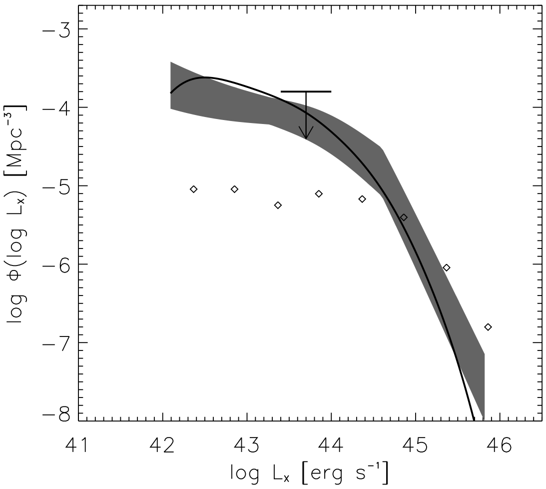

Figure 3.16: AGN luminosity function of hard X-ray band at $z = 2$ with visible time of 3.0×10^8 yr. The data of shaded area are taken from Ueda et al. (2003). The data labeled by diamonds are taken from Bager et al. (2005) for all type AGNs. The upper limit is given from La Franca et al. (2005).

Furthermore, the coevolution model also give the chance to study the dynamic properties of galaxies. Unlike luminosity functions, the distribution of internal velocity dispersions or circular velocities(Sheth et al. 2003) does not depend on waveband. On the other hand, the Faber-Jackson relation(Faber & Jackson 1976) and Tully-Fisher relation(Tully & Fisher 1977) linked the luminosity and dynamic properties together. As examples, in the Fig. 3.19 and Fig. 3.20, the velocity dispersion function and Faber-Jackson relation are presented. These dynamic properties of galaxies, plus the AGN luminosity functions, make up the complete scenario for the galactic formation and evolution.

3.3.5 Conclusion and Discussion

In this chapter, the model of optical and X-ray AGN luminosity functions has been built under the scenario of Granato et al. (2004) and the results are well consistent with the observational data. Due to the time delay and feedback processes, the dark halo/black hole mass distribution and luminosity distri-

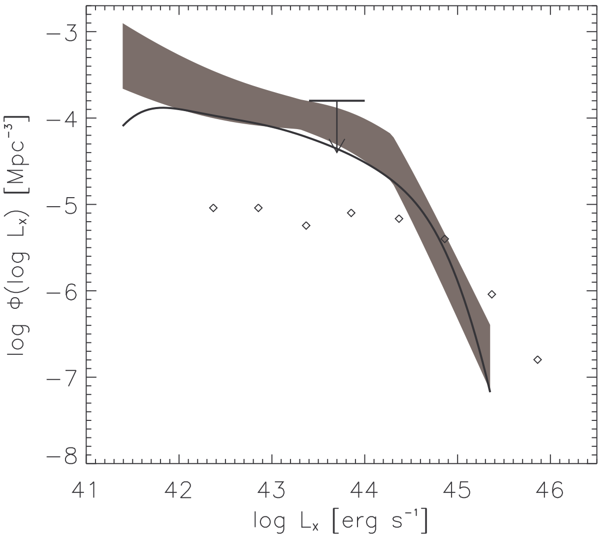

Figure 3.17: AGN luminosity function of hard X-ray band at $z = 1.5$ with visible time of 3.0×10^8 yr. The data of shaded area are taken from Ueda et al. (2003). The data labeled by diamonds are taken from Bager et al. (2005) for all type AGNs. The upper limit is given from La Franca et al. (2005).

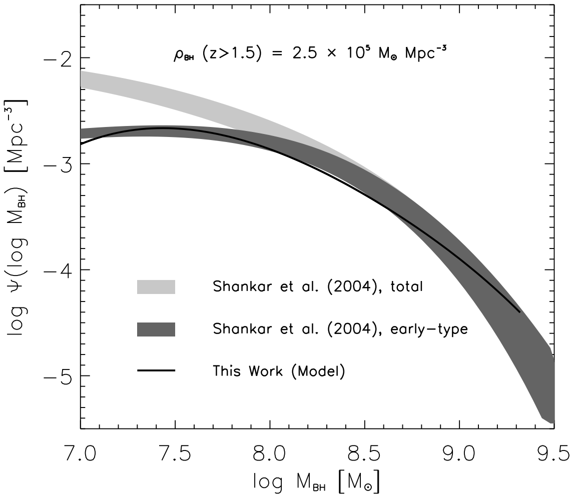

Figure 3.18: Supermassive black hole mass function.

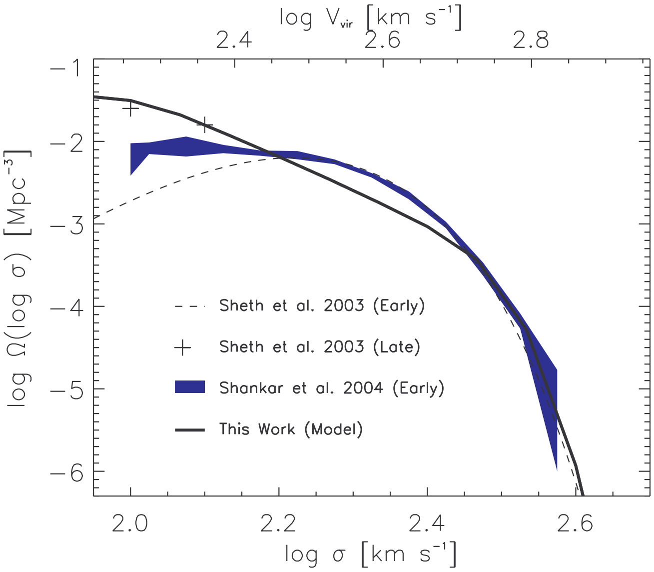

Figure 3.19: Velocity Dispersion Function of Galaxies

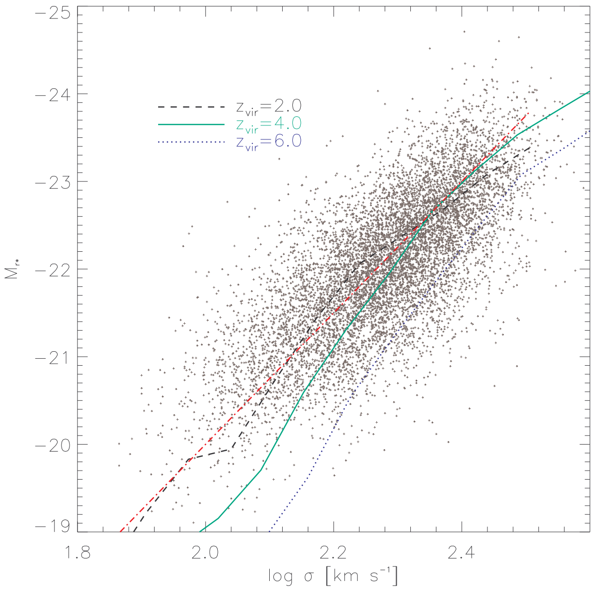

Figure 3.20: Faber-Jackson Relation with Different z_{vir} The data points are from Bernardi et al. (2003a) of SDSS observation.

bution are arranged by a proper way to show the typical anti-hierarchical or downsizing feature.

The important parameters are listed in the Table 3.1. Note that the current set of parameters differs from the one adopted in Granato et al. (2004), but the general scenario and main results are essentially unaffected. The initial mass function(IMF) and metallicity will be discussed in the next Chapter.

The accretion rate onto the central BH has been taken to be at most slightly super-Eddington, as expected when it is limited by radiation pressure(Small & Blandford 1992; King & Pounds 2003). Observational evaluations of the Eddington ratio for high luminosity QSOs with $L \geq 10^{47} ergs\ s^{-1}$ at redshifts $z \geq 2$ have been obtained by Warner, Hamann & Dietrich (2004) and Vestergaard (2004). These authors find a significant fraction of QSOs radiating at mildly super-Eddington powers. Recently, Netzer & Trakhtenbrot(2006) also find that for a given black hole mass Eddington ratio is a function of redshift within the SDSS type-I sample of redshift $z \leq 0.75$. On the other hand, at lower redshifts and luminosities the emission seems to be limited to $\lambda \leq 1$(McLure & Dunlop 2004; Kollmeier et al. 2006). Note that these results are to be taken cautiously. In fact, they are based on the observed FWHM of the H, MgII and CIV broad lines and on an empirical relation linking the size of the broad-line region to the QSO luminosity. On top of that, a normalization to the $M_{BH} - \sigma$ relation is needed to set the scaling factor in the equation yielding the BH mass. This coefficient depends crucially on the kinematic and geometrical properties of the broad line region itself(Onken et al. 2004). Thus the inferred Eddington ratios suffer from large observational and systematic uncertainties, which amount to a factor of up to 10 on individual objects, and up to 4 on statistical samples(Vestergaard & Peterson 2006). In our model a variation of the Eddington ratio with the redshift is necessary to fit the QSOs luminosity functions. From the theoretical view, a major improvement could be obtained by taking into account the results of the photon trapping theory(Blandford 2004) so that the radiative emissions close to Eddington can be originated by strongly super-Eddington accretion rates(e.g., those allowed in our model by viscous accretion). However, details of the mechanism are still uncertain and additional work is needed to quantitatively include it in our model. Non-radiative accretion may also speed up the BH growth and the values of the Eddington ratio could have a substantial scatter due to different environmental conditions around the supermassive BHs. As a result, the samples of high redshift QSOs may be biased towards higher Eddington ratios. Anyhow, the observation and the model of super-Eddington accretion could be studied deeply in the future work.

Alternatively, traditional hierarchical formation is sill going on. Under the effects of supernova and AGN feedback, the typical hierarchical formation can also give the good explanation for the observational anti-hierarchical or downsizing phenomenon(Hopkins et al. 2005d,e; De Lucia et al. 2005; Scannapieco, Silk & Bouwens 2005; Bower et al. 2006). The formation of $z \sim 6$ QSOs from hierarchical galaxy mergers has been produced by the numerical simulations(Li et al. 2006). Recently, the observation(van dokkum 2005) and simulation(Naab, Khochfar & Burkert 2005; Kawata et al. 2005) model of dry merger have been mentioned and the hybrid formation(Ogando et al. 2005) have been proposed, providing other clues to solve the problem. All these models need to be investigated furthermore and be constrained by the future observations.

3.4 Beyond Luminosity Function

3.4.1 AGN Research by Spitzer Space Telescope

The Spitzer Space Telescope[3] carries an 85-centimeter cryogenic mirror and three cryogenic-cooled science instruments(Infrared Array Camera(IRAC), Multi-band Imaging Photometer for Spitzer(MIPS) and Infrared Spectrograph(IRS)) capable of performing imaging and spectroscopy in the 3.6 to 160 micron range.

The IRAC is a four-channel camera that provides simultaneous $5.17' \times 5.17'$ images at 3.6, 4.5, 5.8 and 8 microns. All four detector arrays in the camera are 256×256 pixels in size, with a pixel size of about 1.2 arc second.

---

[3] see the web-page of ssc.spitzer.caltech.edu and the Spitzer observer's manual version 3.0

The MIPS is designed to provide photometry and super resolution images in broad spectral bands centered at 24, 70 and 160μm. The two shorter bands provide roughly 5' square filed of view and the 160μm array provides the filed of view of $0.5' \times 5'$. The IRAC and MIPS are extremely important for the Spitzer Wide-area Infrared Extragalactic Survey(SWIRE; Lonsdale et al. 2003) as a part of the GOODS.

SWIRE gives a special attention to the topics of AGN. First, many AGNs have warm mid-to-far-infrared colors compared to the star formation dominated galaxies so that AGNs could be selected by the highly sensitive 8 and 24μm bands; Second, IR band is a powerful tool to determine the evolving number density of AGNs particularly to the evolution of the obscured AGN population; Third, understanding the starburst-AGN connection from infrared view could be interesting for the AGN-galaxy coevolution.

The initial results has been found by the Spitzer observation: extragalactic number counts of near-IR 3-10μm (Fazio et al. 2004), middle-IR at 24μm(Marleau et al. 2004), far-IR of 70μm and 160μm(Dole et al. 2004) have been obtained respectively. Based on the IRAC color-color diagrams

Table 3.1: The parameters in the model

Parameter	Value	Short description
c	7	clumping factor
τ_0	1	normalization of optical depth
ϵ_{SN}	0.05	efficiency of SN feedback
ϵ_{QSO}	1.3	efficiency of QSO feedback
M_{seed}	10^2 solar mass	mass of seed black hole
k_{accr}	10^{-3}	efficiency of viscous accretion
α_{BH}	2.5	efficiency of radiation drag
η	0.15	radiative efficiency
λ	0.8-4	Eddington ratio
Optical t_{vis}	$5.0 \times 10^7 yr$	visible time/lifetime in optical band
X-ray t_{vis}	$3.0 \times 10^8 yr$	visible time/lifetime in hard X-ray band
ΔM_{bh}	0.3 dex	$M_{bh} - M_{halo}$ scatter

of the Spitzer first look survey, the AGN candidates are distinguished from other star-forming sources(Lacy et al. 2004), half of the AGN candidates are suggested to be obscured AGNs determined by the middle infrared colors. Both type 1 and type 2 AGNs have the clear relation between the mass of the central black hole M_{BH} and infrared $10\mu m$ luminosity(Alonso-Herrero et al. 2002), so that the infrared $10\mu m$ emission could be the powerful tool for conducting a census of BH mass at high redshift and probing the cosmological evolution. The sample of $z > 4$ quasars has about 100 times stronger near-IR emission than the AGN at low redshift(Wilkes et al. 2000). Recent Spitzer observation for the QSOs at high redshift indicates that these QSOs will be very difficult to identify because they are viewed along the dust-obscured sight lines(Hines et al. 2006). More investigations will be dependent on the multi-band observation.

3.4.2 Multi-band Observation and NLSy1 Population

Multi-band observation provides the excellent chance to investigate the AGN evolution and central black hole growth. In the local universe, the good correlation between near infrared 4.8/9.7 μm and hard X-ray fluxes for both Seyfert 1s and Compton thin($N_H \leq 10^{24} cm^{-2}$) Seyfert 2s has been found(Alonso-Herrero & Quillen 2001). The values of the ratio(IR/X) between infrared $24\mu m$ and the X-ray flux(0.5-2keV) were already given from the Chandra and ISO data(Weedman et al. 2004) at the redshift $1 < z < 3$. For the starbursts, IR/X is determined to have the mean value of 1.3 and the sources with $IR/X < 0.2$ probably are dominated by AGNs. From the Spitzer data available, we can distinguish between starbursts galaxies and the AGNs by putting the X-ray emission and $24\mu m$ infrared data together(Alonso-Herrero et al. 2004). Moreover, the universal correlation among black hole mass, $2-10$keV($0.1-2.4$keV) X-ray luminosity and 5GHz (1.4GHz) radio luminosity of AGN has been found(Merloni, Heinz & Di Matteo 2003; Wang, Wu & Kong 2006; but see also Bregman 2006). It is so called the fundamental plane of black hole activity. The fundamental plane of black hole activity is used as a mass and accretion rate estimator to review the growth of super-massive black holes and obtain the black hole mass function(Merloni 2004). The results are: the evolution of the black hole mass function between $z = 0$ and $z = 3$ shows the anti-hierarchical behavior; The majority of the most massive objects were already in place at $z = 3$, lower mass ones mainly grew at progressively lower redshift, so that the average black hole mass increases with the redshift.

The obscured AGNs are predicted to be particularly bright in the middle infrared due to the re-emission from X-ray and UV absorption by the dust. However, the develop study for $24\mu m$ properties of X-ray selected AGN has been done(Rigby et al. 2004). The expectation that harder AGN should be relatively brighter at $24\mu m$ is not confirmed. The AGN evolution especially the obscured AGN evolution could be still an open question.

On the other hand, as concentrated on AGN luminosity function in the section 3.3.3, the super-Eddington accretion is the vital phase during the black hole growth. Mclure & Dunlop(2004) pointed out that the black hole growth could be limited not by the Eddington accretion but by some other physical limit on fuel supply which prevents accretion rates significantly in excess of $10M_{\odot}yr^{-1}$. Such a physical limit might be imposed by accretion disc viscosity(Burket & Silk 2001) or by the physics of galaxy formation(Archibald et al. 2002; Granato et al. 2004). Observational evidences have shown that, the narrow-line Syfert 1 galaxies(NLSy1) or narrow-line type 1 QSOs could be the exact candidates of the objects with supper-Eddington accretion(Kawaguchi, Pierens & Huré 2004, Kawaguchi et al. 2004). This special population is also viewed as young AGN(Grupe 2004) which may undergo a state transition from a radiative inefficient accretion flow to an optical thick and geometry thin disk or radiation pressure supported slim disk(Greece, Ho & Ulvestad 2005). The sample from soft X-ray selected(Grupe et al. 2004) objects and SDSS(Zhou et al. 2006) observation have been prepared, the radio-loud type 1 QSOs(Komossa et al. 2006) have been found and host galaxies of NLSy1s(Deo, Crenshaw & Kraemer 2006) have been archived. Beside the phenomenology, more physical understanding may be revealed to the detailed physics of black hole growth and the galaxy formation in the future.

Chapter 4

Reionization by High Redshift Galaxies

Followed by the coevolution model(Granato et al. 2004) between AGN and galaxies, the AGN luminosity function has been derived in the Chapter 3. Although at $z < 2.5$ the UV ionizing background is dominated by QSOs(Haardt & Madau 1996), due to the rapid decline of AGN population at high redshift, the contribution of QSOs to the ionizing background is less than 30% of that from star-forming galaxies(Fan, Carilli & Keating 2006). Therefore, most theoretical models assume that stellar sources reionize the universe. In this Chapter, we focus on the properties of high redshift galaxies, especially on the global star formation and their contribution to the reionization. Section 4.1 is the observational description of Gunn-Peterson effect and CMB polarization; The key points for galactic evolution, such as initial mass function(IMF), star formation rate(SFR) and chemical evolution, are mentioned in the Section 4.2; The realistic work begins from the fitting of luminosity function for LBGs in the Section 4.3, the star formation history and UV background have been obtained consequently in the Section 4.4; The galactic timescale which is about 10^7 years of the beginning phase of primordial galaxies, has been calculated by fixing the certain mean metallicity, thus the reionization epoch can be determined in the Section 4.5; The discussion issues are presented in the Section 4.6, we propose that the protogalaxies contributed to the reionization have been followed by the stage like SCUBA behavior; Finally, as the complete discussion, some hot topics such as the IR background, the PopIII stars and HI 21cm features, are described respectively in the Section 4.7.

4.1 Introduction: Observational Features

4.1.1 High Redshift QSO Spectrum

The first light completes so-called dark ages which is from the recombination at redshift about 1100 to the reionization epoch. The reionization epoch is the transition phase of intergalactic medium(IGM) from neutral to ionized state.

High redshift QSOs are the possible objects to identify the transition epoch at high redshift universe. Due to strong Lymanα absorption, the spectrum of high redshift QSO may show a clear Gunn-Peterson trough(Gunn & Peterson 1965). The Gunn-Peterson optical depth is given by(Fan et al. 2002; 2006):

$$\tau_{GP}(z) = 1.8 \times 10^5 h^{-1} \Omega_M^{-1/2} (\frac{\Omega_b h^2}{0.02}) \times (\frac{1+z}{7})^{3/2} (\frac{n_{HI}}{n_H}) \tag{4.1}$$

Since only a small fraction of neutral hydrogen component in IGM is required to have $\tau_{GP} > 1$ and show a complete trough, it does not prove that this object is observed around the reionization epoch. However, the fast evolution of the mean absorption suggests that the mean ionizing background along the line of sight has declined significantly from redshift 5 to 6, indicating the reionization epoch at $z \sim 6$(Becker et al. 2001; Fan et al. 2002; White et al. 2003; Fan et al. 2006).

However, it is also noticed that, for the particularly source such as SDSS J1148+5241 at redshift 6.42, the detectable flux is still visible in the Gunn-Peterson trough(White et al. 2003). One explanation is that this flux is emitted by the interloper galaxy. Oh & Furlanetto (2005) measured Lyman γ trough and declared that the flux may be due to the QSO itself. More technique discussion for measurement of QSO spectra is presented by Lidz, Oh & Furlanetto (2006). Recently, the nature and evolution of the highly ionized HII front zones around QSOs at redshift 6 have been discussed in detail by analytic formula and simulation(Bolton & Haehnelt 2006), it is still difficult to determine whether the surrounding IGM is neutral or ionized.

4.1.2 CMB Polarization by WMAP

Due to gravitational instability, the small fluctuations in the early universe grow to the large structure. At redshift about 1100, the Cosmic Microwave Background(CMB) photons decoupled with the baryons. CMB photons show temperature anisotropies as the relic of primordial fluctuations. Reionization produces free electrons which could scatter CMB photons. Thomson scattering produces CMB polarization only when free electron scatters are illuminated by an quadrupole anisotropic photon distribution. Therefore, CMB polarization probes the evolution of the decoupling and reionization epochs(Hu & White 1997). The polarization signal was produced as E-mode owing to its symmetry properties under parity transformation(Zaldarriaga & Seljak 1997) while the anti-symmetric component of CMB polarization is referred as B-mode which arises in inflation and predict a primordial gravitational wave background. Note that CMB polarization does not experience the integrated Sache-Wolfe effect, but gravitational lensing of large scale structure may convert E-mode power into B-mode(Zaldarriaga & Seljak 1998).

The measurement of CMB polarization by the first-year Wilkinson Microwave Anisotropy Probe(WMAP) has obtained the scattering of optical depth $\tau = 0.17 \pm 0.04$(Kogut et al. 2003), implying a reionization redshift of 17 ± 5(Spergel et al. 2003). From recent polarization analysis of 3-year WMAP observation(Page et al. 2006), comprising Stokes I, Q and U components, the maximum likelihood estimates provide the noise characteristics of the sky map(Jarosik et al. 2006). After correction of the measurement uncertainties including system errors and the foreground emission by Galactic synchrotron radiation and dust emission(Page et al. 2006), finally, the optical depth is constrained as $\tau = 0.09 \pm 0.03$ and the reionization epoch is at redshift $z \sim 10.9$ (Spergel et al. 2006).

4.2 Blocks of Galactic Evolution

4.2.1 Initial Mass Function

The initial mass function(IMF) is the relative birth rate of the stars with different initial mass in a certain mass interval. The simple power law of normalized IMF was given by Salpeter(1955) as the form:

$$\phi_m = 0.17m^{-2.35} \tag{4.2}$$

where $0.1M_\odot < m < 125M_\odot$. Another popular multi-slope IMF was produced by Scalo(1986). The Scalo law is flat at small mass and less rich of massive stars with respect to that of Salpeter. From the constraints of star formation and galaxy luminosity densities, other modified power-law index varied with different stellar mass range are proposed(Kroupa 2001; Baldry & Glazebrook 2003) in the local universe. Larson (1998) suggested a top-heavy stellar IMF particularly for the early Pop III star formation. This kind of IMF can be constrained by the UV background and reionization observation(Schneider et al. 2006). Beside these IMF models, the double-slope form(Romano et al. 2002) as $\phi_m \propto m^{-1.4}$ for $m \leq 1M_\odot$ and $\phi_m \propto m^{-2.25}$ for $1M_\odot < m \leq 100M_\odot$ was used in the model of Granato et al. (2004).

In principle, the physical origin of IMF is the complex process of star formation from the molecular cloud which may suffer a hierarchical fragmentation process(Zinnecker 1984). The fragmentation begins from the gravitationally instability disturbed by turbulent flow and shocks(Padoan & Nordlund 2002). The cloudlets fall into the center region, their masses exceed the critical mass so that they turn to form the pro-stellar cores(Murray & Lin 1996). The slope of the IMF at high masses may depend on the dispersion in the accretion rates of protostars(Bate & Bonnell 2005). Mergers of the binary systems can also lead to the formation of the most massive stars(Bonnell & Bate 2005). One kinds of feedback, protostellar outflows, may be responsible for the shape of IMF(Silk 1995). All of these processes can be combined altogether and influence the final IMF form.

Practically, for masses above $1M_\odot$, the IMF can be reproduced with a slope similar to that of Salpeter(1955). Accretion may be responsible for the massive star formation and upper IMF limit. Although fragmentation could be the major process for the IMF shape on the small mass part, the slope is still varied with a wide range(Bonnell, Clarke & Bate 2006; Bonnell, Larson & Zinnecker 2006, Larson 2006).

4.2.2 Star Formation Rate

Star Formation Rate(SFR) is the star-forming mass as the function of evolving time. Normally, it is presented as a exponential function of:

$$\psi(t) \propto e^{-t/t_*} \tag{4.3}$$

where t_* is about 5 to 15 Gyr. For the IMF of Salpeter, the relation between SFR and the ultraviolet luminosity of the galaxies at $1500\mathring{A}$ has been provided by Madau, Pozzetti & Dickinson(1998):

$$L_{UV} = 8.0 \times 10^{27} \times \frac{SFR}{M_{\odot} yr^{-1}} ergss^{-1}Hz^{-1} \tag{4.4}$$

There are at least two methods to obtain the cosmic star formation history. One way is to directly observe an area of the sky. The indicators of SFR are H-alpha emission line from HII regions of local universe(e.g., Gallego et al. 1995), metal density produced by type II SNe(Madau et al. 1996) or UV continuum and infrared continuum(Donas et al. 1987). From the observational point of view, the global SFR history of low redshift has been well established(e.g., Hogg et al. 1998; Cowie et al. 1999; Flores et al. 1999; Wilson et al. 2002). The SFR properties extended to the high redshift universe have obtained large progress from recent deep survey(Steidel et al. 1999; Giavalisco et al. 2004b). Provided by these observational data, the evolution of the star-forming galaxies and the global SFR properties can be well understood(e.g., Hopkins 2004; Hopkins & Beacom 2006).

The other way to obtain the SFR history is by ab initio theory. This method begins from the favorite cosmological model with initial conditions, then uses standard physical equations of gravity, hydrodynamics and radiative transfer etc., finally simulates the whole history of the universe, in which the SFR history is obtained(e.g., Springel & Hernquist 2003; Nagamine et al. 2004, 2006a). A detail comparison is given by Nagamine et al. (2006b).

In this thesis, we derive the SFR as following: in a given dark halo, the diffuse gas in the outer region infalls into the center and turns into the galaxies and stars, through the maximum value between dynamic timescale and cooling timescale. The stars form faster in the larger dark halos controlled by the dynamic timescale, as shown in the model of Granato et al. (2004). The SFR can be expressed as:

$$\psi(t) = 32(M_{gas}/10^{11}M_{\odot})(1+z)^{3/2}M_{\odot}yr^{-1} \tag{4.5}$$

Suppose SFR in each halo mass at each redshift is given, both global SFR density and UV band luminosity density ρ_{UV} can be achieved. Since the SFR value in the Eqs. 4.5 is larger than the average number, this equation is particularly adopted for those star-forming galaxies.

Finally, It is important to point out that Gamma-ray burst(GRB) is tightly associated with the SFR at high redshift. GRB, as the most violent stellar activity, with extremely intrinsic energy releasing, has been studied as two types, short burst(gamma band timescale $t < 2s$)and long-burst(gamma band timescale $t > 2s$)(Piran 1999). It is noticed that long bursts could be the unbiased tracers of star formation(Jakobsson et al. 2005; Fynbo et al. 2006) and the potent tools for the study of IGM(Watson et al. 2006; Bromm & Loeb 2006a,b) in the early universe. The Population III stars, with mass of several hundred to one thousand solar mass and nearly zero metallicity, are thought to be tightly linked with GRBs. The preliminary studies of prediction SFR history from $z > 7$ and the distribution of long-burst GRBs have been performed(Bromm & Loeb 2006a).

4.2.3 Chemical Evolution: Outline

In the total system, there are several basic variables such as mass of gas, mass of stars, dust production and initial chemical abundance Z. It is assumed that all progress involving stellar evolution and recycling occur instantaneously on the timescale of galactic evolution.

Under the standard theory of stellar evolution, various chemical compositions and ages of all kind of stars can be determined(Pagel 1997). Given the certain IMF and SFR, one may have the model of chemical enrichment.

The simple way is having a closed-box model, in which no materials either enter or leave the focused region. The assumption could be: (1) the system is isolated with a constant total mass, no inflows and outflows; (2)the system begins with a primordial abundances; (3) the system is mix during the evolution and (4) IMF does not change with the time.

Since we know there are different stars with a widely range of ages in the whole system, where the chemical abundances evolve with the time, to study the whole system, the stellar population synthesis is required. In general, we divide the two characteristic populations from the colors and brightness: Population I, which dominated by luminous blue stars with a full gas and dust environment; Population II, which contains red and metal-poor stars. Open clusters and the galactic disk comprise Pop I stars while globular clusters and ellipticals have rich Pop II stars. The earlier generation, population III stars of heavy initial mass and metal-free, are proposed to appear in the early universe, will be discussed in the Section 4.6.

In reality, the model of stellar population synthesis includes the procedures as the following: (1) determine an initial chemical condition; (2) evolve the population; (3) for each step, obtain the luminosities and colors for all the stars, thus obtain isochrone which means at the color-magnitude diagram for all the stars at the same time. Given the IMF, SFR, synthesis model of Simple Stellar Population(SSP) the spectra library of population synthesis can be built(e.g. Bressan et al. 1993; more complex treatment of evolution was shown, for example, by Buzzoni 1989). With the assumption that there was only a single instantaneous starburst occurred during the cosmic time of galaxies, the outline of passive evolution of galaxies can be obtained. Note that this is the different situation if galactic merger is taken into account as the major process of hierarchical formation.

4.2.4 Galaxy Luminosity Function

The galaxy luminosity function provides the information not only for the statistics of galactic evolutionary process, but also to the contribution of UV photons which is particularly important to the research of reionization at high redshift. The field galaxy luminosity function, as the galaxy numbers in the luminosity range(or magnitude range) per unit volume, is given by(Schechter 1976):

$$\Phi(L) = (\Phi^*/L^*)(L/L^*)^\alpha exp(-L/L^*) \tag{4.6}$$

or the form of absolute magnitude:

$$\Phi(M) = (0.4ln10)\Phi^* 10^{0.4(\alpha+1)(M^*-M)} exp(-10^{0.4(M^*-M)}) \tag{4.7}$$

where parameter L^* is the luminosity corresponding to the absolute magnitude M^*, α is the slope for luminosity function at the faint end and Φ^* is the overall normalization of galaxy density. Thus, the number set(M^*, Φ^*, α) can be used to fit the observational data at given redshift.

In this section, we focus on the observation of galaxies at high redshift. With Lyman break technique, the great progress(Stanway et al. 2004; Yan & Windhorst 2004a,b; Bouwens et al. 2005; Bouwens et al. 2006; Bunker et al. 2006) has been achieved for the detections of i-dropout galaxies from the Great Observatories Origins Deep Survey(GOODS; Dickinson et al. 2004) and Hubble Ultra-Deep Field(UDF; Thompson et al. 2006). Moreover, the narrow-band research(Hu et al. 2004; Taniguchi et al. 2005) can be used for finding Lyman alpha emitters(Malhotra & Rhoads 2004; Kashikawa et al. 2006) while the direct spectroscopic approach based on the slitless spectroscopy(Kurk et al. 2004; Malhotra et al. 2005) and blind slit search(Martin et al. 2006) are also performed.

Therefore, several sets of Lyman-break galaxies at high redshift can be listed. Dickinson et al. (2004) has the set $(-19.87, 0.00527, -1.6)$ from the number counts of GOODS data; Bunker et al. (2004) gets the set $(-20.87, 0.00023, -1.6)$ from number density of UDF; $(-21.03, 0.00046, -1.6)$ comes from Yan & Windhorst (2004a,b) of GOODS observations; the fitting of Bouwens et al. (2006) is $(-20.20, 0.00176, -1.74)$. All the data process are normalized to the luminosity of $1350\AA$ at redshift about 6. The comparison of UV luminosity function is given in Bouwens et al. (2006). For the Lyman alpha emitters, Hu et al. (2004), Shimasaku et al. (2006) and Kashikawa et al. (2006) have obtained their results respectively and the comparison is shown in Kashikawa et al. (2006). These observations of high redshift galaxies give the direct evidences that the end of reionization could be occurred at redshift $6-7$, consistent with the observation of QSO spectrum.

4.2.5 Output of Coevolution Model: Stellar Part

The general description of the model by Granato et al. (2004) has been introduced in the section 3.2.4. Here, we concentrate on the stellar and galactic properties of the output. The baryonic content in a given halo is partitioned in three gaseous phases: a hot diffuse mass infalling or cooling to the center; cold gas condensing into stars; low angular momentum gas stored in a reservoir around black hole and providing accretion materials.

Normally, SFR is given as the total cold gas over the collapse timescale. The collapse time of gas is the maximum between dynamic timescale and cooling timescale. According to the study of the dark halo(e.g., Zhao et al. 2003), the formation of potential well may be rather fast while the baryons associated with the slow accretion take a long time, comparable with the Hubble timescale. The feedback of SNe and AGNs should be also taken into account. Thus, the cooling process does not take into the star formation process as a direct way. Dynamic timescale is viewed to control the star formation as that stars form faster in the massive halos. The result of SFR is presented in the section 4.2.2.

The output provides all kinds of stellar properties. In each halo at each redshift bin, we have the mass of infalling gas, the mass of cold gas, spheroid mass, SFR and metallicity. The example has been shown in the Fig. 4.1. In the large halos at high redshifts, the SFR calculated by Eq. 4.5 is very high, yielding a large production of metallicity and dust. The chemical evolution of galaxies and dust formation are also evolved(Silva et al. 1998), so that we can obtain the mean metallicity value in each halo at each redshift bin. The different evolution stages of spheroids can be predicted as well.

4.3 Rest-Frame UV Luminosity Function of Lyman Break Galaxies

4.3.1 General Case of SFR in Our Model

For massive halos the energy fed back to the galactic gas by BH activity dominates over the energy released by SN explosions only in the last e-folding

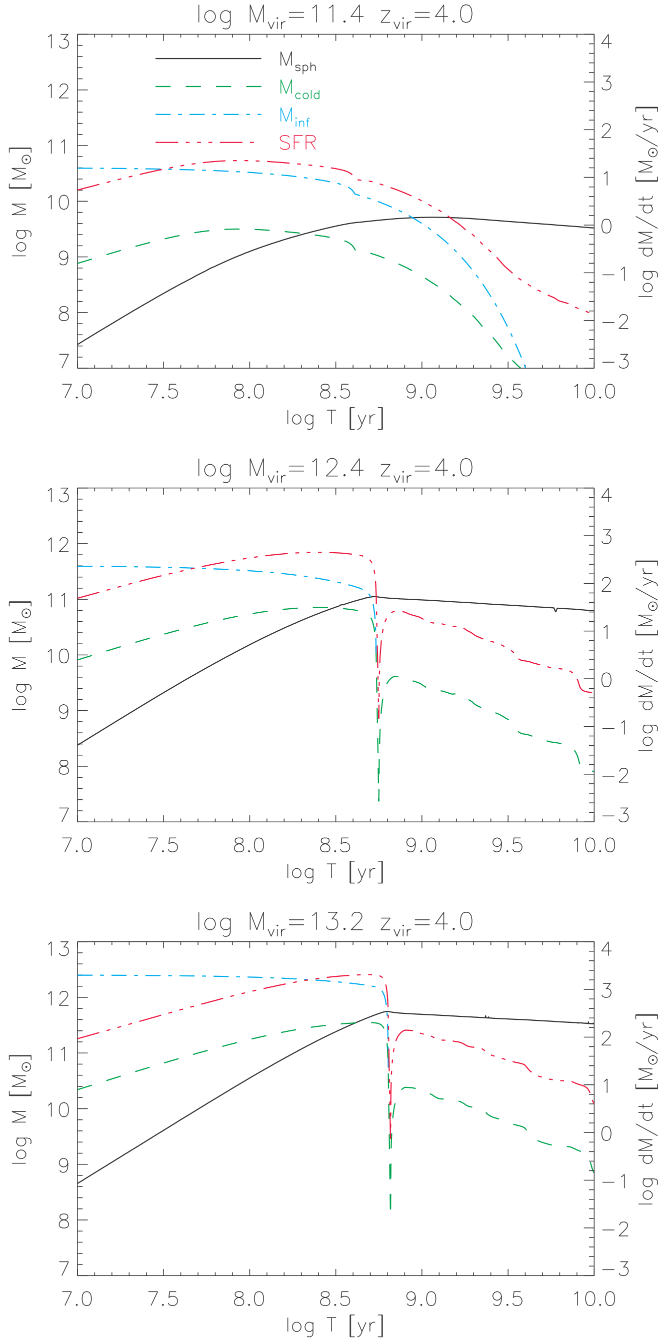

Figure 4.1: Evolution of star mass, cold gas, infalling gas and star formation rate as a function of galactic age. Three values of M_{vir} at $z_{vir} = 4$ are given as examples.

time(i.e. during the QSO phase), and removes all the gas from the halo drastically reducing the star formation. As for the less massive halos, the mutual effects of star formation and gas flow toward the reservoir around the central BH result in a strong decline of the BH mass with halo mass; as a consequence the impact of QSO feedback is much less important and star formation can continue for longer times. The elapsed time can be approximated as:

$$\Delta t_{burst} = 4 \times 10^{8} yr \tag{4.8}$$

for $M_{halo} > 10^{12} m_{\odot}$ and

$$\Delta t_{burst} = 10^{8} (M_{halo}/10^{12} M_{\odot})^{-0.15} [(1+z)/7]^{-1.5} yr \tag{4.9}$$

for $M_{halo} \leq 10^{12} m_{\odot}$.

A nice fitting for the metallicity of the cold, star-forming gas is given by:

$$Z(t) = 10^{-4} (t/10^{7})^{3} \tag{4.10}$$

for $t \leq 5 \times 10^{7}$ yr and

$$Z(t) = 10^{-2} (t/5 \times 10^{7}) \tag{4.11}$$

for $5 \times 10^{7} \leq t \leq min[\Delta t_{burst}, \Delta t_{sat}]$, where $\Delta t_{sat} = 5 \times 10^{7} (M_{halo}/2.5 \times 10^{10})^{0.2}$yr is the time after which Z keeps almost constant.

The Star formation rate and the star mass as the function of time is shown in the Fig. 4.2.

4.3.2 Dust Extinction

Before the fitting of UV luminosity function, we need to treat the dust extinction. Following the results of Calzetti et al. (1994) and Jonsson et al. (2006), the dust extinction is computed as:

$$A_{v} = -2.5 log((1.0 - exp(-\tau_{dust}))/\tau_{dust}) \tag{4.12}$$

where the optical depth of the dust absorption is $\tau_{dust} = 1.7 \times SFR^{0.26}$. Since we know that the larger extinction is required in the massive halo thus affected at higher luminosity part of luminosity function, we improve the dust

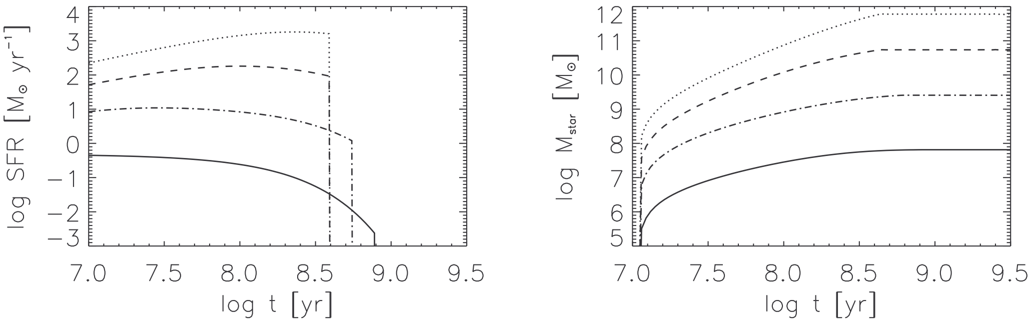

Figure 4.2: Star formation rate(left panel) and star mass(right panel) as the function of evolutionary time for different halo masses $10^{10}M_\odot$(solid line), $10^{11}M_\odot$(dot-dash line), $10^{12}M_\odot$(dash line) and $10^{13}M_\odot$(dot line) virialized at z=6.

attenuation as the function of both star formation rate and the metallicity of the gas. We propose the extinction law as:

$$A_{1350} = 0.35(\frac{\dot{M}_\star}{M_\odot yr^{-1}})^{0.4}(\frac{Z}{Z_\odot})^{0.6} \tag{4.13}$$

where $\dot{M}_\star$ is the star formation rate. From the extinction curve results by Calzetti et al. (2000), we may also use the dust extinction at other wavelength, such as $A_{1216} = 1.1A_{1350}$, $A_{1700} = 0.87A_{1350}$ and extrapolating $A_{912} = 1.6A_{1350}$. The extinction as the function of the time evolution in the certain halo is shown in the Fig. 4.3.

From the star formation, we derive the observed absolute magnitude as:

$$M_{1350} = 51.6 - 2.5log\frac{L_{1350}}{ergs^{-1}Hz^{-1}} - 2.5log\frac{\dot{M}_\star}{M_\odot yr^{-1}} + A_{1350} \tag{4.14}$$

where $L_{1350} = 1.2 \times 10^{28}ergs^{-1}Hz^{-1}$ is the monochromatic luminosity for the IMF of Romoano et al. (2002). Therefore, the extincted magnitude is shown as Fig. 4.4.

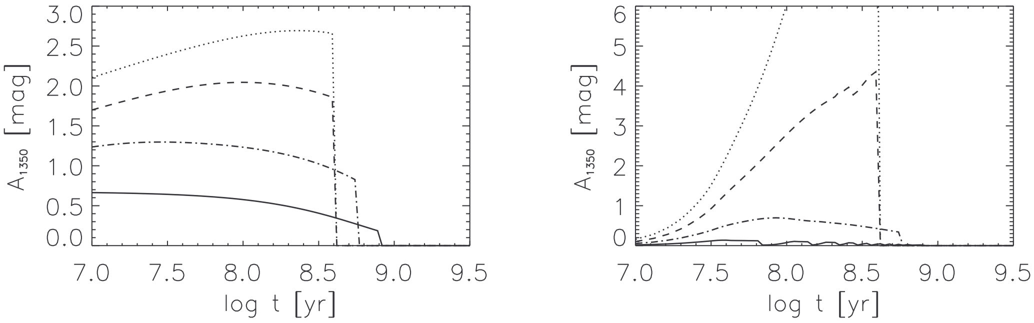

Figure 4.3: Dust extinction at $1350\mathring{A}$ as the function of time for different halo masses $10^{10}M_{\odot}$(solid line), $10^{11}M_{\odot}$(dot-dash line), $10^{12}M_{\odot}$(dash line) and $10^{13}M_{\odot}$(dot line), according to the Eq. 4.12 (left) and Eq. 4.13 (right).

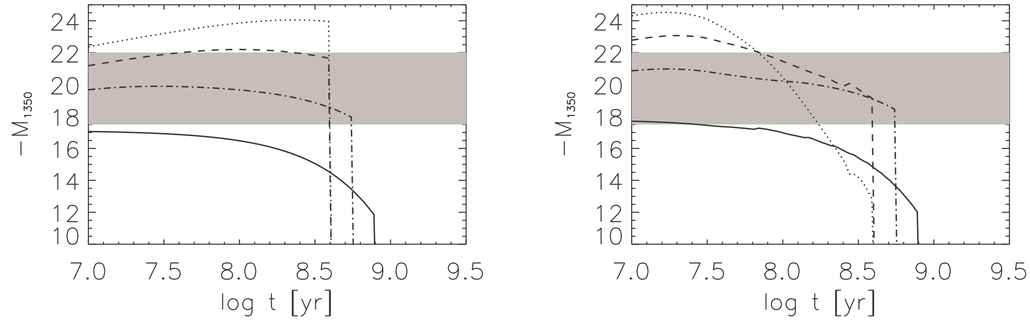

Figure 4.4: Extincted magnitude at $1350\mathring{A}$ as the function of time for different halo masses $10^{10}M_{\odot}$(solid line), $10^{11}M_{\odot}$(dot-dash line), $10^{12}M_{\odot}$(dash line) and $10^{13}M_{\odot}$(dot line), according to the Eq. 4.19 (left) and Eq. 4.20 (right). The shaded area highlights the range probed by the observed UV luminosity functions of Lyman break galaxies.

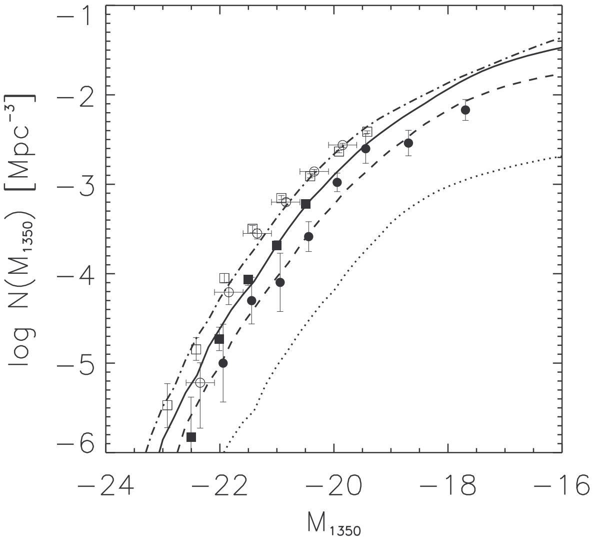

Figure 4.5: Luminosity function of Lyman break galaxies at 1350Å for different redshifts z=5.5(solid), z=3.5(dot-dash), z=7.5(dash) and z=10(dot). Data at z=3 are from Steidel et al.(2001; empty circles), at z=4 from Yoshida et al. (2006; empty squares), at z=5 from Yoshida et al. (2006; filled squares) and at z=6 from Bouwens et al. (2006; filled circles). To convert the Steidel data from 1700Å to 1350Å, we use the prescription $M_{1350} = M_{1700} + 0.2$.

4.3.3 UV Luminosity Function of Lyman break Galaxies

The rest-frame UV luminosity function at cosmic time t is obtained as:

$$\Phi(M_{1350}, t) = \int dM_{halo} \frac{d^2 N_{st}}{dM_{halo} dt} \frac{d}{dM_{1350}} \tau[M_{1350}|M_{halo}, t] \tag{4.15}$$

where $\tau[M_{1350}|M_{halo}, t]$ is the time lapse spent at magnitude higher than the level M_{1350}. After the consideration of dust extinction of Eq. 4.13, we obtain the luminosity function of Lyman break galaxies shown as Fig. 4.5.

4.4 Cosmic SFR History

4.4.1 Results of Dust-Free Assumption

The star formation and UV background has been studied in detail at low redshift(e.g., Bianchi, Cristiani & Kim 2001; Buzzoni 2002). In this section, we explore it to the early universe and concentrate its effect on the reionization.

Followed the output of the model by Granato et al. (2004) which provided the different SFR $\dot{M}_\star(t, M_{vir}, z_{vir})$ and the average gas metallicity $Z(t, M_{vir}, z_{vir})$ as a function of the galactic age t in the halo mass range $10^{10.0} - 10^{13.4} M_\odot$ and the virialized redshift bins $1.5 \leq z_{vir} \leq 11.0$, the cosmic SFR density can be achieved as :

$$SFR = \int_{M_{vir}} \int_z dz_{vir} dM_{vir} \frac{d^2 N_{ST}}{dz_{vir} dM_{vir}} \dot{M}_\star[t(z), M_{vir}, z_{vir}] \Theta(Z_{cut}) \tag{4.16}$$

where

$$\Theta(Z_{\rm cut}) = \begin{cases} 1, & \text{if} \quad Z[t(z), M_{\rm vir}, z_{\rm vir}] < Z_{\rm cut} \\ 0, & \text{otherwise.} \end{cases} \tag{4.17}$$

and $d^2 N_{ST}/dz_{vir} dM_{vir}$ is the formation rates of objects with mass M_{vir} at redshift z_{vir}. This theoretical result is consistent with both the simulation(e.g., Kobayashi, Springel & White 2006) and the observational measurements from Hopkins (2004) and Hopkins & Beacom (2006) shown in the Fig. 4.6. From the HST/ACS and VLT/ISSAC data, the beginning of the star formation epoch has been determined at redshift 7(Mannucci et al. 2006). However, it is also noted that from the lensing clusters observation the star-forming galaxies at redshift $6 \leq z \leq 10$ has been achieved(Richard et al. 2006), the SFR density is higher than the estimates from UDF by Bouwens et al. (2005).

The present mean metallicity of interstellar medium is close to the solar value(Kulkarni & Fall 2002). Although it is well known that the number would be rapidly increase with redshift, based on the evolution of global SFR density, it is expected that after redshift $3 - 4$, the mean metallicity turns to decrease(Madau, Pozzetti & Dickinson 1998; Songaila 2001; Fynbo et al. 2006). Stiavelli, Fall & Panagia (2004) set the minimum and maximum value of $1.7 \times 10^{-4} Z_\odot$ and $0.01 Z_\odot$ at redshift 6, but these values are corresponding

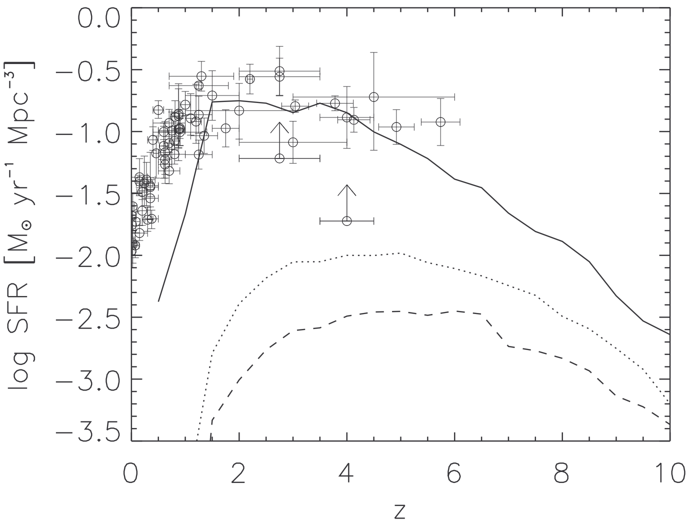

Figure 4.6: Star formation history as the function of redshift. Dashed line is for a metallicity threshold of 0.1 solar, dotted line for 0.3 solar and solid line for no-threshold. The data are collected by Hopkins (2004).

to the situation which is dominated by the primordial metal-free Pop III stars. Since only Pop I and Pop II stars are included in the thesis, we take the threshold metallicity value $Z_{cut} = 0.1Z_{\odot}$ to illustrate the metal effect. Note that the mean metallicity of infalling gas and the metallicty of normal stars in the galaxies could be totally different.

The threshold metallicity Z_{cut} is corresponding to the galactic evolutionary timescale t_{nodust}. Below the level of the threshold value the environment is viewed as dust-free while $Z > Z_{cut}$ means that the galactic evolution passes into the dust and metal phase. The galactic timescale t_{nodust} is dependent on the dark halo mass, redshift and metallicity. More and more evidences reveal that the environment at high redshifts is polluted by the dust of supernova explosion(Maiolino et al. 2004; Marchenko 2006). Therefore, the UV photons could be strongly absorbed and have no possibility to contribute for reionization. However, during the first beginning of galactic timescale about 10^7 years, the environment may not be affected by the dust yet. With the fixed infalling gas metallicity, the galactic timescale shown in the Fig. 4.7 could be a dust-free timescale for the primordial galaxies at redshift around 6. The obtained timescale is roughly equal to the duration of metal-free star formation derived by semianalytic method(Tumlinson et al. 2004) and numerical simulation(Wada & Venkatesan 2003). As mentioned by Venkatesan, Nath & Shull (2006), this corresponds to the timescale for the reincorporation of metals created by the first SNe into cold star-forming gas clumps.

Followed by the model of Granato et al. (2004), this timescale is also dependent on the feedback of SNe and AGNs. Given a more powerful feedback, meaning to strongly quench of star formation, the galactic timescale should be increased. However, the range of this timescale is varied so small, because during the beginning time of 10^7 years, AGNs are still under formation, while massive stars just finish the main sequence phase and are turning to be the SN explosion. Moreover, changing clumping factor does not affect the galactic timescale efficiently, because we assume that star formation at high redshift is violent from the dynamic process, not the gas cooling. In this section, we select the standard parameters used by Granato et al. (2004), in which a coevolution model of galaxies and AGNs has been built, to derive the reasonable galactic timescale thus determine the reionization epoch.

In the mean time, under the different galactic timescales, the details of star formation in different dark halos are shown in the Fig. 4.8 and the SFR functions with different redshifts are shown in the Fig. 4.9.

4.4.2 UV Background at High Redshift

Since the SFR history SFR(z) is given, the luminosity density ρ_{UV} can be transfered as:

$$\rho_{UV}(\nu, z) \approx 1.3 \times 10^{28} \frac{SFR(z)}{M_{\odot} Mpc^{-3} yr^{-1}} erg\ s^{-1} Mpc^{-3}\ Hz^{-1} \tag{4.18}$$

where the constant 1.3×10^{28} is corresponding to the IMF of Romano et al. (2002), while 8.0×10^{27} is the result of Salpeter's IMF as mentioned by Madau, Pozzetti & Dicknson (1998).

The mean special intensity J defined at the observed frequency ν_{obs} of redshift z_{obs} can be derived as:

$$J(\nu_{obs}, z_{obs}) = \frac{1}{4\pi} \int_{z_{obs}}^{\infty} \frac{(1+z_{obs})^3}{(1+z)^3} \rho(\nu, z) e^{-\tau_{eff}(\nu_{obs}, z_{obs}, z)} \frac{dl}{dz} dz \tag{4.19}$$

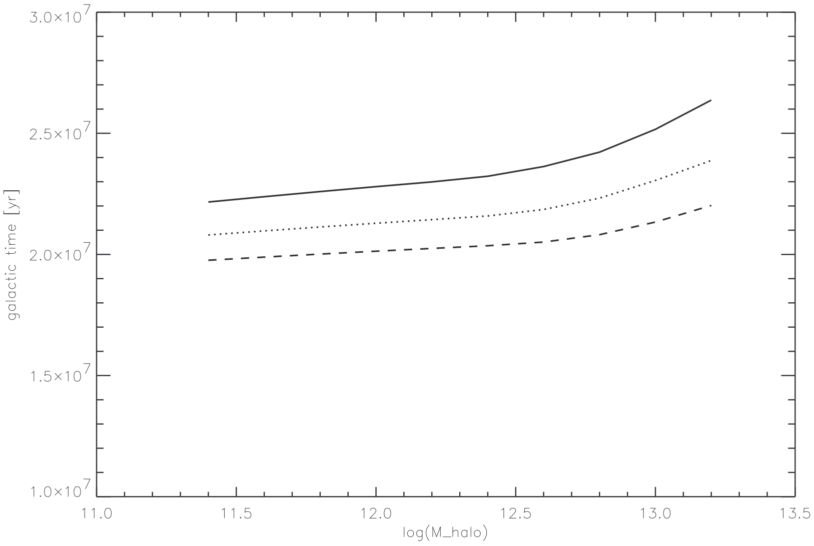

Figure 4.7: Galactic timescale for the fixed star metallicity $Z = 0.1 Z_{\odot}$. Redshift 6, 7 and 8 are symbolized with solid line, dashed line and dotted line respectively.

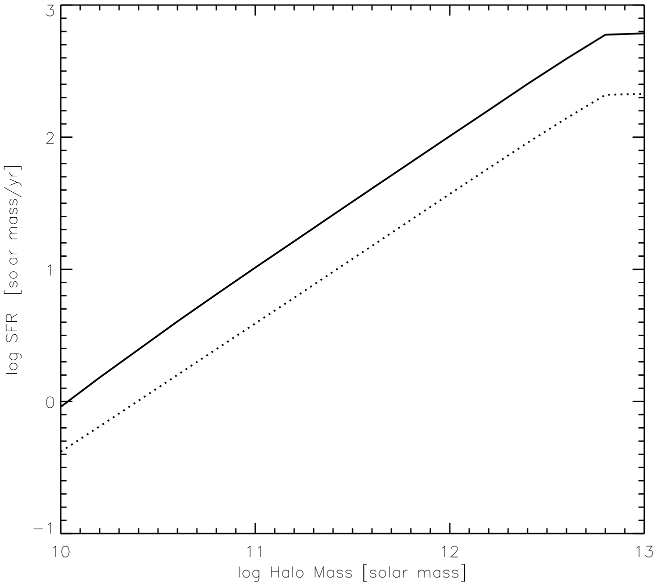

Figure 4.8: Star formation rate as the function of dark halo mass. Solid line is for a threshold of 2×10^7 years and dotted line is for 8×10^6 years.

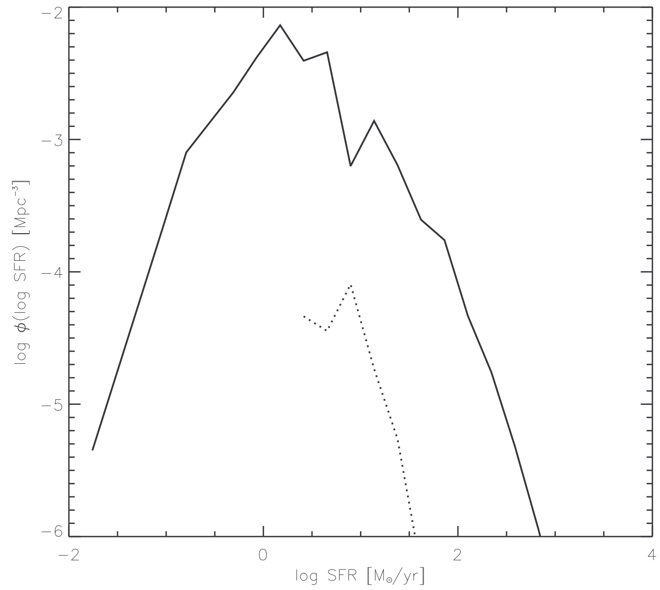

Figure 4.9: Star formation rate function with the threshold of 2×10^7 years, solid line is for the redshift 6.5 and dotted line is for the redshift 10.

where $\nu = \nu_{obs}(1+z)/(1+z_{obs})$ is the relation between the rest-frame and the observed frequency, the line element is written as

$$\frac{dl}{dz} = \frac{c}{H_0(1+z)[(1+z)^3\Omega_m + \Omega_\Lambda]^{1/2}} \tag{4.20}$$

To obtain a complete solution, the values of ρ_{UV} extended to the very high redshift are required. We assume that the ρ_{UV} evolves with redshift as an exponential damping for $z > 10$ as predicted by Kitayama et al. (2001) and Umemura, Nakamoto & Susa (2001).

The $\tau_{eff}(\nu_{obs}, z_{obs}, z)$ is the effective optical depth between z and z_{obs} due to absorption of IGM, depending on the distribution of neutral hydrogen and observational frequency(Madau 1995). As the first approximation, the absorption can be ignored as $\tau_{eff} = 0$(Haiman, Rees & Loeb 1997). In the paper of Loeb & Haiman (1997), the absorption effect is calculated from the collapse of dark halo with a dust ratio. More deliberative solution was given by Bianchi, Cristiani & Kim (2001). Numerical simulation has been performed for the color correction due to this kind of intergalactic attenuation(Meiksin 2006). In this context, we use the function of Madau, Haardt & Rees (1999):

$$\tau_{eff} = \frac{4}{3}(\pi\sigma_0)^{0.5}N_0(\frac{\nu_{obs}}{\nu_L})^{-1.5}(1+z_{obs})^{1.5}[(1+z)^{1.5}-(1+z_{obs})^{1.5}] \quad (4.21)$$

where $\sigma_0 = 6.3\times10^{-18}cm^{-2}$ is the hydrogen photoionization cross section at the Lyman edge $\nu_L = 912\mathring{A}$, $N_0 = 4.0\times10^7$ is the normalization value.

Given the intensity of UV background at redshift z, the photoionization rate can be also obtained by:

$$\Gamma_{HI}(z) = 4\pi\int_{\nu_0}^{\infty}\frac{J(\nu,z)\sigma_{HI}(\nu)}{h\nu}d\nu \quad (4.22)$$

with ν_0 the frequency of the Lyman limit and photoionization cross section of hydrogen $\sigma_{HI}(\nu) = \sigma_0(\nu_0/\nu)^3$.

4.4.3 Results Obtained from Luminosity Function

From the luminosity function of Lyman break galaxies, we get the cosmic star formation history as

$$SFR(t) = \int d\dot{M}_\star\Phi(\dot{M}_\star,t)\dot{M}_\star \quad (4.23)$$

where $\dot{M}_\star$ is the star formation rate and the UV background can be computed by:

$$\rho_{UV}(t) = \int dM_{1350}\Phi(M_{1350},t)\frac{L_{1350}}{\nu_{1350}} \quad (4.24)$$

Therefore, the cosmic star formation and UV background is shown in the Fig. 4.10.

4.5 Reionization at Redshift $6-8$

4.5.1 General Formula

The complete reionization model includes two components: one is for the sources which emit UV photons at any given redshift, the other is the propagation of ionization regions in IGM.

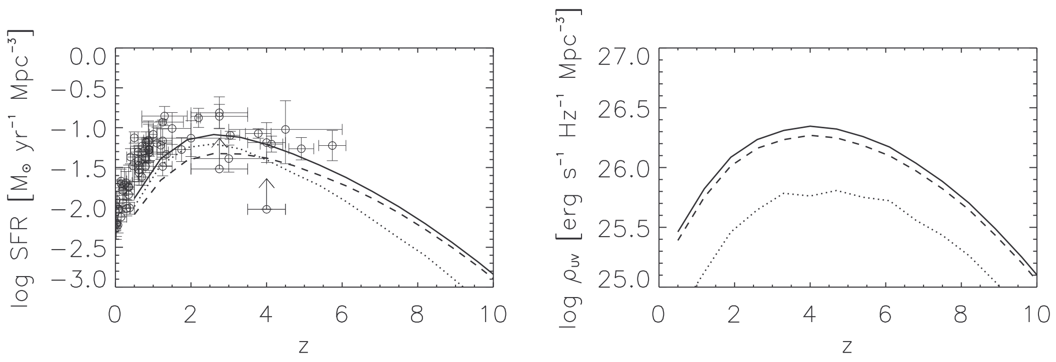

Figure 4.10: Cosmic star formation history(left panel) and the UV background contributed by the stellar properties(right panel). The overall result (solid) is split in the contribution from protogalaxies brighter(dash) or dimmer(dot) than $M_{1350} = -17.5$. The data are coming from Hopkins (2004).

The radiation intensity in thermal equilibrium of a normal star presents the black-body spectrum:

$$B_\nu = \frac{dE}{d\nu dt dA d\Omega} = \frac{2h\nu^3}{c^2}\frac{1}{e^{h\nu/kT}-1} \tag{4.25}$$

For a star remaining on the main sequence, the scaling relation for mass-luminosity and luminosity-temperature are given by(Padmanabhan 2001):

$$\frac{L}{L_\odot} = (\frac{M}{M_\odot})^\alpha \tag{4.26}$$

and

$$\frac{T_{eff}}{T_\odot} = (\frac{L}{L_\odot})^\beta \tag{4.27}$$

Therefore, the rate of UV photons per unit solar mass for reionization of neutral hydrogen is(Bromm, Kudritzki & Loeb 2001):

$$\frac{d^2N_{ion}}{dtdM} = \frac{1}{M}\int_{\nu_1}^{\nu_2}\frac{<L_\nu>}{h\nu}d\nu \tag{4.28}$$

where $<L_\nu>= \int dM L_\nu(M)\Phi_{IMF}(M)$ is the specific luminosity averaged over IMF, calculated from B_ν integrated by solid angle and radiation area.

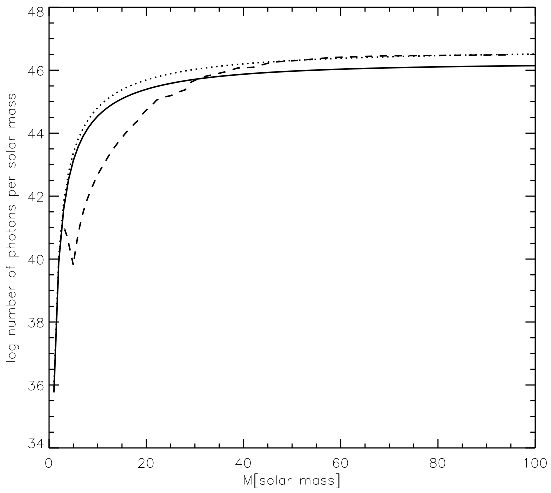

Figure 4.11: UV photons per solar mass emitted by different masses of stars. Solid line: IMF of Salpeter; Dotted line: IMF proposed in the model of Romano et al. (2002); Dashed line: the model taken from Bressan(1993), with metallicity $Z = Z_{\odot}$.

The stellar radius can be obtained by the relation of $L = 4\pi R^2 \sigma T_{eff}^4$. The respective threshold frequency for ionizing neutral hydrogen is $3.29 \times 10^{15} Hz < \nu < 5.94 \times 10^{15} Hz$. Since the UV photons are contributed mainly from the massive stars, in this context, we choose the set of stellar parameters $(\alpha, \beta) = (3.8, 0.17)$ which can be fitted well with the high luminosity and high temperature part on the Hertzsprung-Russell diagram. The results are agreement with the numerical model under a spectral library of Bressan (1993).

The difference affected by two kinds of IMF are compared in the Fig. 4.11. The typical slope 1.35 is taken from Salpeter(1955), while another double-power law from the model of Romano et al. (2002) has the form of $\Phi_{IMF} \propto M^{-1.25}$ for $1M_{\odot} < M \leq 100M_{\odot}$ and $\Phi_{IMF} \propto M^{-0.4}$ for $M \leq 1M_{\odot}$. The upper limit of the stellar mass has the cut-off at 100 $M_{\odot}$, indicating that it is not necessary to choose those supermassive stars, i.e., Pop III, in this scenario.

The photon rate emitted from the proto-galaxies is given by:

$$\frac{dN_{ion}}{dt} = \frac{d^2N_{ion}}{dtdM}\int_{t_{vir}}^{min[t(z),t_{nodust}]} dt' \ \dot{M}_\star[t', M_{vir}, z_{vir}] \tag{4.29}$$

where $t_{nodust}(M_{vir}, z_{vir}|Z_{cut})$ is the timescale within which the galaxy is dust-free, defined here as $Z[t_{nodust}, M_{vir}, z_{vir}] = Z_{cut}$.

The total ionization rate at redshift z is obtained on summing up all the contribution from galactic halos of given mass and virialization redshift, to read

$$\dot{\mathcal{N}}_{ion} = \int_z dz_{vir}dM_{vir} \ \ \frac{d^2N_{ST}}{dz_{vir}dM_{vir}}\frac{dN_{ion}}{dt} \tag{4.30}$$

Of the propagation for the ionization fronts in the IGM, the formula for the evolution of filling factor Q_{HII} is(Shapiro & Giroux 1987; Madau, Haardt & Rees 1999):

$$\frac{dQ_{HII}}{dt} = \frac{\dot{\mathcal{N}}_{ion}}{n_H} - \frac{Q_{HII}}{t_{rec}} \tag{4.31}$$

where t_{rec} is the recombination time as(Madau, Haardt & Rees 1999):

$$t_{rec} = 0.3Gyr(\frac{\Omega_b h^2}{0.02})^{-1}(\frac{1+z}{4})^{-3}(\frac{C}{30})^{-1} \tag{4.32}$$

and C is the clumping factor. The general solution of filling factor is the following:

$$Q_{HII}(t) = exp(-\int_0^t \frac{dt'}{t_{rec}})\int_0^t \frac{\dot{\mathcal{N}}_{ion}}{n_H} exp(\int_0^{t'} \frac{dt''}{t_{rec}})dt' \tag{4.33}$$

All kinds of physical cases for the filling factor solution are discussed in detail by Meiksin (2005). If the case is at high redshift and for the IGM with clumping factor $C >> 1$, which are also the conditions shown by Madau, Haardt & Rees (1999), we have the prime approximation as:

$$Q_{HII} = f_{esc}\frac{\dot{\mathcal{N}}_{ion}}{n_H}t_{rec} \tag{4.34}$$

where n_H is the number density of hydrogen in the local universe. Obviously, $Q_{HII} = 1.0$ is corresponding to the reionization epoch. The optical depth to electron scattering can be computed as:

$$\tau_e(z) = \int_0^z \left| dz' \frac{dt}{dz'} \right| c\sigma_T n_e(z') \tag{4.35}$$

where $n_e = Q_{HII} n_B (1+z)^3$ is the electron density in terms of the baryon number density n_B and $\sigma_{\rm T}$ is the Thomson cross section.

4.5.2 Results

The description in the Section 4.3 and 4.4 is very useful for the determination of the reionization. Obviously, the galaxy luminosity function at high redshift may provide direct observational evidence for the spheroidal protogalaxies which are proposed to reionize the Universe.

In general, the UV photons for reionization are just a part of the total photons emitted from the proto-galaxies. The escape fraction which means the ratio between ionizing photons and the total UV photons of galaxies is a parameter of $0 \leq f_{esc} \leq 1$. To find out the proper value of f_{esc} is a complex process and a wide range of it has been shown in the literatures. From the UV observation of local starburst galaxies $f_{esc} = 0.05$(Heckman et al. 2001). However, at high redshift, the number could be higher(Haiman & Loeb 1997). For the observed sample of LBGs the escape fraction must be close to 100 percent(Haehnelt et al. 2001). $f_{esc} = 0.2 - 0.5$ are set in the simulation of Iliev et al. (2006). It is found that the escape fraction could increase by an order of magnitude, from a value less than 0.01 at $z \leq 1$ to about 0.1 at $z \leq 4$(Inoue, Iwata & Deharveng 2006). Recently, Alvarez, Bromm & Shapiro (2006) reveal that escape fraction is even associated with the star mass and IMF. For more accurate calculation, Benson et al. (2001) split the effect into contributions from dust and gas. Here, we compute escape fraction from the formula:

$$L_{912}^{obs} = L_{912}^{int} f_{HI} e^{-\tau_{912}} e^{-\tau_{IGM}} \tag{4.36}$$

where the L_{912}^{int} is the intrinsic luminosity at $912\mathring{A}$, f_{HI} is the fraction of ionizing photons surviving HI absorption. So the product $f_{HI}e^{-\tau_{912}} = f_{esc}$. following the results of Inoue, Iwata & Deharveng (2006), we write:

$$\frac{L_{912}^{obs} e^{\tau}_{IGM}}{L_{1350}^{obs}} = \frac{L_{912}^{int} f_{esc}}{L_{1350}^{int}} e^{-\tau_{1350}} \tag{4.37}$$

and we get

$$F_{esc} = \frac{R_{esc}}{R_{int}} e^{-\tau_{1350}} \tag{4.38}$$

where $R_{int} = L_{912}^{int}/L_{1350}^{int} = 0.3$ which depends only on the IMF and metal content. R_{esc} can be directly obtained by observation(Shapley et al. 2006).

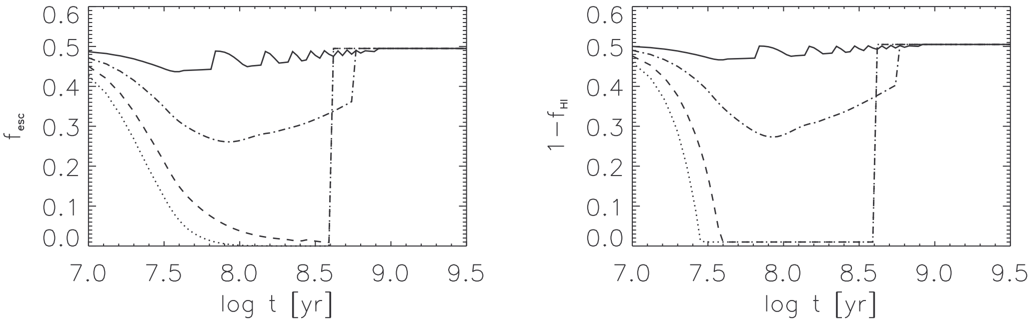

Figure 4.12: Escape fraction of ionizing photons at $912\mathring{A}$ as the function of time for different halo masses $10^{10}M_{\odot}$(solid line), $10^{11}M_{\odot}$(dot-dash line), $10^{12}M_{\odot}$(dash line) and $10^{13}M_{\odot}$(dot line).

The value $R_{ecs} = 0.22$ is taken from Steidel et al. (2001). Here we take $R_{ecs} = 0.15$ as a reference value. Thus the escape fraction can be obtained as Fig. 4.12.

The total reionization photons could be calculated by the two parts. We integral the luminosity function and get the number density of the galaxies while form the UV luminosity we know how many ionizing photons can be obtained. In this procedure, we transfer the luminosity at $1350\mathring{A}$ to $912\mathring{A}$ as $L_{912} = R_{esc}L_{1350}^{obs} = R_{esc}L_{1350}^{int}e^{-\tau_{1350}}$. From the luminosity function fitting of Lyman break galaxies, we have:

$$\dot{\mathcal{N}}_{ion} = \int d\dot{N}_{912}\Phi(\dot{N}_{912}, t)\dot{N}_{912} \tag{4.39}$$

where

$$\dot{N}_{912} = \frac{L_{912}}{h\nu_{912}} = 3.6 \times 10^{53} f_{esc}(\frac{\dot{M}_*}{M \odot yr^{-1}})s^{-1} \tag{4.40}$$

Therefore, in Fig. 4.13 and 4.14 we illustrate the filling factor evolved with redshift. The results are consistent with the estimation assuming the galactic timescale of 2×10^7 yr and the infalling gas metallicity $Z = 0.1Z_{\odot}$. Fig. 4.15 is presented for the upper limit and lower limit of filling factor under the different parameters of clumping factor C and the f_{esc}. The related electron optical depth at the reionization epoch is determined as the value about 0.06.

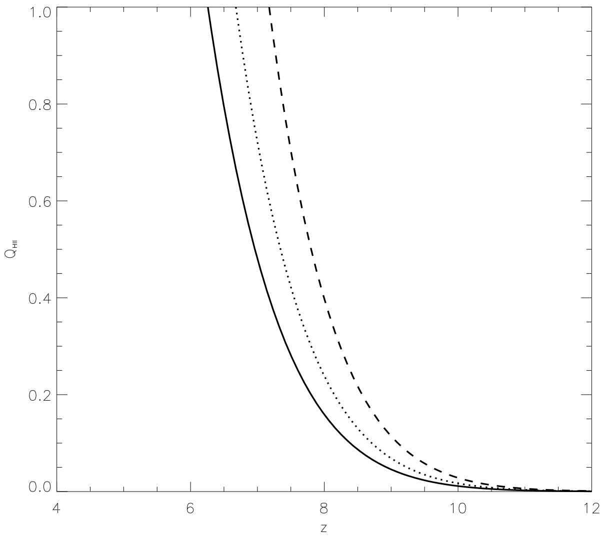

Figure 4.13: Filling Factor vs. redshift. The evolution for $f_{esc} = 0.2$(solid), $f_{esc} = 0.3$(dotted) and $f_{esc} = 0.5$(dashed) are shown respectively with $C = 7$ and the IMF of Romano et al. (2002).

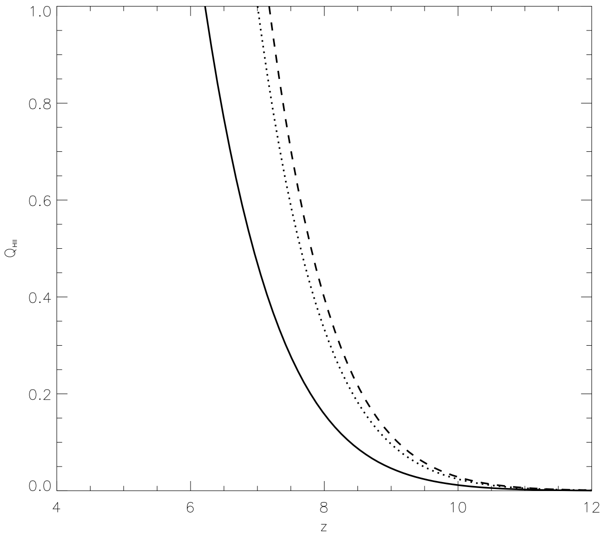

Figure 4.14: Filling Factor vs. redshift. The evolution for clumping factor $C =$ 7(solid), $C = 10$(dotted) and $C = 30$(dashed) are shown respectively with $f_{esc} =$ 0.5 and the IMF of Romano et al. (2002).

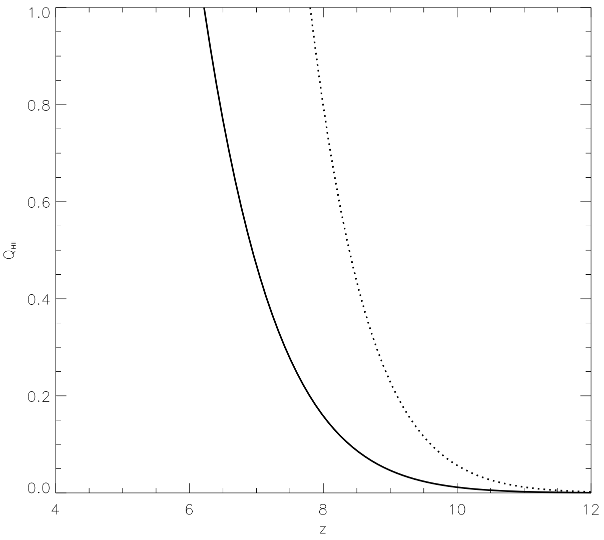

Figure 4.15: Upper and lower limit cases of filling Factor vs. redshift. The evolution for clumping factor $C = 7, f_{esc} = 1.0$(dotted) and $C = 30, f_{esc} = 0.5$(solid) are shown respectively with the IMF of Romano et al. (2002).

The Lyman alpha emitters which are possibly prior to the reionization redshift have been detected(e.g., Hu et al. 2002; Kashikawa et al. 2006). The source can create the HII region(30 comoving Mpc) around itself and allow most of the intrinsic Lyα line to be transmitted without significant scattering(Haiman 2002). Within the region from the boundary of HII regions to the reionization epoch, the emission line may suffer absorption as presented simply by the parameter f_{IGM}. Thus, the process can be described by $F_{obs} = f_{Ly\alpha}F_{em} = e^{-\tau_{dust}}(1 - f_{esc})f_{IGM}F_{em}$(Barton et al. 2004). In this context, we use the optical depth of the dust as mentioned before. The normal transformation from the star formation rate to the Lyman alpha luminosity is $L(Ly\alpha) \approx 3.0 \times 10^{42}(SFR/M_{\odot}yr^{-1})ergs\ s^{-1}$(Kashikawa et al. 2006). Here, assuming 2/3 of the ionizing photons absorbed by neutral hydrogen in the galaxy are converted into Lyman alpha photons, we have:

$$L_{1216}^{int} = \frac{2}{3}L_{912}^{int}(1 - f_{HI}) = 2.2 \times 10^{42}(1 - f_{HI})(\frac{\dot{M}_*}{M \odot yr^{-1}})ergs^{-1} \qquad (4.41)$$

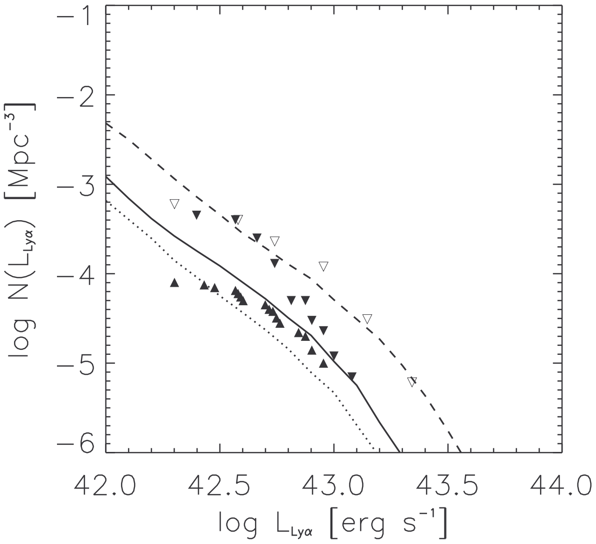

Figure 4.16: Model prediction of luminosity function of Lyα emitters at redshift 6.5(Solid), 5.7(dash) and 8.2(dot). Data are collected form Kashikawa et al. (2006) as upper and lower limits denoted as filled triangles. The empty triangles are the symbol of data at z=5.7 from Shimasaku et al. (2006).

and

$$L_{1216}^{obs} = L_{1216}^{int} e^{-\tau_{1216}} f_{IGM} \tag{4.42}$$

The $f_{IGM} = 0.12$ can be used to fit the data as the same number selected by Nagamine et al. (2006a) and $f_{esc} = 0.2$. For the detailed calculation of the Lyα line with the transmission through IGM, the cross section as the function of observed wavelength has been given by Peebles (1993). The line profile and the optical depth has been shown in the work of Santos (2003) and Dijkstra, Haiman & Spaans (2006). Here, we note that $(1 - f_{HI})e^{-\tau_{1216}} f_{IGM} \leq 0.1$. Thus, the luminosity function of Lyα emitters can be drawn in the Fig. 4.1.

Furthermore, since recently the massive Lyman-break galaxies at redshift $4 < z < 6$ have been discovered from the deep surveys(Dunlop, Cirasuolo & McLure 2006; McLure et al. 2006), it is also interesting to understand the halo masses(corresponding to the stellar masses) which contribute to the reionization process. In our model, SFR is given by $\dot{M}_\star \propto M_{vir}^{3/2}$(Granato et al. 2004). We use the form of Sheth & Tormen (2002) to calculate the dark halo formation rates and estimate the total ionized photons as:

$$\frac{dn_{ion}}{dt} \propto \dot{M}_\star \frac{d^2 n_{vir}}{dM_{vir}dz} \propto [M_{vir}^{-1/3} + \frac{M_{vir}^{-3/5}}{(1+z)^{0.6}}](1+z)^{1.5} exp[-A(1+z)^2 M_{vir}^{1/3}] \tag{4.43}$$

where $d^2n_{vir}/dM_{vir}dz$ is the formation rate of halo mass function and parameter A is certain constant. We define function $F(M_{vir}, z) \equiv [M_{vir}^{-1/3} + M_{vir}^{-3/5}(1+z)^{-0.6}](1+z)^{1.5}exp[-A(1+z)^2 M_{vir}^{1/3}]$ and do integral as $I(M_{vir}, z) = \int_{M_{min}}^{M_{vir}} F(M_{vir}, z)dM_{vir}$, where $M_{min} = 10^{10.0}M_\odot$ is the lower limit, the total UV photons in different halo can be realized. Thus, in Fig. 4.17 we plot the integrated contribution to the reionization flux from masses above a given threshold. The main contribution arises from galaxies residing in halos with masses $M_{vir} \leq 10^{12}M_\odot$ and the halo masses larger than $10^{12}M_\odot$ do not take effect for reionization. This is due to the reason that in general the smaller halos are numerous while massive halos are very rare. Therefore, only those small galaxies hosted by the small halos do contribution to the reionization. The discovery of massive galaxies at high redshift reveals the downsizing feature as mentioned in the Section 3.2, however, these massive galaxies hosted by the massive halos can be negligible for the reionization. This theoretical result is supported by the recent discovery of stellar masses from Spitzer observation(Labbe et al. 2006).

The final issue is the following: what is the evolution of the protogalaxies considered here after the time $t_{\rm nodust}$? In our view these objects will be polluted by the dust produced by the SN explosions, then evolve into highly dust-enshrouded objects radiating mainly at IR and submm wavelengths. Therefore, our model prediction for the Submillimetre Common User Bolometer Array(SCUBA) counts at 850μm are plotted in Fig. 4.18, the result is in excellent agreement with the observational data.

As the summary, the different galaxy properties in the different dark halos at different redshift are compared in the Fig. 4.19. Since reionization is occurred at high redshift during the beginning stage of the galaxy formation, the value of star formation before the $10^7 - 10^8$ years is higher at high redshift. Because the UV photons are mainly contributed from the protogalaxies in the small halos, the supernova feedback will essentially affect on

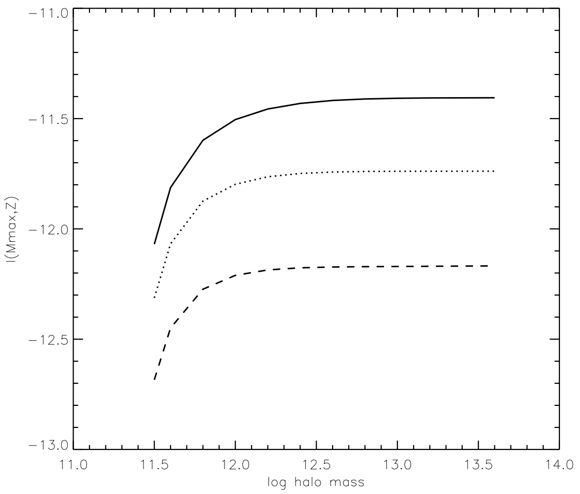

Figure 4.17: The contribution to the UV flux from masses above a given value, indicating the ionized photons are released mainly from those small objects. The Solid line refers to redshift 6, dotted line to redshift 8 and dashed line to redshift 10.

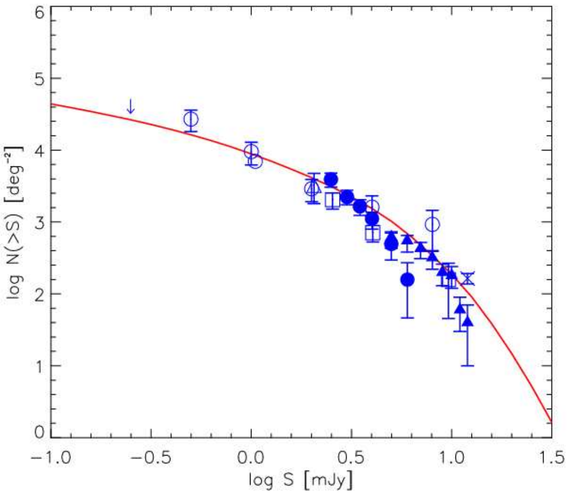

Figure 4.18: Predicted 850μm number counts(Solid line) with the data of Blain et al. (1999; open circles), Hughes et al.(1998; asterisk and open triangles), Barger, Cowie & Sanders(1999; open squares), Eales et al. (2000; filled circles), Chapman et al(2002; filled triangles) and Borys et al. (2002; filled squares).

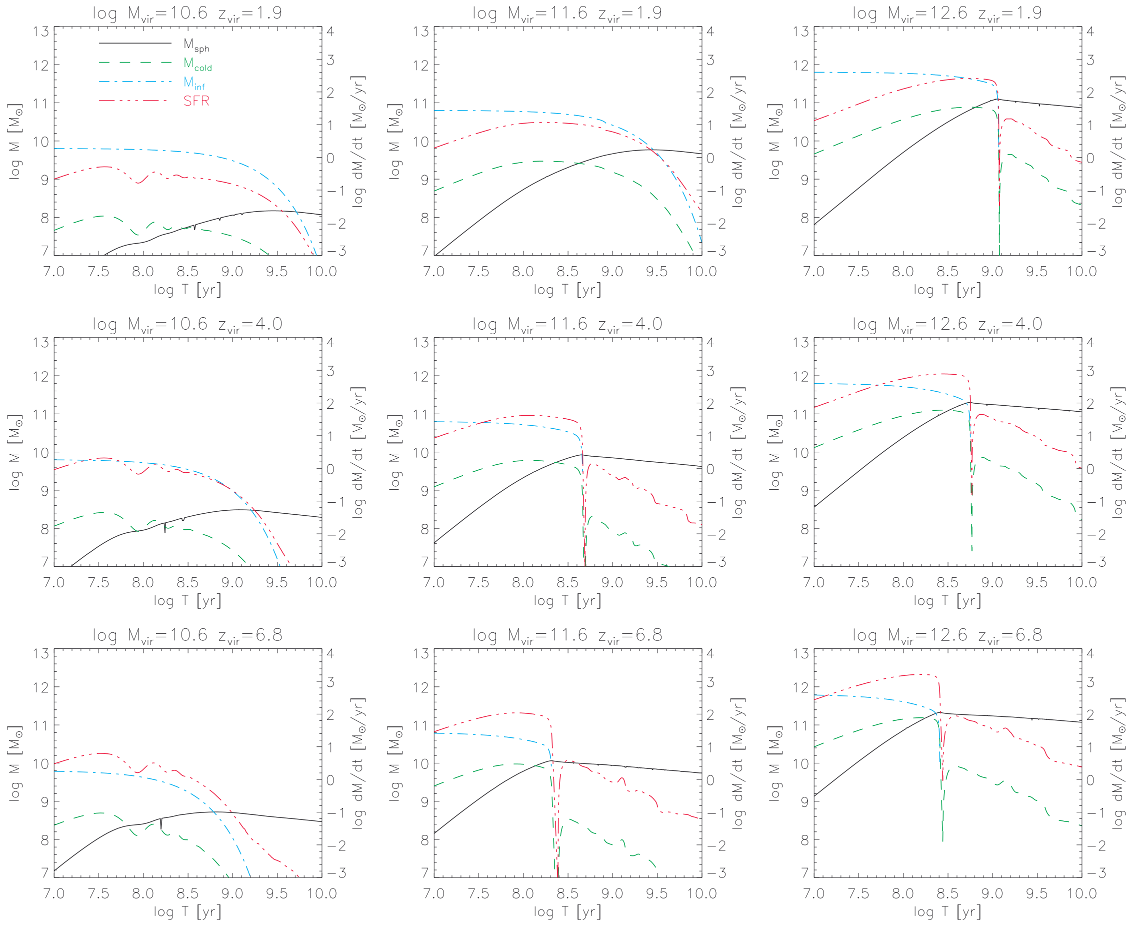

Figure 4.19: The evolution of star formation rate, mass of spheroids, mass of infalling gas and mass of cold gas in the different halo mass at different redshifts.

the star formation so that the star formation in the smaller halos is strongly suppressed.

4.6 Conclusion and Discussion

During the work, we have shown that the UV background at high redshift can be mostly provided by the normal stars residing in proto-galactic spheroids. Based on this scenario, the reionization epoch has been estimated around redshift $z \sim 6-8$, which is consistent with the measurement from QSO spectrum(Fan et al. 2002). In the mean time, the results can fit the luminosity functions of high redshift galaxies selected by Bouwens et al. (2006) and Lyman alpha emitters(Kashikawa et al. 2006) well. The fitting can be the extreme constraint for the reionization issues.

However, the situations of HII regions around the high redshift QSOs are still under debate. From the QSO spectra, the study favors a ionized universe with $x_{HI} < 0.06$ at redshift 6.1(Maselli et al. 2006). Fan et al. (2006) found that the ionization state of IGM changes very fast toward the high redshift. But, for a sample of optical depth in the Lyman alpha forest with wide redshift range, there has no evidence to support the opinion that reionization occurs suddenly at redshift 6(Becker, Rauch & Sargent 2006).

4.6.1 Beginning Stage of Primordial Galaxies

Although some authors argue that those observed galaxies at $z \sim 6$ are not sufficient to reionize the IGM(Bunker et al. 2004), our calculations present the positive opinion. For the sample of LBGs, Haehnelt et al. (2001) declared that the escape fraction must be close to 100 percent, meaning that this sample could be dust-free. Somerville & Livio (2003) calculated the global SFR under the hierarchical collapse and found that Pop II stars alone may be able to reionize the universe if the reionization occurs at late epoch($z_{ion} < 15$). Recently, Nagamine et al. (2006a) have also shown their results of SFR and LBGs, the implication is that the universe could be reionized by Pop II stars in the ordinary galaxies.

Our conclusion, with other similar results mentioned above, are strongly supported by the UDF and GOODS observation at redshift 6, especially about the measurement of stellar mass density(Stark et al. 2006) and a large contribution of faint galaxies(Yan & Windhorst 2004a,b; Bouwens et al. 2006) as mentioned in the Section 4.2. Furthermore, as the indirect evidence, some dwarf elliptical galaxies survived today in the Local Group are thought to form stars during their early evolution phase at high redshift universe, then, pass by a long passive evolution and finally be the fossils from the epoch of reionization (Ricotti & Gnedin 2005; Gnedin & Kravtsov 2006; Tumlinson 2006; but see also Fenner et al. 2006). Recently, Wyithe & Loeb

(2006) have pointed out that the limit mass about $10^{11}M_{\odot}$ is two orders of magnitude larger than the reionizing galaxies. As shown in the Fig. 4.17, our results illustrate that all the galaxies contributed to the reionization are harbored in the halos below the mass of $10^{12}M_{\odot}$.

Therefore, we realize: during the first period of about 10^7 years, the primordial galaxies emit UV photons to ionize the universe on the first stage and can be observed by GOODS and UDF in optical band; then, these objects evolve into the highly dust-enshrouded sources, being active as SCUBA galaxies at submm wavelength; Some small objects as the fossils of reionization survive today, showing as red dwarfs.

4.6.2 Dust and Metallicity at High Redshift

In the local universe, for instance, the dust density in the Galaxy is $\rho_d = 1.8\times 10^{-23}kgm^{-3}$ calculated from the interstellar extinction. The dust production is mainly from the M giants and other Carbon-rich stars, which give the dust injection as $\dot{\rho_d} = 2.0\times10^{-32}kgm^{-3}yr^{-1}$(Whittet 1992). Thus, the estimation of the dust timescale is about $t_{dust} = \rho_d/\dot{\rho_d} = 9.0\times10^8 yr$, which is larger than the galactic timescale shown in the Fig. 4.6. The evolution of the abundances in the gas and dust phases of interstellar medium of the Galaxy has been studied(Dwek 1998). The mass-loss predictions for early-type stars as a function of metallicity has also been calculated(Vink, de Koter & Lamers 2001). However, although these stars could be born in the early universe, they occupy the main sequence as long as about 10^9 years so that they may not be the origin of dust production at high redshift.

It is expected that the universe dominated by the first stars and galaxies could be metal-free. Since we assume that the reionization process was finished at $z\sim 6$ and Pop III stars do not affect the situation at this epoch, it need not to constrain the mean metallicity as a low value of about $10^{-4}Z_{\odot}$. Moreover, the metals would be enriched in the IGM by the first generation stars(Madau, Ferrara & Rees 2001) so that the clean environment could be still polluted. Marchenko (2006) provided a brief review of dust production at high redshift, SNe and other massive stars are thought to be the major dust factories. The observational emission line ratios in the star-forming galaxies as the diagnostics of gas metallicity are investigated comprehensively by Nagao, Maiolino & Marconi (2006). Cosmic history of metal densities is firstly attempted by chemical evolution models(Calura & Matteucci 2006). For simplicity, it is plausible to fix the star metallicity which is corresponding to certain galactic timescale. Particularly, the metallicity of $0.3Z_{\odot}$ is the value of intra-cluster medium determined by X-ray observation(Fukazawa et al. 1998; Voit 2004) while the metallicity of $0.1Z_{\odot}$ is the level of pre-enrichment of G dwarf stars around the solar neighborhood and in near galaxies(Ostriker & Thuan 1975; Thomas, Greggio & Bender 1999). Nagamine, Springel & Hernquist (2004) have obtained the mean metallicity for damped Lyman-alpha absorbers through simulations, the value of $1/3Z_{\odot}$ at redshift 3 is much higher the observed one of $1/30Z_{\odot}$. However, as pointed out by Prochaska et al. (2003), the missing metal problem, the observational number is 10 times lower than the one expected from star formation history, has shown that the interplay between star formation and chemical abundance could not be understood as the normal way.

In this context, we draw our estimation as below. Suppose star formation rate $\psi(t) = 32(1+z)^{2/3}(M_{gas}/10^{11}M_{\odot})$(Granato et al. 2004) is also valid for the type of young star-forming galaxies at redshift 6, the total mass of metallicity could be $M_{metal} = \psi(t) \times t_{nodust} \times f \times (M_{dust}/M_{star}) \times f_{dep}$. t_{nodust} is the galactic timescale shown in the Fig. 4.6. The parameter $f = 0.29$ is the ratio of massive stars($M > 2M_{\odot}$) to all stars, calculated from Salpeter's IMF. The ratio M_{dust}/M_{star} means the dust mass produced by the SNe to the progenitor star mass. The mass value of output dust per SN, varies from a small number $10^{-3}M_{\odot}$(Dwek 2004; Pozzo et al. 2004) within the ejecta of core-collapse supernovae detected by the infrared band, to the large value $0.08-0.3M_{\odot}$(Todini & Ferrara, 2001) which is in agreement with the submillimeter observation(Morgan et al. 2003). Here, following the result of Todini & Ferrara (2001) and Schneider, Ferrara & Salvaterra (2004), we take the value $M_{dust}/M_{star} = 0.03$ as the average number although the real one would be dependent on the initial metallicity and SN progenitor mass. f_{dep} means the quantity of metals converted from the dust, it is also studied in detail by Schneider, Ferrara & Salvaterra (2004), here, we assume that all dust can be changed into metals thus $f_{dep} = 1.0$. Therefore, the metallicity can be obtained as $Z = M_{mental}/M_{gas}$. At redshift 6, the metallicity $Z = 0.1Z_{odot}$ is corresponding the galactic timescale 4.0×10^7 yr. Although this estimation is roughly consistent with our calculation in the section 4.3 and 4.4, given the galactic timescale, the obtained metallicity is still a little smaller. This may be due to the following reason: we argue that all massive stars turn into SNe and release heavy abundances, however, as point out by Marchenko (2006), other types of massive stars, such as red giants and carbon-rich Wolf-Rayet stars which may also produce the dust(Eldridge & Vink 2006; Kroger, Hensler & Freyer 2006), are ignored, although it is said that Wolf-Rayet populations are more common within the metal-rich environment(Crowther 2006).

In addition, two kinds of objects should be noticed for the complete discussion: (1) As mentioned in the Section 4.2, the GRBs could be one powerful tool for the study of star formation and IGM at high redshift universe. The GRB 040904 has been detected at redshift 6.3, with a series metal absorption lines, implying the environment may be self-polluted by pre-burst winds(Kawai et al. 2006). (2) The observation of local dwarf irregular galaxies may give the hints for deeply understanding of the young objects reionizing IGM at high redshift. In general, the dwarf galaxies have low mentallicities typically below half-solar(Mateo 1998). The observation of chemical abundance $[\alpha/Fe]$ ratios in four Local Group dwarf irregular galaxies(NGC 6822, WLM, Sextans A and GR 8) all appear to have solar ratios(Venn et al. 2003). As a particular example, NGC 1705, a nearby blue compact dwarf, has shown one third solar metallicity(Tosi et al. 2001; Lee & Skillman 2004). Note that these blue dwarfs could be the primordial galaxies in the local universe, not the red ones as the fossils of reionization at high redshift mentioned in the section 4.5.

4.6.3 Different IMF

The different IMF forms give the different results of reionization. As mentioned in the Section 4.2, The IMF proposed by Larson (1998) can be constrained by the UV background and reionization observation(Schneider et al. 2006). Other forms of IMF, such as the discussions by Kroupa (2001) and

Baldry & Glazebrook (2003), varied with the power-law index by different stellar mass range, have been applied in the local universe. For our work, we have compared the effects with the IMF of Salpeter and of Romano et al. (2002). It is shown that the normal stellar population with the universal IMF of Salpeter could be enough to do with the observations at redshift $z \sim 6-8$, however, the reionization epochs are varied with the different choices of the IMF.

4.7 Other Issues Associated with Reionization

4.7.1 Near Infrared Background

The observation of near infrared background may open another window to study the reionization. It has been shown that the near IR background has an intensity excess with respect to the light from normal galaxies(e.g., Hauser & Dwek 2001; Totani et al. 2001). The UV photons emitted from redshift $6-10$ will be redshifted to the near IR band thus be detected from background observation. Therefore, The IR excess could be produced by the metal-free stars at high redshifts(Santos, Bromm & Kamionkowski 2002; Salvaterra & Ferrara 2003). However, this explanation has overestimated the number of J-dropouts and Lyman alpha emitters(Salvaterra & Ferrara 2006). Recently, it has been found that Pop II galaxies dominate the near IR intensity while Pop III stars contribute at most 40% of total intensity(Salvaterra et al. 2006). The similar results have been obtained that stars with metals as $1/50Z_{\odot}$ can also produce the IR background as metal-free stars(Fernandez & komatsu 2006).

4.7.2 Early Reionization by Pop III Stars

The objects which collapse at first beginning are predicted to have masses corresponding to the virial temperature 10^4 K. For the primordial gas under this condition, the main coolant is molecular hydrogen via the process $H + e^- \rightarrow H^- + \gamma$, $H^- + H \rightarrow H_2 + e^-$. Tegmark et al. (1997) calculated the evolution of H_2 abundance for different halo mass and found that the minimum baryonic mass is from $10^6 M_\odot$ at redshift 15 to $5\times10^3 M_\odot$ at redshift 100 if the H_2 cooling is efficient. From the numerical simulation of Abel et al. (2000) and Fuller & Couchman (2000), this critical mass value could be even smaller for a factor of 10. The recent simulation about the formation of primordial stars in ΛCDM universe is given by Yoshida et al. (2006).

The Population III stars, with mass of several hundred to one thousand solar mass and nearly zero metallicity, have been proposed to appear in the early universe, emitting more effectively UV photons than the normal stars(e.g., Haiman & Loeb 1997; Tumlinson & Shull 2000; Bromm, Kudritzki & Loeb 2001; Schaerer 2002; Cen 2003a,b; Tumlinson, Shull & Venkatesan 2003; Ciardi, Ferrara & White 2003; Reed et al. 2005). This kind of massive stars could be collapse into intermediate mass black holes in the dark minihalos(Madau & Rees 2001; Ricotti & Ostriker 2004a,b; Zhao & Silk 2005; Ciardi et al. 2006) and shine as miniquasars(Cooray & Yoshida 2004; Madau et al. 2004; Madau & Silk 2005; Salvaterra, Haardt & Ferrara 2006).

The Pop III stars may play a vital role for an earlier reionization epoch. The transition from the early epoch($z = 17-20$) to the later one($z = 6-7$) was under debate(Schaerer 2003; Schneider et al. 2006). Cen (2003b) proposed the twice reionization in the universe to explain both the observation of QSO spectrum and 1st year WMAP data. Ciardi et al. (2006) put forward a model in which the cosmic reionization may start at very high redshift and then go through a long phase lasting up to $z \sim 6$. If the gas remained largely in the metal-free state at higher redshift, the era of Pop III could be prolonged and extended to the redshift 6(Wyithe & Cen 2006).

Constrained by the new three-year WMAP data, for instance, one updating model is proposed that reionization starts around redshift 15 and completes by $z = 10$, Pop III stars, forming with efficiencies $> 2\%$, still favour this scenario(Choudhury & Ferrara 2006). However, in order to avoid overproducing the optical depth, as an example, at redshift about 15, the efficiency to produce UV photons in minihalos should be an order of magnitude lower than expected(Haiman & Bryan 2006). It gives the hint that the feedback processes may show an important way(e.g., Haiman & Holder 2003) to suppress the star formation and production of UV photons. Some feedback mechanisms are: the metals are enriched in the IGM by the first generation stars(Madau, Ferrara & Rees 2001; Karlsson 2006),thus the subsequent star formation will be affected(Wyithe & Loeb 2003b); H_2 is important for gas cooling, but UV photons will destroy the H_2 molecules directly(Haiman, Rees & Loeb 1997; Ciardi, Andrea & Abel 2000); the clustered sources at high redshift boost the impact of feedback progress(Kramer, Haiman & Oh 2006). Beside the feedback, another way for model correction is to retreat the dark halo distribution from the new cosmological parameters by WMAP data. Note that the value of σ_8 has been changed from 0.9 to 0.74(Spergel et al. 2006). It has been found that the delay of reionization is well-matched by a comparable delay in the formation of the halos responsible for reionization(Alvarez et al. 2006).

All these proposals put their predictions to be compared with the deeper surveys and more accurate observations such as James Webb Space Telescope(JWST) and Plank satellite in the future.

4.7.3 HI 21cm Observation

The observation of 21cm hyperfine line of neutral hydrogen is the powerful tool to study the early phases of cosmic structure and the high redshift universe(see the review of Furlanetto, Oh & Briggs 2006). At redshift larger than 10, the universe can be directly observed by 21cm transition of neutral hydrogen. The observed brightness temperature due to HI 21cm line is given as(Fan, Carilli & Keating 2006; Furlanetto, Sokasian & Hernquist 2004):

$$T_B = \frac{T_s - T_{CMB}}{1+z}\tau = 7(1+\delta)x_{HI}(1 - \frac{T_{CMB}}{T_s})(1+z)^{1/2} mK \qquad (4.44)$$

where T_s is spin temperature, T_{CMB} is CMB temperature, δ is the cosmic overdensity, x_{HI} is the fraction of neutral hydrogen, the optical depth

$$\tau = \frac{3c^3 hAn_{HI}}{16k_B\nu_{21}^2 T_s H(z)} \sim 0.0074\frac{x_{HI}}{T_s}(1+\delta)(1+z)^{3/2}[H(z)/\frac{dv}{dr}] \qquad (4.45)$$

in which $A = 2.85 \times 10^{-15}s^{-1}$ is the Einstein coefficient, k_B is Boltzmann constant, h is Plank constant, $\nu_{21} = 1420.4MHz$, dv/dr is the peculiar velocity structure. Moreover, collision and resonant scattering of Lyman alpha photons can drive T_s to the gas kinetic temperature T_k as:

$$T_s = \frac{T_{CMB} + y_c T_k + y_\alpha T_k}{1 + y_c + y_\alpha} \tag{4.46}$$

where y_c and y_α represent collisional excitation and Lyman alpha resonance respectively.

The spin temperature T_s will be decoupled from the CMB temperature by the conditions: (1) collision between hydrogen atoms which depends on the local gas density and temperature or (2) Lyman alpha pumping which depends on the UV radiation field. The flux can be detected by radio telescope from brightness temperature which is obey the radiative transfer equation(Iliev et al. 2002). Thus, the physical regimes can be drawn as below(Carilli 2006; Fan, Carilli & Keating 2006; Santos & Cooray 2006): at $z > 200$, there is equilibrium between T_{CMB}, T_k and T_s so that no 21cm signal; at $30 < z < 200$, the gas cools as $(1+z)^2$ faster than $(1+z)$ for the CMB, but T_s and T_k are still coupled by collision since the mean density is high, the HI 21 cm signal would be seen in absorption; at $z \sim 20 - 30$, collision can no longer couple T_k and T_s, but the Lyman alpha photons from first luminous objects(Pop III stars and mini-quasars) could induce local coupling of T_k and T_s, thereby showing 21cm absorption regions(e.g., Chen & Miralda-Escude 2006); at $6 < z < 20$, due to the first stars, galaxies and black holes, the T_k is larger than T_{CMB} globally(Furlanetto, Sokasian & Hernquist 2004) and most model expectations and observations play during this period.

Shapiro et al. (2006) find that the 21cm signal from gas in minihalos dominates over that from the gas in IGM. However, it is analyzed that, minihalos only dominate the observed fluctuations if the IGM remains cold and the Lyman alpha background remains small, while in reality the minihalo would be buried within the IGM signal and surrounded in the feedback environment(Furlanetto & Oh 2006). Thus, it is difficult to detect minihalos except the way of so-called 21cm forest, in which minihalos appear as weak 21 cm absorption features toward a bright background radio source(Furlanetto 2006). The observations of Primeval Structure Telescope(PAST), Mileura Widefield Array(MWA), Low Frequency Array(LOFAR) and Square Kilometer Array(SKA) would open the new era for the universe beyond redshift $6 - 10$ in the next few years.

Chapter 5

Conclusion

In the thesis, under the framework of coevolution between central black hole and the host spheroid, the properties of two kinds of objects, AGNs and primordial galaxies, are concerned especially at high redshift from the anti-hierarchical baryon collapse model of Granato et al. (2004). Especially, we successfully predict the AGN luminosity functions and the reionization issues. The results are agreement with the observations. In our model, the black hole growth induces the time delay which is between the moment of halo virilization to the time of QSOs shine. The feedback of AGNs and SNe play a vital role for the black growth, gas cooling and star formation. The mergers are viewed as the minor events. Therefore, the assembling of the central black hole and the star formation in the host spheroids at each redshift bin is different from the prediction of the traditional hierarchical way thus our model can naturally explain the observational downsizing features.

During the thesis, we have obtained the merits as the following:

(1) From HST/ACS deep survey, we have selected the high redshift AGN candidates; the X-ray and infrared counterparts have been concerned; after the identification of these candidates, the AGN luminosity function at redshift 4.5 has been successfully extended into the low luminosity part;

(2) AGN luminosity functions from redshift 1.5 to 6 have been derived under the model of Granato et al. (2004); We find that the black hole assembling and AGN luminosity functions can be treated as the anti-hierarchical way due to the time delay by the black hole growth and the feedback of

AGNs and SNe;

(3) The galaxies evolve in general as the passive way after the violent starburst; The UV emission from the protogalaxies could be enough to reionize the universe at redshift around 6-8; after the beginning of about 10^7 years, the primordial galaxies would pass into the dust phase, shown as SCUBA galaxies, in the mean time, the central black holes grow and finally shine as QSOs.

One of the most important challenges for modern astrophysics and cosmology is to understand the intrinsic relations and evolutionary traces of cosmic objects among numerous observational phenomena. In the Chapter 3, as shown in the Fig. 3.6, we realize that QSO shine is the final stage of the coevolution between AGN and host galaxy. In the Chapter 4, the initial stage of the timescale about a few of 10^7 years with the dust-free environment is for the protogalaxies which emit the UV photons to ionize the high redshift universe.

Moreover, the observational relative features of other kinds of objects could be put forward:

(1) from deep photometry survey, it has been found that the primordial galaxies with violent star formation in the small halos could be formed at high redshifts $z > 6$(Hu et al. 2004; Bouwens et al. 2006). Lyman break galaxies(LBGs), partly obscured by the gas and dust, showing strong star formation by UV emission at redshift $3 - 4$, are viewed as the young spheroids(e.g., Matteucci & Pipino 2002). The dwarf blue galaxies in the local universe will be polluted even they still have low metallicity of one third solar(Tosi et al. 2001; Lee & Skillman 2004). All of these young objects have shown their star-forming evidences at different redshift.

(2) Extremely Red Object(ERO) population is typically selected by, for example, $(R - K)_{vega} > 6.0$. Despite those old evolved galaxies whose red colors are caused by a dearth of young and luminous stars, we refer the EROs as the dusty starburst galaxies, their red colors are due to the dust absorption and re-radiation(e.g., Graham & Dey 1996; Cotter, Simpson & Bolton 2005; Stern et al. 2006);

(3) Combined with the X-ray properties, some EROs are confirmed to host obscured QSOs(Severgnini et al. 2005). The central black hole masses

could be higher than $10^9 M_\odot$ and they are radiating at Eddington ratios $L/L_{Edd} < 0.1$(e.g., Maiolino et al. 2006).

(4) Deep SCUBA survey has discovered a population of submillimeter(300−100μm) galaxies(SMG, Barger, Cowie & Sanders 1999; Blain et al. 1999; Chapman et al. 2002; Borys et al. 2002; Webb et al. 2003) which are actually the dust-enshrouded galaxies(Simpson et al. 2004; Pope et al. 2005) identified by multi-band observation. The sample of infrared luminous Lyman break galaxies is viewed as a population that bridges LBGs and SCUBA galaxies(Huang et al. 2005). The evolutionary relation between the protogalaxies and SMG has been investigated in the Section 4.4. Our results indicate that at high redshift the young galaxies would transfer into SCUBA phase after the timescale of 10^7 years from the beginning stage of galactic formation.

(5) On the other hand, the observation by Chapman et al. (2005) found that bright SMGs contribute a comparable star formation density to Lyman break galaxies, and suggested a close link between SMGs and the formation and evolution of the galactic halos that host QSOs. The black hole growth in the center of SMGs will mainly occur accompanied with the obscured far-infrared luminous phase of stellar component which is likely associated with the formation of the spheroids(Borys et al. 2005) and the central black holes shine detected by X-ray observation(Alexander et al. 2005). While high redshift AGN population which is bright in the mid-infrared but optically obscured has been tested by millimeter observation(Lutz et al. 2005). Actually, in the thesis, the results of AGN luminosity functions shown in the Section 3.3.3 are also consistent with the properties of host galaxies(Silva et al. 2005; Cirasuolo et al. 2005) under the coevolution model of Granato et al. (2004).

(6) A possible evolutionary path has been proposed to link AGN and starburst phenomena: starburst–NLS1–post starburst–luminous AGN from the observational sample SDSSJ085338.27+033246.1(Wang & Wei 2006). From the sample of galaxies with both post-starburst(strong Balmer absorption lines) and AGN(based on the emission line ratio) signatures, it has been suggested that AGNs may outlive starbursts in the starburst-AGN connection(Goto 2006).

All of these evidences above are consistent with the results predicted by our model of Granato et al. (2004). Based on the properties of the objects of dwarfs, starbursts and AGNs at different redshift, from the unified understanding of the whole scenario about galactic formation and evolution so far, it is proposed that the intrinsic evolutionary sequence of galaxies could be:

blue dwarfs(protogalaxies)−−Lyman break galaxies at high redshift and star-burst galaxies at low redshift−−SCUBA phase at high redshift and EROs at low redshift−−QSO/AGN shine

From this evolutionary chain, we draw the conclusion: the blue dwarfs at high redshift emit UV photons and ionize the universe, the vestiges are shown as red passive dwarfs in the local universe; the young galaxies with violent star formation are viewed as Lyman break galaxies at high redshift and starburst galaxies at low redshift respectively; the galaxies still continually evolve, but in the dusty environment which could be polluted by the SNe, the emission from the massive galaxies at high redshift could be absorbed by the dust and be detected by submillimeter band while the EROs are the dust-obscured objects at low redshift; in the mean time, the central black holes grow enough to emit the detectable light, first in the X-ray band, then, they are observed as the unobscured QSOs.

This evolution sequence provides the prime physical understanding to some observational phenomena of cosmic objects. Since the interesting points in the thesis are focused on the issues at high redshift, based on this sequence, the topics such as primordial black holes, first generation stars/galaxies and their interaction with CMB photons could motivate the research to the earlier universe in the future.

Appendix A

Optical Instruments and Data Process

A.1 HST/ACS Photometry

The images of B, V, i and z band of the GOODS survey have been obtained by HST/ACS observations. In this appendix, the characteristics of HST/ACS and the data calibration are given in detail. After a simple introduction of HST, the observing modes of ACS are described. Then, the exposure time are mentioned since it is one of important parameters for the survey of faint point-like objects such as AGNs. As the popular detector, CCD can not be ignored and the treatment to the instrument signatures due to the CCD properties are presented. Finally, the data calibration steps of HST/ACS are listed[1].

A.1.1 Hubble Space Telescope

Hubble Space Telescope(HST) is a 2.4-meter reflecting facility deployed in a low orbit of 600 kilometers with the spatial resolution about 0.05 arcseconds. Current observing instruments onboard HST are Wide Field/ Planetary Camera 2(WFPC2), Space Telescope Imaging Spectrograph(STIS),

---

[1] The figures and some materials mentioned in this section are cited in ACS instrument handbook version 3.0, 2002. A comprehensive review of photometric performance and calibration is given by Sirianni et al. (2005).

Near Infrared Camera and Multi-Object Spectrometer(NICMOS) and Advanced Camera for Surveys(ACS).

WFPC consists of an L-shaped trio of wide-field sensors and a smaller but high resolution camera that can be used especially for wide field surveys.

STIS is a two-dimensional spectrograph using three detectors for the wavelengths from UV to near infrared band.

NICMOS is the instrument providing the capability for infrared images and spectroscopic observations of the band between 0.8 and 2.5 micrometers.

ACS is designed to have a deep and wide-field survey capability from the visible to near infrared band, imaging from near-UV to near infrared with the point spread function critically sampled at 6300Å. It has played a major role in the GOODS observation and should be described comprehensively.

A.1.2 Observing Modes of ACS

ACS has three channels:

(1) Wide Field Channel(WFC) has 202×202 $arcsecond^2$ field of view from 3700 to 11000Å. In this channel, a CCD of 2048×4096 is provided.

(2) High Resolution Channel(HRC) has 29×26 $arcsecond^2$ field of view from from 2000 to $11000\AA$ with the CCD 1024×2024.

(3) Solar Blind Channel(SBC) has 35×31 arcsecond field of view from 1150 to $1700\AA$ with the photon-counting detector which provides a two-dimensional ultraviolet capability.

The optical design of WFC and HRC/SBC(Sirianni et al. 2005) is shown in the Fig. A.1.

ACS has three filter wheels, two shared by the WFC & HRC and a separate wheel dedicated to the SBC. When the selected ACS camera is WFC or HRC, the appropriate filter in one wheel is rotated into position and a clear aperture is automatically selected on the other wheel. For SBC imaging, the single filter wheel is simply rotated to the required position. Parallel WFC and HRC observations are possible for some filter combinations.

There are 4 pass-bands selected by ACS survey for the Hubble Deep Field(HDF) observation. They are F435W Johnson B, F606W Broad V, F775W SDSS i and F850LP SDSS z. These filters are full-sized and used by

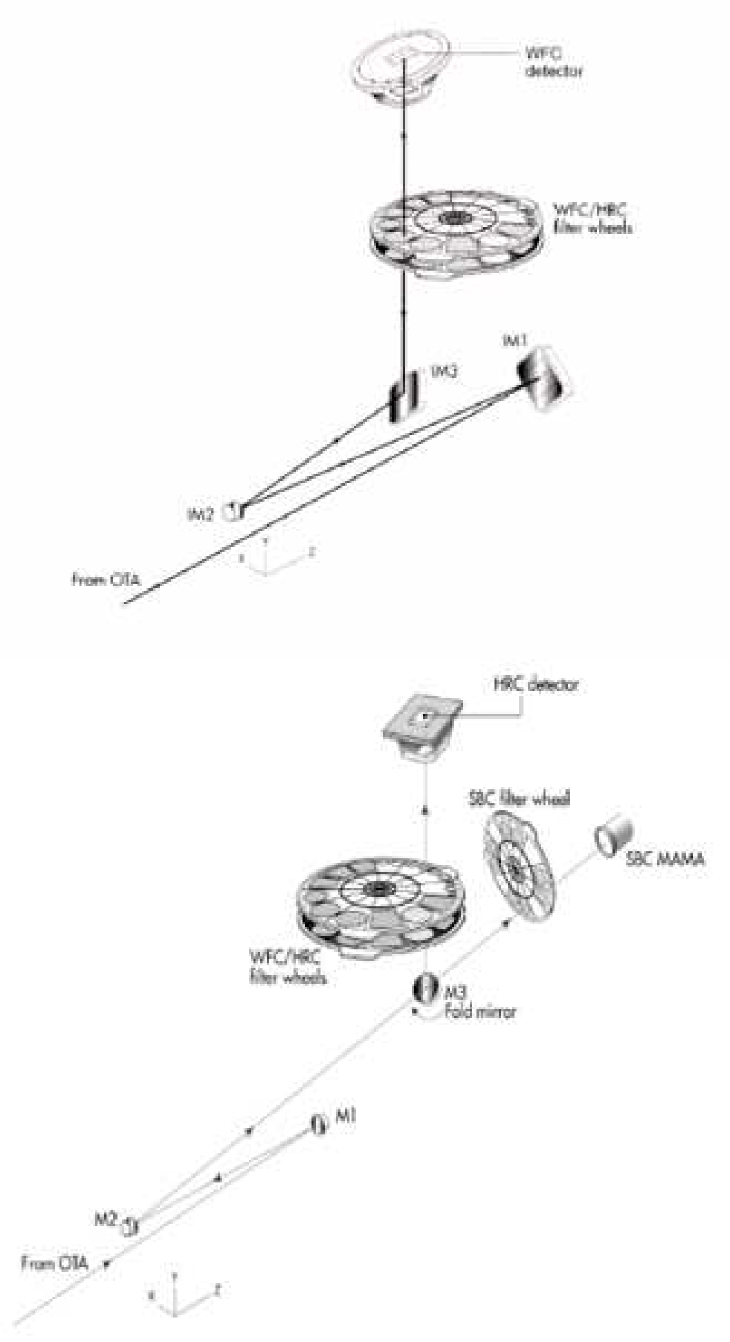

Figure A.1: ACS Optical Design

WFC and HRC. The main parameters of these four pass-bands are presented in the Table A.1 and the filters are shown in the figures of A.2, A.3, A.4 and A.5.

Table A.1: The parameters of 4 passbands in HST/ACS

Filter	central wavelength	width(Å)	Description	camera
F435W	4227	1038	Johnson B	WFC/HRC wheel 2
F606W	5907	2342	Broad V	WFC/HRC wheel 1
F775W	7764	1528	SDSS i	WFC/HRC wheel 1
F850LP	9445	1229	SDSS z	WFC/HRC wheel 1

As a brief review, ACS provides wide field of view about $202 arcsecond \times 202 arcsecond$, point spread function(PSF) in a region of about 5×5 pixel, high throughput at wavelengths larger than $3700 \AA$ and good spatial resolution up to 0.027 arcsecond in the HRC.

A.1.3 Exposure Time

In an imaging survey, the exposure time required to achieve a given signal to noise ratio is the result of five main ingredients:

(1) The object count rate C derived from the instrument sensitivities, reflectivity and transmission of the optics, passband, quantum efficiency of the detector, etc.;

(2) Since extinction can reduce the counts particularly in the ultraviolet, the extinction correction has been applied for calculating the exposure time;

(3) The area(in pixels) over which those counts are received N_{pixel};

(4) Measurement of the sky background B_{sky}. The sources of the sky background which affect ACS observations include Earth shine due to the near obit of the HST, zodiacal light and geocoronal emission.

(5) Determination for the detector background B_{dec} which comes from the CCD dark current.

For the CCD detector, the integration time to reach a signal to noise ratio

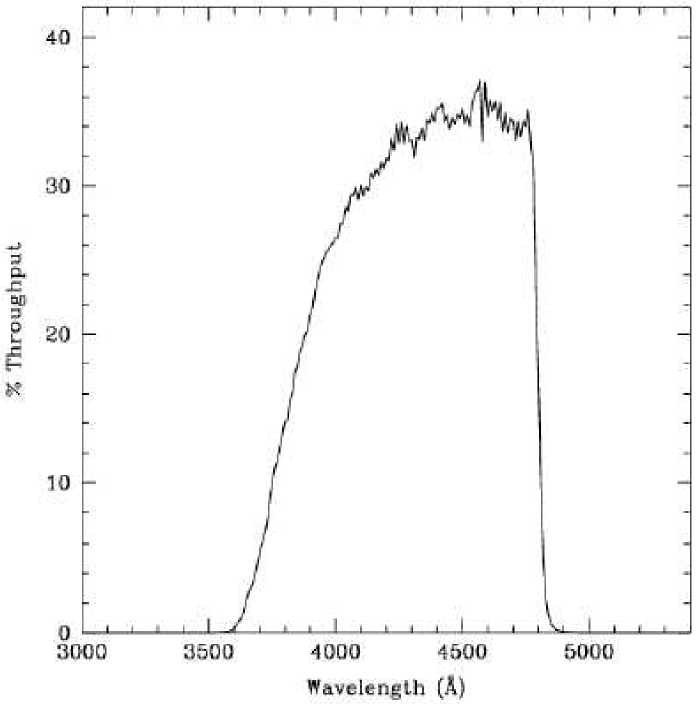

Figure A.2: ACS WFC/F435W Johnson B filter

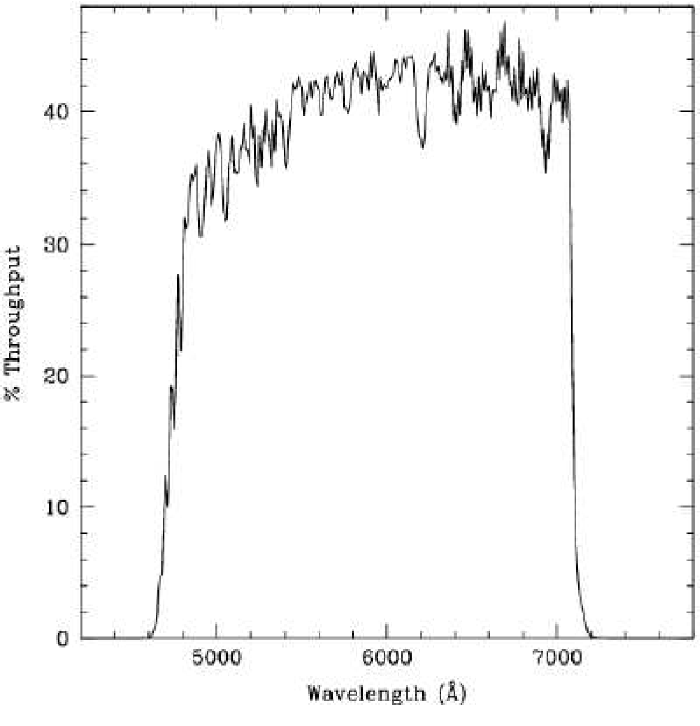

Figure A.3: ACS WFC/F606W Broad V filter

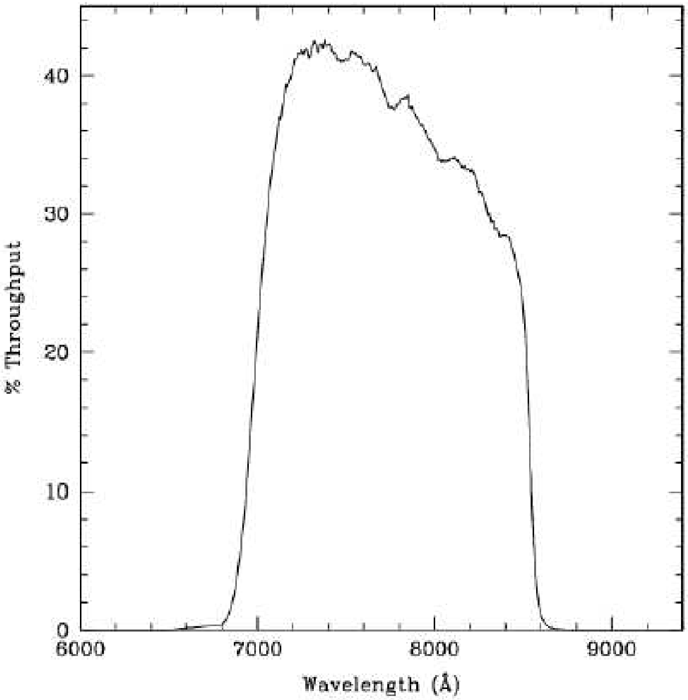

Figure A.4: ACS WFC/F775W SDSS i filter

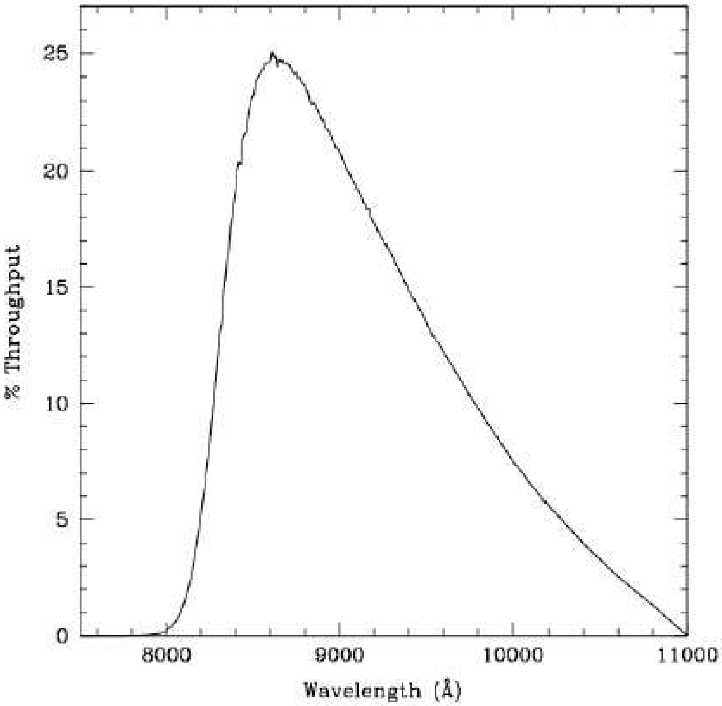

Figure A.5: ACS WFC/F850LP SDSS z filter

Σ, is given by:

$$t = \frac{\Sigma^2[C + N_{pix}(B_{sky} + B_{dec})]}{C^2} \tag{A.1}$$

For example, given the signal to noise of 10 for a point source of $V = 26.5$, the total time of the filter F555W in WFC is about 5835s to 6124s.

A.1.4 CCD Properties

The charge-coupled device(CCD) is a solid-state integrated circuit that stores the electrons produced by incident photons as discrete packets of charge in potential wells maintained by an electric field(Sterken & Manfroid 1992). Nowadays, it is the most popular detector used in the space and ground-based telescopes. In this section, the description is divided into two parts. The first part is about the general characteristics of the CCD while the second part is about the CCD of ACS.

The main characteristics of a CCD are:

(1) Readout noise(RON): the additional noise to the number of the counts recorded;

(2) Charge transfer efficiency(CTE): the effective efficiency of a CCD at moving charge from one pixel location to the next one;

(3) Bad columns: the columns of a CCD array that do not read out charge;

(4) Fringes: the wave patterns due to the interference effects by the layered structure of the CCD;

(5) Dark current: all kinds of electrons produced by the thermal motions as:

$$I_d = A\exp(-B/kT) \tag{A.2}$$

where I_d is dark current and A and B are constants. Liquid-nitrogen is used for cooling the detector and reduce the dark current;

(6) Cosmic ray events: produced by the cosmic rays generated in the upper atmosphere which hit the CCD and cause a signal.

Due to the CCD characteristics mentioned above, the observational data contain both astronomical signals and the effects from the CCD detector.

Therefore, the observational data need to be processed to remove the CCD signature[2]. It involves a number of steps:

(1) Bias subtract and trim the image: a typical CCD contains a number of pixels about 2048×4096. Some of the pixels in the raw image are not physical. They just correspond to the bias level and have to be trimmed out. The bias level, in turn, has to be subtracted to each pixel, either by estimating its value in the non-physical pixels or estimating a zero level exposure representing the bias image. This treatment is called bias frames or zero frames.

(2) Prepare combined dome flat: using a standard lamp and a screen, one can obtain the so-called dome flat for each filter.

(3) Prepare combined sky flat: standard lamp to correct the pixel-to-pixel response has not the same spectral distribution as the light sky and may present some illumination gradient. Therefore, a sky flat is needed. It can be taken at dawn or dusk so that there can be a smooth sky background.

(4) Combine the dome and sky flat: put the flats together and create a refined version of the flat frame to get rid of the effects of bad pixels and fringes.

(5) Remove cosmic ray events: the simple way is to stack multiple images using a median filter to obtain a blemish-free final image.

Besides these general properties, CCD as the detector for HST/ACS has its features which are described in the following.

The CCD of ACS does not suffer from the quantum efficiency hysteresis, it means that CCD responds in the same way to the light levels over its whole dynamic range.

The CCD of ACS exhibits fringing in the red long-ward of about $7500\mathring{A}$. The amplitude of the fringing is a function of wavelength and spectral resolution. This fringe patten can be corrected by an appropriate flat field.

The CCD for space observation can not avoid the attack of cosmic rays. The fraction of pixels affected by cosmic rays varies from 1.5% to 3% during a 1000 second exposure time. The distribution of the number of pixels affected by a single cosmic ray is strongly peaked at 4 to 5 pixels. The size distribution of cosmic peaks near 0.4 pixels which is narrower than the PSF of the point

---

[2] see also www.lco.cl/magellan/ instruments/magic and www.astro.caltech.edu/∼ sco/

single source so that distributions of sizes and anisotropies can be useful for distinguishing cosmic rays from astrophysical sources in a single image.

The CCD of ACS is also affected by the dark current and the hot pixels. The number of the hot pixels even grows daily so that subtraction of a superdark frame is important to reduce the influence of the hot pixels from dark current.

To remove all kinds of the instrumental signature from the ACS data, the CCD calibration of ACS has been described in the section below.

A.1.5 Calibration

The whole observation of HDF is: selection of primary field⟶selection of flanking field⟶filter selection⟶data reduction.

The data reduction concludes a series of steps(Williams et al. 1996; Casertano et al. 2000):

(1) standard pipeline calibration: Since the charge in each pixel of CCD is added a bias value, the superbias frame has been done; The superdark frame has been taken for removing thermally-induced dark current; The flat field frame has been operated in this pipeline;

(2) Even with the superdark treatment, some hot pixels still remain. The dither strategy is used to deal with these hot pixels;

(3) Cosmic ray rejection has been involved;

(4) Due to the low orbit of the HST, the observations have the effect of the scattered light. The subtraction has been done by registering the bright and dark images, subtracting the dark from the bright to remove the sources, smoothing to remove any residual sources and subtracting this smoothed sky image from the bright frame;

(5) Correct the geometric distortion due to the shifts and rotations of the images by dither strategy;

(6) The preliminary images can be obtained after above series;

(7) Use the preliminary images to have a median-combined image also by dither strategy;

(8) Other corrections and adjustments should be take into account such as inter-chip alignment adjustment due to the alignment of detectors changed by

time, photometry balancing due to the difference sensitivities of the detectors, sky background correction due to the varied sky brightness and so on.

(9) Calculation of the weights of all the images and then combination for the final image.

The dither strategy plays an important role for the dark current subtraction, removal hot pixel, geometric distortion and combined images. the details of the dither are described in the HST dither handbook(version2.0, 2002). Here, it is just mentioned briefly. The key point is that the observations are obtained at nine separate points separated by 2 arcseconds. The images may shift from one point to another. The shift between the points can not only average and smooth the low-level detector features such as the imperfections of the flat field and dark current subtraction, but also can reconstruct a combined image with better sampling and quality thus greatly improving the ability to discern the small-scale details.

A.2 Optical Observation Techniques

In the thesis, high redshift AGN candidates have been selected using the photometry survey of ACS. The software Source Extractor(SExtractor) has been used to process the survey data. The photometry method is described in the first part of this section. The optical spectra are taken for the final AGN identification through spectrograph placed at the large ground-based telescopes such as VLT and Keck. The optical spectroscopy results of VLT are described in the second part of this section.

A.2.1 Photometry

The traditional photometric systems are the Johnson-Morgan UBVRI system and the infrared JHKLM system(Sterken & Manfroid 1992). The filters used in the HDF-ACS (B, V, i and z) has been shown in the Appendix A.

The optical magnitude can be defined as:

$$m_\lambda = -2.5 \log f + f_0 \tag{A.3}$$

where f is the observed flux and f_0 is the magnitude scale at zero point. The zero points of the magnitude systems are usually defined with respect to one or more standard stars(Vega etc.). For the AB magnitude used in the HDF, we use the definition:

$$m_{AB} = -2.5 \log f - 48.57 \tag{A.4}$$

Since a huge amount of survey data have been obtained by HST/ACS, the Source Extractor[3](SExtractor or SE) becomes one of the powerful tools for this kind of photometric survey. This software carries out an automated detection and produces photometric catalogs for imaging data. The SExtractor data analysis proceeds with the following steps:

(1) Measure the background and its RMS noise(Background and RMS maps);

(2) Subtract background;

(3) Filter(convolve with specified profile);

(4) Find objects(thresholding);

(5) Deblend detections(break up detection into different objects);

(6) Measure shapes and positions;

(7) Clean(reconsider detections, accounting for contributions from neighbors);

(8) Perform photometry;

(9) Classify/index level of fuzziness–more star like or galactic;

(10) Output catalog.

Due to the different morphology of the objects which need to be measured by SExtractor, there are several photometric apertures(parameters) provided in the SExtractor:

(1) ISO – photometry derived from the counts above the threshold minus the background;

(2) ISOCOR – ISO photometry, corrected for loss as a Gaussian profile;

(3) Auto – Photometry from flexible elliptical aperture;

(4) Aper – Photometry from circular, user specified apertures.

(5) Best – Choice between AUTO and ISOCOR;

In the Fig. A.6, four different apertures are illustrated. Different apertures can be used corresponding to particular objects(stars or galaxies).

---

[3] contents and figures are extracted from Source Extractor for dummies V.4

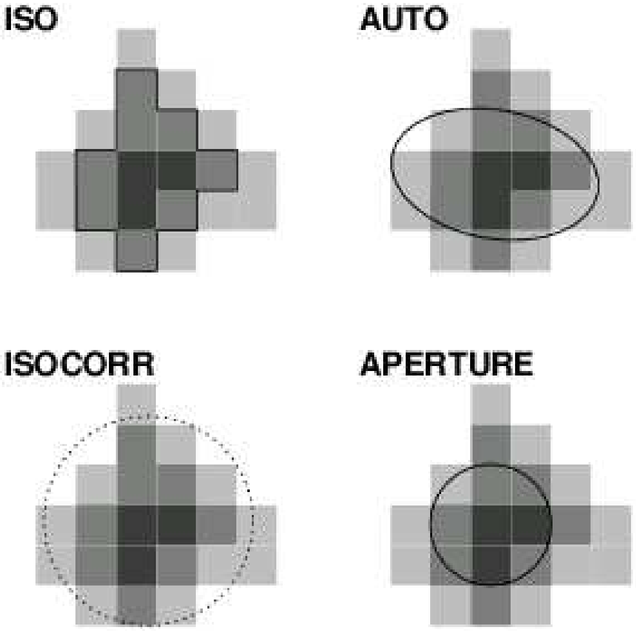

Figure A.6: Different apertures used for photometry by SExtractor

Thus, facing the image data and catalog produced by SExtractor, one may choose exactly the photometry parameter to obtain the accurate magnitudes of the objects which he wants to measure.

The faint objects(high redshift AGNs in the thesis) are often the interesting targets in a survey image. SExtractor provides the tools for detection and measurement of them. In the multi-band survey, SExtractor has the in-built ability to detect sources in one image and subsequently carry out photometry on the found apertures in another image. It has the advantage that the photometry on an object has the same apertures in all bands and catalogs, and the different catalogs need not be matched each other.

In this context, there are 3 images can be used by this package:

(1) Meta images – the result that two or several bands to be used for object detection while doing the photometry in the individual bands;

(2) Maximum likelyhood images – to construct a χ^2 image and do the detection on these objects;

(3) Optimal image – the band where the target objects are the bright-

est(i.e. the reddest band available for field galaxies) or the band with the longest exposure is used as the detection image and the apertures of that band are used for the photometry in all the other bands.

After process of Sextractor, the photometry catalogs are available. The coordinates of the objects, the different aperture parameters, the corresponding magnitudes of different filters and the errors are all included.

A.2.2 Spectroscopy

Several basic facilities can be used for obtaining the astronomical spectra.

The prism is used in front of a telescope objective to transform each object image into an image of its spectrum. The grating is a system of parallel slits, where the slit width is of the same order as the wavelength of the incident radiation, which is capable of dispersing light into its spectrum. The grism(grating plus prism) is a right-angled glass prism with a transmission diffraction grating deposited on the hypotenuse surface.

The spectrum produced by the grating is deflected by the prism to remain on the optical axis and the apex angle of the prism is chosen to get a certain wavelength in the center of the detector.

The key parameters defining the characteristics of an astronomical spectrograph are:

(1) Spectral resolution defined as:

$$R = \frac{\lambda}{\Delta\lambda} \tag{A.5}$$

The values are from a few hundred up to $10^5 \sim 10^6$;

(2) Spectral range: typically, an optical spectrograph may cover a decade about 400-800nm. Using a CCD detector with about 4×10^3 pixels in the direction of the dispersion, a sampling of about 1 $\mathring{A}$ per pixel is obtained;

(3) Sensitivity: for a spectrograph it is important to estimate the magnitude of the faintest objects for which a useful spectrum can be recorded. The formula is(Kitchin 1991):

$$m = 12 + 2.5 \log \frac{sDT_D gqt(d\lambda/d\theta)}{f_1 f_2 \alpha H} \tag{A.6}$$

where T_D is the diameter of telescope; H is the height of the spectrum; t is the exposure time; g is the optical efficiency of the system; q is the quantum efficiency of the detector; α is the angular size of the stellar image at the telescope's focus; f_1 is the focal length of the collimator; f_2 is the focal length of the imaging element and parameter $s = f_1\lambda/D$. Normally, with an 8m telescope of resolution about 10^3, one can get to $m_{AB} \sim 25mag$ in a few hours of observation.

Often several targets of interest are present in the field of view of the telescope and it is possible to take advantage of multiple object spectroscopy(L$\acute{e}$na 1988). The application of fiber optics for spectroscopy is to take the energy from various points of the field and bring it to the slit of the spectrograph. Another way is to take the image with a CCD and then slits are made in a mask at the positions of the desired objects.

Very Large Telescope(VLT) has given a particular contribution to the spectroscopic observations of the GOODS. Spectroscopic surveys have been carried out with FORS 1& 2(Szokoly et al. 2004; Vanzella et al. 2004). In the description of Vanzella et al (2004), the 300I grism was used as dispersing element without order-separating filter providing a scale of roughly $3.2\AA/pixel$. The standard resolution of the configuration is 860, which corresponds to about $9\AA$ at $8000\AA$. The spatial scale of FORS2 is $0.126''/pixel$, the slit width is always 1 arcsecond. Dithering of the targets along the slits is applied in order to improve the sky subtraction, the mean shift is ±8 pixels.

The survey presented by Szokoly et al.(2004) was especially dedicated to the investigation of X-ray sources. Objects were identified primarily from the deep VLT/FORS imaging data, reaching a depth of $R = 26.5$. Possible optical counterparts of X-ray sources are selected based on the estimated astrometry error of the X-ray object. For a bright point source the astrometry rms error is about 0.5 arcsecond. The observations use the 150I grism which provide a pixel scale(dispersed) of 280Å/mm, or roughly 5.5Å/pixel. The normal resolution of the configuration is $R = 230$.

The data reduction and flux calibration are followed the standard procedures. For simplicity, the minor changes are ignored in this section. The redshift determination has been carried out through the identification of prominent features, such as the 4000Åbreak, CaII H and K absorption, Balmer lines, or, Ly-alpha, MgII, [OII], CIV in emission. As an example, in the results of Szokoly et al. (2004), spectroscopic redshifts have been obtained for 168 X-ray sources, of which 137 have both reliable optical identification and redshift estimate. This survey gives the catalog of 40% completeness considering the whole X-ray sources, and 70% completeness considering the subset in the central 8' radius with optical counterparts at $R < 24$.

Appendix B

Luminosity Function

One of the direct results of an observational survey is the information about space distribution of the objects. The standard calculation of luminosity function using the observational data are presented in the section B.1. The theoretical procedures for the derivation of luminosity function are discussed in the section B.2.

B.1 Calculation from Observational Data

Given a set of luminosities of a certain type of objects within the different redshift bins, the luminosity function, which is the number per unit volume in a certain luminosity domain at a certain redshift, can be computed. Beside the sophisticated C^- method(Lynden-Bell 1971), the standard way to calculate the luminosity function is the following (Schmidt 1968, Krolik 1999):

in a flux-limited sample, the maximum luminosity distance at which a particular member of a sample can be seen is

$$R_{max,i} = (F_i/F_{min})^{1/2} R_i \tag{B.1}$$

where F_{min} is the limit flux and R_i is the actual distance of object i. In Euclidean geometry, the volume is $V = (1/3)R^3\Delta\Omega$. Then, we have the relation between volume and flux

$$< V_i/V_{max,i} >=< R_i^3/R_{max,i}^3 >=< (F_{min}/F_i)^{3/2} > \tag{B.2}$$

The V/V_{max} test is based on the assumption that V/V_{max} has a uniform distribution from 0 to 1 for the total sample if it is complete, or, $< V_i/V_{max,i} >= 1/2$ in general. For objects at a cosmological distance, the co-moving volume is given by

$$V_{co,i} = \Delta\Omega_i \frac{R^2(z)}{1+z} \frac{\Delta z}{\sqrt{1+\Omega_M z + \Omega_\Lambda[1/(1+z)^2 - 1]}}. \tag{B.3}$$

The sample at a certain redshift can be divided into a few groups by the luminosity or absolute magnitude intervals. The luminosity function at a certain redshift can be computed as:

$$\frac{dn}{dz} = \sum_i^N \frac{1}{2\Delta L V_{co,i}} \tag{B.4}$$

where $2\Delta L$ is the full luminosity width.

In the case of overlapping samples, for example, if we need to combine the luminosity functions of different surveys, an improved V/V_{max} method can be used (Avni & Bahcall 1980).

Besides the description above, a further step is needed to relate the same intrinsic properties among all objects, because the observer sees a different part of the intrinsic spectrum, depending on the redshift of the object observed. To compare an object at one redshift with those at others, it is necessary to normalize to certain standard wavelength or frequency within the object's spectrum. This concept is so-called K-correction or redshift correction. The K-correction includes the change of properties(e.g. the luminosity) as a function of λ_e, the wavelength of the emitted radiation, and the change in the bandwidth $d\lambda_e$ to $d\lambda_o$ (Weedman 1986).

In this context, for simplicity we only concentrate on the K-correction estimated for a power-law continuum as a representation of the QSO spectrum. The effects of emission and absorption lines are ignored.

The relation between the observational frequency ν_0 and the intrinsic frequency ν_e is given by:

$$\nu_e = (1+z)\nu_0 \tag{B.5}$$

such that the frequency interval is:

$$d\nu_e = (1+z)d\nu_0 \tag{B.6}$$

For AGNs, we know that the intrinsic luminosity is a power law of

$$L_{\nu e} \propto \nu_e^{\alpha} \tag{B.7}$$

where α is the power law index. Since $\nu = c\lambda^{-1}$, $d\nu/d\lambda = -c\lambda^{-2}$ and for the same interval, $L_{\nu e} d\nu_e = -L_{\lambda e} d\lambda_e$, the intrinsic luminosity is written as:

$$L_{\lambda e} = L_{\nu e} c \lambda_e^{-2} \propto \nu_e^{\alpha} \lambda_e^{-2} \propto \lambda_e^{-(2+\alpha)} \tag{B.8}$$

Thus, we have the relation

$$L_{\nu e} = L_{\nu 0}(\nu_0/\nu_e)^{-\alpha} = L_{\nu 0}(1+z)^{\alpha} \tag{B.9}$$

and

$$L_{\lambda e} = L_{\lambda_0}(1+z)^{2+\alpha} \tag{B.10}$$

At high redshift space, the K-correction of AGNs could be with large uncertainty because of the lack of statistics on the continuum shape between the rest-frame UV and optical region(Fan et al. 2001a) due to the absorption of intergalactic medium.

To fit the parameters of luminosity function and its evolution models, the unbinned maximum likelihood method(Marshall et al. 1983) is often selected. Given an analytic form of luminosity function $\Phi(L, z)$, the maximum likelihood function is:

$$S = -2\sum_{i=1}^{N} ln[\Phi(L_i, z_i)] + 2\int\int \Phi(L, z)\Omega\frac{dV}{dz}dzdL \tag{B.11}$$

where (dV/dz)dz is the differential comoving volume, Ω is the sky area covered by the observational sample, N is number of the total sources. The best fitting parameters can be obtained by minimizing the likelihood function. As an example, the optical and X-ray luminosity functions and their evolution forms are described in the section 1.4.5.

B.2 Theoretical Derivation

Generally, the AGN luminosity function can be derived as the following procedures:

First, at high redshift space, the black holes are thought to be formed in the dark matter halo due to the gravitational collapse although the details are under debate. The mass of the black hole should be the function of the mass of dark matter halo:

$$M_{BH} = f(M_{DM}) \tag{B.12}$$

The function depends on the models. For the nonlinear scenario(Haehnelt, Natarajan & Rees 1998),

$$M_{BH} \propto v_{halo}^5 M_{halo}^{5/3} \tag{B.13}$$

while for the linear scenario(Haiman & Loeb 1998),

$$M_{BH} = \epsilon M_{DM} \tag{B.14}$$

where ϵ is constant. The feedback constrained model has the relation(Wyithe & Loeb 2003):

$$M_{BH} = \epsilon_0 M_{DM}(M_{DM}/10^{12})^{2/3}[\xi(z)]^{5/6}(1+z)^{5/2} \tag{B.15}$$

where ϵ_0 is the constant to fit the M_{BH}-σ relation, $\xi(z)$ is almost unity.

Second, given the relation between black hole mass and dark halo mass, the number density of the black holes can be derived from that of dark halos. Here is one example from Haiman & Loeb (1998):

$$\frac{d^2N_{bh}}{dM_{bh}dz} = \frac{1}{\epsilon}\frac{d}{dz}\frac{dN_{ps}}{dM_{halo}} \tag{B.16}$$

and the PS mass function(Press & Schechter 1974, Sasaki 1994) at redshift z is given as:

$$N_{ps}(M,t) = \sqrt{\frac{2}{\pi}}\frac{\rho_0}{M}\frac{\delta_c}{D(t)}|\frac{1}{\sigma^2}\frac{d\sigma}{dM}|\exp(\frac{-\delta_c^2}{2\sigma^2(M)D(t)^2}) \tag{B.17}$$

Here, D(t) is the Peebles function for the growth of the perturbations and $\delta_c \approx 1.68$. For the hierarchical scenario, the merger rate of the dark matter halos should be taken into account(Lacey & Cole 1993).

Third, the luminosity can be written as:

$$L(t) = M_{bh}f(t) \tag{B.18}$$

where

$$f(t) = \frac{L_{edd}}{M_{bh}} \exp(-t/t_0) \tag{B.19}$$

Fourth, we can write the bolometric luminosity function(Haiman & Loeb 1998, Hosokawa et al. 2001):

$$\phi(L, z) = \int_z^\infty \int_{\epsilon M_{min}}^\infty dM_{bh} dz' \frac{d^2 N_{bh}}{dM_{bh} dz'} \delta[L - M_{bh} f(t_{z,z'})] \tag{B.20}$$

Fifth, the observational luminosity function is dependent on the observational band so that we need to have the bolometric correction. Yu & Lu (2004) has provided an example to obtain the B band luminosity function:

$$\phi(L_B, z) = \int C_B P(C_B | L_{bol}) \phi(L_{bol}, z) dC_B \tag{B.21}$$

where the bolometric luminosity is defined by $L_{bol} = C_B L_B$ and L_B is B band luminosity. $P(C_B | L_{bol})$ is the probability distribution function of the bolometric correction C_B at a given L_{bol}. Practically, since luminosity is a function of accretion rate which is associated with AGNs spectra, the corresponding spectra should be given to calculate luminosity function for each band. Suppose the AGN lifetime is so small compared with the cosmic timescale, the Eqs. B.20 can be equal to the Eqs. 3.26.

As for the luminosity function of galaxies, similar to the Eqs. 3.26, we may propose the analytic procedure as the following way:

$$\frac{dn}{dM_{1350,AB}} = \frac{d^2 N_{st}}{dM_{halo} dz} \frac{dM_{ahalo}}{dSFR} \frac{dSFR}{dL} \frac{dL}{dM_{1350,AB}} \frac{dz}{dt} t_{nodust} \tag{B.22}$$

where t_{nodust} is the galactic timescale for the case of dust-free. The dark halo formation rate has been given in the Section 3.1.1. The relationship between halo mass and SFR is shown in the Fig. 4.4 as an example. The AB magnitude in the wavelength $1350\AA$ can be obtained by $M_{1350,AB} = -2.5log(L_{UV}/ergs\ s^{-1} Hz^{-1}) + 51.6$. We transfer the luminosity to the SFR using the constant in the Eqs. 4.10, thus we have:

$$M_{1350,AB} = -2.5logL_0/ergs\ s^{-1} Hz^{-1} - 2.5logSFR/M_\odot yr^{-1} + 51.6 \tag{B.23}$$

in which $L_0 = 1.3 \times 10^{28} ergs\ s^{-1} Hz^{-1}$. Note that the SFR is the function of the halo mass as the general expression of Eqs. 4.5, so that the AB magnitude can be directly linked with the halo mass. As the conclusion, galactic luminosity function is the joint evolution of both dark halo distribution and the relation of SFR with the halo mass.

Bibliography

[1] Abel, T. et al., 2000, ApJ, 540, 39

[2] Abramowicz, M.A. et al., 1988, ApJ, 332, 646

[3] Adelberger, K.L. & Steidel, C.C., 2005, astro-ph/0505210

[4] Alexander, D.M. et al., 2003, AJ, 126, 539

[5] Alexander, D.M. et al., 2005, ApJ, 632,736

[6] Alonso-Herrero, A. & Quillen, A.C., 2001, AJ, 121, 1369

[7] Alonso-Herrero, A. et al., 2002, ApJ, 571, L1

[8] Alonso-Herrero, A. 2004, ApJS spitzer issue, astro-ph/0406153

[9] Alvarez, M.A., Bromm, V. & Shapiro, P.R., 2006, ApJ, astroph/0507684

[10] Alvarez, M.A. et al., 2006, astroph/0604447

[11] Antonucci, R., 1993, Annu. Rev. Astro. Astrophys, 31, 473

[12] Archibald, E.N. et al., 2002, MNRAS, 336, 353

[13] Arnouts, S. et al., 1999, MNARS, 310, 540

[14] Arnouts, S. et al., 2002, MNARS, 329, 355

[15] Avni, Y. & Bahcall, J.N., 1980, ApJ, 235, 694

[16] Bahcall, J.N. et al., 1997, ApJ, 479, 642

[17] Baldry, I.K. & Glazebrook, K., 2003, ApJ, 593, 258

[18] Balmaverde, B.& Capetti, A., 2005, A&A, astroph/0510268

[19] Bajtlik, S., Duncan, R.C. & Ostriker, J.P., 1988, ApJ, 327, 570

[20] Barkana, R. & Loeb, A., 2001, Phys. Rep., 349, 125

[21] Barger, A.J., Cowie, L.L. & Sanders, D.B., 1999, ApJL, 518, L5

[22] Barger, A.J. et al., 2003, ApJ, 584, L61

[23] Barger, A.J. et al., 2005, AJ, 129, 578

[24] Barger, A.J. & Cowie, L.L., 2005, astroph/0508558

[25] Barton, E.J. et al., 2004, ApJ, 604, L1

[26] Bate, M.R. & Bonnell, I.A., MNRAS, 1996, 356, 1201

[27] Bawer, R.G., Lucey, J.R.& Ellis, R. S., 1992, MNRAS, 254, 601

[28] Bechtold, J. et al., 2003, ApJ, 588, 119

[29] Becker, R.H. et al., 2001, AJ, 122, 2850

[30] Becker, G.D., Rauch, M. & Sargent, W.L.W., 2006, astroph/0607633

[31] Begelman, M.C., 1978, MNRAS, 184, 53

[32] Begelman, M.C., Blandford. R.C. & Rees, M.J., 1984, Rev. Mod. Phys. 56, 255

[33] Begelman, M.C., 2002, ApJ, 568, L97

[34] Begelman, M.C., 2003, in Carnegie Observatories Astrophysics Series, Vol.1: Coevolution of Black Holes and Galaxies, astro-ph/0303040

[35] Bennett, C.L., et al., 2003, ApJS, 148, 1

[36] Benson et al., 2001, MNRAS, 320, 153

[37] Bernardi, M. et al., 2003a, AJ, 125, 1866

[38] Bernardi, M. et al., 2003b, AJ, 125, 1882

[39] Bernardi, M. et al., 2005, astroph/0509360

[40] Bertin, E. & Arnouts, S., 1996, A&AS, 117, 393

[41] Bianchi, S., Cristiani, S. & Kim, T.-S., 2001,A&A, 376, 1

[42] Blain, A.W. et al., 1999, ApJL, 512, L87

[43] Blandford, R.D. & Znajek, R.L., 1977, MNRAS, 179, 433

[44] Blandford, R.D. & Payne, D.G., 1982, MNRAS, 199, 883

[45] Blandford, R.D., 2004, in Coevolution of Black Holes and Galaxies, ed. L.C. Ho, Cambridge Univ. Press

[46] Bolton, J.S. & Haehnelt, M.G., 2006, astroph/0607331

[47] Bonnell, I.A. & Bate, M.R., 2005, MNRAS, 362, 915

[48] Bonnell, I.A., Larson, R.B. & Zinnecker, H., 2006, astroph/0602469

[49] Bonnell, I.A., Clarke, C.J. & Bate, M.R., 2006, astroph/0603444

[50] Borys, C. et al., 2002, MNRAS, 330, L63

[51] Borys, C. et al., 2005, ApJ, 635, 863

[52] Bouwens, R.J. et al., 2005, ApJL, 624, L5

[53] Bouwens, R.J. et al., 2006, astroph/0509641

[54] Bower, R.G. et al., 2001, MNRAS, 325, 497

[55] Bower, R.G. et al., 2006, astroph/0511338

[56] Boyce, P.J., Disney, M.J. & Bleaken, D.J., 1999, MNRAS, 302, L39

[57] Boyle, B.J., Shanks, T. & Peterson, B.A., 1988, MNRAS, 235, 935

[58] Boyle, B.J. et al., 2000, MNRAS, 317, 1014

[59] Bregman, J.N., 2006, astroph/0511368

[60] Bressan, A. et al., 1993, A&AS, 100, 647

[61] Bromm, V., Kudritzki, R.P. & Loeb, A., 2001, ApJ, 552, 464

[62] Bromm, V. & Loeb, A., 2003, ApJ, 596, 34

[63] Bromm, V. & Loeb, A., 2006, astroph/0509303

[64] Bromm, V. & Loeb, A., 2006, astroph/0601216

[65] Bullock, J.S. et al., 2001, MNRAS, 321, 559

[66] Bunker et al., 2004, MNRAS, 355, 374

[67] Bunker et al., 2006, NewAR, 50, 94

[68] Burket, A. & Silk, J., 2001, ApJ, 554, L151

[69] Burstein, D. et al., 1997, AJ, 114, 1365

[70] Buzzoni, A., 1989, ApJS, 71, 817

[71] Buzzoni, A., 2002, AJ, 123, 1188

[72] Calura, F. & Matteucci, F., 2006, astroph/0602311

[73] Calzetti, D. et al., 1994, ApJ, 429, 582

[74] Calzetti, D. et al., 2000, ApJ, 533, 682

[75] Capak, P. et al., 2004, AJ, 127, 180

[76] Capetti, A. & Balmaverde, B., 2005, A&A, 440, 73

[77] Caputi, K.I. et al., 2005, astroph/0510070

[78] Carilli, C.L., 2006, NewAR, 50, 162

[79] Carlberg, R.G. et al., 2000, ApJ, 532, L1

[80] Casertano, S. et al., 2000, AJ, 120, 2747

[81] Cattaneo, A. & Bernardi, M., 2003, MNRAS, 344, 45

[82] Cattaneo, A. et al., 2005, astroph/0509116

[83] Cavaliere, A., Lapi, A. & Menci, N., 2002, ApJL, 581, L1

[84] Cen, R., 2003a, ApJL, 591, L5

[85] Cen, R., 2003b, ApJ, 591, 12

[86] Chapman, S.C. et al., 2002, MNRAS, 330, 92

[87] Chapman, S.C. et al., 2005, ApJ, 622, 772

[88] Chen, X. & Miralda-Escude, J., 2006, astroph/0605439

[89] Chiosi, C. & Carraro, G., 2002, MNRAS, 335, 335

[90] Choudhury, T.R. & Ferrara,A., 2006, astroph/0603617

[91] Churazov, E. et al. 2005, astroph/0507073

[92] Ciardi, B., Ferrara, A. & Abel, T., 2000, ApJ, 533, 594

[93] Ciardi, B., Ferrara, A. & White, S.D.M., 2003, MNRAS, 344, L7

[94] Ciardi, B. & Ferrara, A., 2005, Space Science Review, 116, 625

[95] Ciardi, B. et al., 2006, astroph/0511623

[96] Cimatti, A. et al., 2004, Nature, 430, 184

[97] Ciotti, L. & Ostriker, J.P., 1997, ApJ, 487, L105

[98] Ciotti, L. & Ostriker, J.P., 1997, ApJ, 551, 131

[99] Cohen, J.G. et al., 1996, ApJ, 471, L5

[100] Cohen, J.G. et al., 2000, ApJ, 538, 29

[101] Cole, S. et al., 2000, MNRAS, 319, 168

[102] Conselice, C.J. et al., 2004, ApJ, 600, L139

[103] Conselice, C.J., 2005, astroph/0507146

[104] Cooray, A. & Sheth, R., 2002, Phys. Rep., 372, 1

[105] Cooray, A. & Yoshida, N., 2004, MNRAS, 351, L71

[106] Cotter, G., Simpson, C. & Bolton, R.C., 2005, MNRAS, 360,685

[107] Cowie, L.L.& Binney, J., 1977, ApJ, 215, 723

[108] Cowie, L.L. et al., 1996, AJ, 112, 839

[109] Cowie, L.L. et al., 1999, AJ,.118, 603

[110] Cowie, L.L., et al., 2003, ApJ, 584, L57

[111] Cowie, L.L., et al., 2004, AJ, 127, 3137

[112] Cristiani, S. & Vio, R. 1990, A&A, 227, 385

[113] Cristiani, S. et al., 2004a, ApJ, 600, L119

[114] Cristiani, S. et al., 2004b, in proceedings of 'Multiwavelength mapping of galaxy evolution' conference held in Venice(Italy), A. Renzini and R. Bender (Eds.), astro-ph/0403494

[115] Croom, S.M. & Shanks, T., 1996, MNRAS, 281, 893

[116] Croom, S.M. et al., 2004, MNRAS 349, 1397

[117] Croom, S.M. et al., 2005, MNRAS 356, 415

[118] Croton, D.J. et al., 2005, astroph/0508046

[119] Crowther, P.A., 2006, Review paper to appear in proceeding of Metal Rich Universe, astroph/0608076

[120] Danese, L., et al., 2004, Proceedings of the Conference on "Growing Black Holes" held in Garching, Germany, Springer-Verlag series of "ESO Astrophysics Symposia", astro-ph/0409585

[121] Dawson, S. et al., 2001, ApJ, 122, 598

[122] De Lucia, G. et al., 2005, MNRAS, astroph/0509725

[123] De Propris, R. et al., 2005, astroph/0506635

[124] Deo, R.P., Crenshaw, D.M. & Kraemer, S.B., 2006, astroph/0603806

[125] Di Matteo, T. et al., 2003, ApJ, 593, 56

[126] Di Matteo, T., Springel, V. & Hernquist, L., 2005, Nature, 433, 604

[127] Diaferio, A. et al., 1999, MNRAS, 307, 537

[128] Dickinson, M., Giavalisco, M. and the GOODS team, astro-ph/0204213

[129] Dickinson, M. et al., 2004, ApJL, 600, L99

[130] Dijkstra, M., Haiman, Z. & Spanns, M., 2006, astroph/0510407

[131] Disney, M.J. et al., 1995, Nature, 376, 150

[132] Djorgovski, S. & Davis, M., 1987, ApJ, 313, 59

[133] Dole, H. et al., 2004, ApJS spitzer issue, astro-ph/0406021

[134] Donas, J. et al., 1987, A&A, 180, 12

[135] Dudik, R.P. et al., ApJ, 620, 113

[136] Dunlop, J.S., Cirasuolo, M. & McLure, R.J., 2006, astroph/0606192

[137] Dwek, E., 1998, ApJ, 501, 643

[138] Dwek, E., 2004, ApJ, 607, 848

[139] Eales, S. et al., 2000, AJ, 120, 2244

[140] Eggen, O.J., Lynden-bell, D. & Sandage, A.R., 1962, ApJ, 136, 748

[141] Eldridge, J.J. & Vink, J.S., 2006, astroph/0603188

[142] Elvis, M., et al., 1994, ApJS, 95, 1

[143] Faber, S.M. & Jackson, R., 1976, ApJ, 204, 668

[144] Fan, X. et al., 2001a, AJ, 121, 54

[145] Fan, X. et al., 2001b, AJ, 122, 2833

[146] Fan, X. et al., 2002, AJ, 123, 1247

[147] Fan, X. et al., 2003, AJ, 125, 1649

[148] Fan, X. et al., 2004, AJ, 128, 515

[149] Fan, X. et al., 2006, astroph/0512082

[150] Fan, X., Carilli, C.L. & Keating, B., 2006, ARA&A, astroph/0602375

[151] Fazio, G.G. et al., 2004, ApJS spitzer issue, astro-ph/0405595

[152] Fenner, Y. et al., 2006, astroph/0602489

[153] Fernandez, E.R. & komatsu, E., 2006, astroph/0508174

[154] Ferrarese, L. & Merritt, D., 2000, ApJ, 539, L9

[155] Ferrarese, L., 2002, ApJ, 578, 90

[156] Flores, H. et al., 1999, ApJ, 517, 148

[157] Fontana A. et al., 2004, A&A, 424, 23

[158] Fontanot, F. et al., 2006, A&A, submitted

[159] Fragile, P.C., Murray, S.D. & Lin, D.N.C., 2004, ApJ, 617, 1077

[160] Fragile, P.C. et al., 2004, ApJ, 604, 74

[161] Franx, M. et al., 2003, ApJ, 587, L79

[162] Fuller, T.M. & Couchman, H.M.P., 2000, ApJ, 544, 6

[163] Fukazawa, Y. et al., 1998, PASJ, 50, 187

[164] Furlanetto, S., Ssokasian, A. & Hernquist, L., 2004, MNRAS, 347, 187

[165] Furlanetto, S., 2006, astroph/0604223

[166] Furlanetto, S. & Oh, S.P., 2006, astroph/0604080

[167] Furlanetto, S., Oh,S.P. & Briggs, F.H., 2006, astroph/0608032

[168] Fynbo, J.P.U. et al., 2006, astroph/0602444

[169] Gallego, J. et al., 1995, ApJL, 455,L1

[170] Gebhardt, K. et al., 2000, ApJ, 539, L13

[171] Giacconi et al., 2002, ApJS, 139, 369

[172] Giavalisco, M. et al., 2004a, ApJ, 600, L93

[173] Giavalisco, M. et al., 2004b, ApJ, 600, L103

[174] Gibson, B.K. & Matteucci, F., 1997, MNRAS, 291, L8

[175] Gilli, R., in New X-ray Results from Clusters of Galaxies and Black Holes, Advances in Space Research, astro-ph/0303115

[176] Gilli, R., Salvati, M. & Hasinger, G., 2001, A&A, 366, 407

[177] Gilli,R., Risaliti, G. & Severgnini, P., 2001, in the proceedings of "X-ray Astronomy 2000", ASP Conf. Series, astro-ph/0103077

[178] Gnedin, N.Y. & Kravtsov, A.V., 2006, astroph/0601401

[179] Goto, T., 2006, astroph/0605202

[180] Graham, J.R. & Dey, A., 1996, ApJ, 471, 720

[181] Granato, G.L. & Danese, L., 1994, MNRAS, 268, 235

[182] Granato, G.L., Danese, L. & Francesechini, A., 1997, MNRAS, 486, 147

[183] Granato, G.L. et al., 2001, MNRAS, 324, 757

[184] Granato, G.L. et al., 2004, ApJ, 600, 580

[185] Grazian et al., 2004, AJ, 127, 592

[186] Greene, J.E. & Ho, L.C., 2005, astroph/0508335

[187] Greece, J.E., Ho, L.C. & Ulvestad, J.S., 2005, ApJ, 636, 56

[188] Greene, J.E. & Ho, L.C., 2006, astroph/0512461

[189] Grogin et al., 2005, ApJ, astroph/0507091

[190] Grupe, D., 2004, AJ, 127, 1799

[191] Grupe, D. & Mathur, S., 2004, ApJ, 606, L41

[192] Grupe, D. et al., 2004, AJ, 127, 156

[193] Guainazzi, M., Matt, G. & Perola, G.C., 2005, A&A, astroph/0508265

[194] Gunn, J.E. & Peterson, B.A., 1965, ApJ, 142, 1633

[195] Gurkan, M.A., Freitag, M. & Rasio, F.A., 2004, ApJ, 604, 632

[196] Haardt, F. & Madau, P., 1996, ApJ, 461, 20

[197] Haehnelt, M.G. & Rees, M.J., 1993, MNRAS, 263, 168

[198] Haehnelt, M.G., Natarajan, P. & Rees, M.J., 1998, MNRAS, 300, 817

[199] Haehnelt, M.G & Kauffmann, G., 2000, MNRAS, 318, L15

[200] Haehnelt, M.G. et al., 2001, ApJL, 549, L151

[201] Haehnelt, M.G., 2003, in Carnegie Observatories Astrophysics Series, Vol. 1: Coevolution of Black Holes and Galaxies, astro-ph/0307378

[202] Haehnelt M.G, Natarajan, P. & Rees, M.J., 1998, MNRAS, 300, 817

[203] Haering, N.& Rix, H., 2004, ApJ, 604, L89

[204] Haiman, Z., Rees, M.J. & Loeb, A., 1997, ApJ, 476, 458

[205] Haiman, Z. & Loeb, A., 1997, ApJ, 483, 21

[206] Haiman, Z. & Loeb, A., 1998, ApJ, 503, 505

[207] Haiman, Z., Madau, P & Loeb, A., 1999, ApJ, 514, 535

[208] Haiman, Z. & Hui, L., 2001, ApJ, 547, 27

[209] Haiman, Z., 2002, ApJ, 576, L1

[210] Haiman, Z. & Cen, R., 2002, ApJ, 578, 702

[211] Haiman, Z. & Holder, G.P., 2003, ApJ, 595, 1

[212] Haiman, Z. & Bryan, G.L., 2006, astroph/0603541

[213] Hao, C.N. et al., 2005, ApJ, 625, 78

[214] Hasinger, G., Miyaji, T. & Schmidt, M., 2005, astroph/0506118

[215] Hauser, M.G.& Dwek, E., 2001, ARA&A, 39, 249

[216] Heavens, A. et al., 2004, Nature, 428, 625

[217] Heckman, T.M. et al., 2001, ApJ, 558, 56

[218] Heckman, T.M. et al., 2004, ApJ, 613, 109

[219] Heckman, T.M. et al., astroph/0507674

[220] Hines, D.C. et al., 2006, ApJ, 641, L85

[221] Hogg, D.W. et al., 1998, ApJ, 504, 622

[222] Holland, W. et al., 1999, MNRAS, 303, 659

[223] Hopkins, A.M., 2004, ApJ, 615, 209

[224] Hopkins, A.M. & Beacom, J.F., 2006, astroph/0601463

[225] Hopkins, P.F., Narayan, R. & Hernquist, L., 2005, ApJ, astroph/0510369

[226] Hopkins, P.F. et al., 2005a, ApJ, 625, L71

[227] Hopkins, P.F. et al., 2005b, ApJ, 630, 705

[228] Hopkins, P.F. et al., 2005c, ApJ, 630, 716

[229] Hopkins, P.F. et al., 2005d, astroph/0506398

[230] Hopkins, P.F. et al., 2005e, ApJ, 632, 81

[231] Hopkins, P.F. et al., 2005f, astro-ph/0508299

[232] Hopkins, P.F. et al., 2005g, astro-ph/0508167

[233] Hosokawa, T. et al., 2001, PASJ, 53, 861

[234] Hu, E.M. et al., 2002, ApJL, 568, L75

[235] Hu, E.M. et al., 2004, AJ, 127, 563

[236] Hu, J. et al., 2005, MNRAS, astroph/0510222

[237] Hu, W. & White, M., 1997, NewA, 2, 323

[238] Huang, J.-S. et al., 2005, ApJ, 634, 137

[239] Hughes, D.H., 1998, Nature, 394, 241

[240] Idzi, R. et al., 2004, ApJ, 600, L115

[241] Iliev, I.T. et al., 2002, ApJL, 572, L123

[242] Iliev, I.T. et al., 2006, MNRAS, astroph/0512187

[243] Inoue, A.K., Iwata, I. & Deharveng, J.-M., 2006, astroph/0605526

[244] Jakobsson et al., 2005, MNRAS, 362, 245

[245] Jaffe, A.H. & Backer, D.C., 2003, ApJ, 583, 616

[246] Jarosik, N. et al., 2006, astroph/0603452

[247] Jonsson, P. et al., 2006, ApJ, 637, 255

[248] Juneau, S. et al., 2004, ApJ, 619, L135

[249] Kang, X. et al., 2004, astroph/0408475

[250] Karlsson, T., 2006, astroph/0602597

[251] Kashikawa et al. 2006, astroph/0604149

[252] Kaspi, S. et al., 2000, ApJ, 533, 631

[253] Kaspi, S. et al., 2005, ApJ, 629,61

[254] Kauffmann, G. et al., 1999a, MNRAS, 303, 188

[255] Kauffmann, G. et al., 1999b, MNRAS, 307, 529

[256] Kauffmann, G. & Haehnelt, M. 2000, MNRAS, 311, 576

[257] Kauffmann, G. et al., 2003, MNRAS, 346, 1055

[258] Kawai, N. et al., 2006, astroph/0512052

[259] Kawaguchi, T., Pierens, A. & Hur*é*, J.-M., 2004, A&A, 415, 47

[260] Kawaguchi, T., et al., 2004, A&A, 420, L23

[261] Kawakatu, N., Umemura, M. & Mori, M., 2003, ApJ, 583, 85

[262] Kawata, D. et al., astroph/0605653

[263] Kennefick, J.D., Djorgovski, S.G. & de Carvalho, R.R., 1995, AJ, 110, 2553

[264] King, A., 2003, ApJ, 596, L27

[265] King, A.R. & Pounds, K.A., 2003, MNRAS, 345,, 657

[266] Kitayama, T. et al., 2001, MNRAS, 326, 1353

[267] Kitchin, C.R., 1991, Astronomical Techniques, Chap. 3&4, IOP Publishing Ltd.

[268] Kobayashi, C., Springel, V. & White, S.D.M., astroph, 0604107

[269] Kodama, T. et al., 1998, A&A, 334, 99

[270] Kodama, T. et al., 2004, MNRAS, 350, 1005

[271] Kogut, A. et al., 2003, ApJS, 148, 161

[272] Kollmeier, J.A. et al., 2006, astroph/0508657

[273] Komossa, S. et al., 2006, astroph/0603680

[274] Kramer, R. H., Haiman, Z. & Oh, S.P., 2006, astroph/0604218

[275] Kroger, D., Hensler, G. & Freyer, T., astroph/0603189

[276] Krolik, J., 1999, Active galactic nuclei, Chap. 1, 2 & 3, Princeton university press

[277] Kroupa, P., 2001, MNRAS, 322, 231

[278] Kulkarni, V.P. & Fall, S.M., 2002, ApJ, 580, 732

[279] Kurk, J.D. et al., 2004, A&A, 422, L13

[280] La Franca, F., Andreani, P. & Cristiani, S., 1998, ApJ, 497, 529

[281] La Franca, F. et al., 2005, ApJ, 635, astro-ph/0509081

[282] Labbe, I. et al., 2006, astroph/0608444

[283] Lacey, C. & Cole, S., 1993, MNRAS, 262, 627

[284] Lacy, M. et al., 2004, ApJS spitzer issue, astro-ph/0405604

[285] Lapi, A. et al., 2006, astroph/0603819

[286] Léna, P., 1988, Observational astrophysics, Chap.7, Springer-Verlag, Germany

[287] Larson, R.B., 1969, MNRAS, 145, 405

[288] Larson, R.B., 1974, MNRAS, 166, 585

[289] Larson, R.B., 1975, MNRAS, 173, 671

[290] Larson, R.B., 1998, MNRAS, 301, 569

[291] Larson, R.B., 2006, astroph/0602469

[292] Lee, H. & Skillman, E.D., 2004, ApJ, 614, 698

[293] Levine, R. & Gnedin, N.Y., 2005, astroph/0506670

[294] Li, Y. et al., 2005, astroph/0510372

[295] Li, Y. et al., 2006, astroph/0608190

[296] Lidz, A. et al., 2005, astroph/0507361

[297] Lidz, A.,Oh, S.P. & Furlanetto, R., 2006, astroph/0512427

[298] Lintott, C., Ferreras, I. & Lahav, O., 2006, astro-ph/0512175

[299] Loeb, A. & Haiman, Z., 1997, ApJ, 490, 571

[300] Loeb, A. & Peebles, P.J.E., 2003, ApJ, 589, 29

[301] Lonsdale, C.J. et al., 2003, PASP, 115, 897

[302] Lu. Y., et al., 2005, astroph/0508624

[303] Lutz et al., 2005, ApJL, 632, L13

[304] Lynden-Bell, D., 1969, Nature, 223, 690

[305] Lynden-Bell, D., 1971, MNRAS, 155, 95

[306] MacLow, M. & Ferrara, A., 1999, ApJ, 513, 142

[307] Madau, P., 1995, ApJ, 441, 18

[308] Madau, P. et al., 1996, MNRAS, 283, 1388

[309] Madau, P., Pozzetti, L. & Dickinson, M., 1998, ApJ, 498, 106

[310] Madau, P., Haardt, F. & Rees, M.J., 1999, ApJ, 514, 648

[311] Madau, P. & Rees, M.J., 2001, ApJL, 551, L27

[312] Madau, P., Ferrara, A. & Rees, M.J., 2001, ApJ, 555, 92

[313] Madau, P. et al., 2004, ApJ, 604, 484

[314] Madau, P. & Silk, J., 2005, MNRAS, 359, L37

[315] Magain, P. et al., 2005, Nature, 473, 381

[316] Magorrian, J. et al., 1998, AJ, 115, 2285

[317] Mahmood, A., Devriendt, J.E.G. & Silk, J., 2005, MNRAS, 359, 1363

[318] Mahmood, A. & Rajesh, A., 2005, astro-ph/0502513

[319] Maiolino, R. et al., 2001, A&A, 365, 28

[320] Maiolino, R., Marconi, A. & Oliva, E., 2001, A&A, 365, 37

[321] Maiolino, R. et al., 2003, ApJ, 596, L155

[322] Maiolino, R. et al., 2004, Nature, 431, 533

[323] Maiolino, R. et al., 2006, astroph/0509244

[324] Makino, N., Sasaki, S. & Suto, Y., 1998, ApJ, 497, 555

[325] Malhotra, S. & Rhoads, J.E., 2004, ApJL, 617, L5

[326] Malhotra, S. et al., 2005, ApJ, 626, 666

[327] Mannucci, F. et al., 2006, astroph/0607143

[328] Marchenko, S.V., 2006, Stellar Evolution at Low Metallicity: Mass Loss, Explosions, Cosmology, ASP Conference Series., astroph/0511147

[329] Marleau, F.R. et al., 2004, ApJS spitzer issue, astro-ph/0405635

[330] Marshall et al., 1983, ApJ, 265, 35

[331] Marconi, A. & Hunt, L.K., 2003, ApJ, 589, L21

[332] Marconi, A. et al., 2004, MNRAS, 351, 169

[333] Martin, C.L. et al., 2006, NewAR, 50, 53

[334] Martini, P. & Weinberg, D.H., 2001, ApJ, 547, 12

[335] Martini, P., 2004, in Carnegie Observatories Astrophysics Series, Vol. 1: Coevolution of Black Holes and Galaxies.

[336] Maselli, A. et al., 2006, astroph/0608209

[337] Mateo, M., 1998, ARA&A, 36, 435

[338] Mathur, S. & Grupe, D., 2005, astroph/0507624

[339] Matt, G., 2002, Phil.Trans.Roy.Soc.Lond., A360, 2045, astro-ph/0205164

[340] Matteucci, F. & Pipino, A., 2002, ApJL, 569, L69

[341] McLure, R.J. & Dunlop, J.S., 2004, MNRAS, 352, 1390

[342] McLure, R.J. et al., 2005, MNRAS, astroph/0510121

[343] McLure, R.J. et al., 2005, MNRAS, astroph/0606116

[344] Meiksin, A., 2005, MNRAS, 356, 596

[345] Meiksin, A, 2006, astroph/0512435

[346] Menci, N. et al., 2003, ApJL, 587, L63

[347] Merloni, A., Heinz, S. & Di Matteo, T., 2003, MNRAS, 345, 1057

[348] Merloni, A., 2004, MNRAS, 353, 1035

[349] Miller, L. et al., 2006, astroph/0608202

[350] Milosavljevic, M. et al., 2002, MNRAS, 331, L51

[351] Miyaji, T., Hasinger, G. & Schmidt, M., 2000, A&A, 353, 25

[352] Miyaji, T., Hasinger, G. & Schmidt, M., 2000, A&A, 369, 49

[353] Mo, H.J. & White, S.D.M., 1996, MNRAS, 282, 347

[354] Moore, B. et al., 1999a, ApJ, 524, L19

[355] Moore, B. et al., 1999b, MNRAS, 310, 1147

[356] Monaco, P., Salucci, P. & Danese, L., 2000, MNRAS, 311, 279

[357] Moran, E.C., Filippenko, A.V. & Chornock, R., 2002, ApJL, 579, L71

[358] Morgan, H.L. et al., 2003, ApJL, 597, L33

[359] Murray, S.D. & Lin, D.N.C., 1996, ApJ, 467, 728

[360] Mushotzky, R., 2004, Supermassive Black Holes in the Distant Universe(2004), Chapter 2, Kluwer Academic Publishers, also seen in astro-ph/0405144

[361] Myers, A.D. et al., 2005, astroph/0510371

[362] Naab, T., Khochfar, S. & Burkert, A., astroph/0509667

[363] Nagamine, K. et al., 2004, ApJL, 610, L45

[364] Nagamine, K. et al., 2006a, New Astronomy, 50, 29

[365] Nagamine, K. et al., 2006b, astroph/0603257

[366] Nagao, T., Marconi, A. & Maiolino, R., 2005, astroph/0510385

[367] Nagao, T., Maiolino, A & Marconi, A., 2006, astroph/0603580

[368] Nandra' K. et al., 2005, MNRAS, 360, L39

[369] Narayan, R. & Yi, I., 1994, ApJ, 428, L13

[370] Navarro, J.F., Frenk, C.S. & White, S.D.M., 1997, ApJ, 490, 493

[371] Navarro, J.F. & Steinmetz, M., 2000, ApJ, 538, 477

[372] Osmer, P.S., 2003, in Carnegie Observatories Astrophysics Series, Vol. 1: Coevolution of Black Holes and Galaxies, astro-ph/0304150

[373] Nelson, C.H. & Whittle, M., 1996, ApJ, 465, 96

[374] Nelson, C.H. et al., 2004, ApJ, 615, 652

[375] Netzer, H. & Trakhtenbrot, B., 2006, astroph/0607654

[376] Novak, G.S., Faber, S.M. & Dekel, A., 2005, astroph/0510102

[377] Ogando, R.L.C. et al., astroph/0509142

[378] Oh, S.P. & Furlanetto, S., ApJ, 620, L9

[379] Onken, C.A. et al., 2004, 615, 645

[380] Ostriker, J.P. & Thuan, T.X., 1975, ApJ, 202, 353

[381] Ostriker, J.P. & Ciotti, L., 2005, Phil. Trans. Roy. Soc. Lond. A. 363, 667

[382] Padmanabhan, T., 1993, Structure formation in the universe, Chap. 4, Cambridge university press

[383] Padmanabhan, T., Theoretical Astrophysics, Volume II: Stars and Stellar Systems, Chapter 2., 2001, Cambridge University Press

[384] Padmanabhan, T., 2002, Theoretical Astrophysics, Vol III: Galaxies and cosmology, Chap 1, Cambridge university press

[385] Padoan, P. & Nordlund, A., 2002, 576, 870

[386] Padovani, P. et al., 2004, A&A, 424, 545

[387] Page, L. et al., 2006, astroph/0603450

[388] Pagel, B.E.J., 1997, Nucleosynthesis and chemical evolution of galaxies, Chap 6, Cambridge university press

[389] Partridge, R.B. & Peebles, P.J.E., 1967a, ApJ, 147, 868

[390] Partridge, R.B. & Peebles, P.J.E., 1967b, ApJ, 148, 377

[391] Patton, D.R. et al., 1997, ApJ, 475, 29

[392] Peacock, J.A., Cosmological Physics, Chap. 11, Cambridge university press

[393] Peebles, P.J.E., 1993, Section 23, Principles of physical cosmology, Princeton Universiy Press

[394] Pei, Y.C., 1995, ApJ, 438, 623

[395] Peterson, B.M., 1993, PASP, 105, 247

[396] Peterson, B.M., 1997, An introduction to active galactic nuclei, Chap 2,5&6, Cambridge university press

[397] Peterson, J.R., 2001, A&A, 365, L104

[398] Pier, E.A. & Krolik, J.H., 1992, ApJ, 399, L23

[399] Pier, E.A. & Krolik, J.H., 1993, ApJ, 418, 673

[400] Piran, T., 1999, Physics Reports, 314, 575

[401] Pope, A. et al. 2005, MNRAS, 358, 149

[402] Pozzo, M. et al., 2004, MNRAS, 352, 457

[403] Press,W.H. & Schechter, P.L., 1974, ApJ, 181, 425

[404] Prochaska J.X. et al., 2003, ApJL, 595, L9

[405] Reed, D.S. et al., 2005, MNRAS, 363, 393

[406] Rejkuba, M. et al., 2002, ApJ, 564, 688

[407] Rosati, P. et.al., 2002, ApJ, 566, 667

[408] Richard, J. et al., 2006, astroph/0606134

[409] Richards, G.T. et al., 2006, astroph/0601434

[410] Ricotti, M. & Ostriker, J.P., 2004a, MNRAS, 350, 539

[411] Ricotti, M. & Ostriker, J.P., 2004b, MNRAS, 352, 547

[412] Ricotti, M. & Gnedin, N.Y., 2005, ApJ, 629, 259

[413] Riess, A., et al., 2004, ApJ, 600, L163

[414] Rigby, J.R. et al., 2004, ApJS spitzer issue, astro-ph/0406029

[415] Robertson, B. et al., 2005, astroph/0506038

[416] Romano, D. et al., 2002, MNRAS, 334, 444

[417] Romano-Diaz, E. et al., 2005, astroph/0508272

[418] Rothberg, B. & Joseph, R. D., 2004, AJ, 128, 2098

[419] Rothberg, B. & Joseph, R. D., 2005, astroph/0510019

[420] Roychowdhury, S. et al, 2004, ApJ, 615, 681

[421] Salpeter, E.E., 1955, ApJ, 121, 161

[422] Salpeter, E.E., 1964, ApJ, 140, 796

[423] Salpeter, E. E., 1955, ApJ, 121, 161

[424] Salvaterra, R. & Ferrara, A., 2003, MNRAS, 339, 973

[425] Salvaterra, R. & Ferrara, A., 2006, MNRAS, 367, L11

[426] Salvaterra, R., Haardt, F. & Ferrara, A., 2006, MNRAS, astroph/0507208

[427] Salvaterra, R. et al., 2006, astroph/0512403

[428] Sandage, A., 1971, in Proceedings of a Study Week on Nuclei of Galaxies, New York: American Elsevier

[429] Sanders, D.B. et al, 1989, ApJ, 347, 29

[430] Santos, M.R., Bromm, V. & Kamionkowski, M., 2002, MNRAS, 336, 1082

[431] Santos, M.R., 2004, MNRAS, 349, 1137

[432] Santos, M.R. & Cooray, A., 2006, astroph/0605677

[433] Sasaki, S., 1994, PASJ, 46, 427

[434] Satyapal, S. et al., 2005, ApJ, 633, 86

[435] Sazonov, S.Y. et al., 2005, MNRAS, 358, 168

[436] Scalo, J.M., 1986, Fund. Cosmic. Phys., 11, 1

[437] Scannapieco, E., Silk, J. & Bouwens, R., 2005, ApJ, 635, L13

[438] Schaerer, D., 2002, A&A, 382, 28

[439] Schaerer, D., 2003, A&A, 397, 527

[440] Schechter, P., 1976, ApJ, 203, 297

[441] Schirber, M. & Bullock, J.S., 2003, ApJ, 584, 110

[442] Schmidt, M., 1968, ApJ, 151, 393

[443] Schmitt, H.R., et al., 1997, AJ, 114, 592

[444] Schneider R., Ferrara, A.& Salvaterra, R., 2004, MNRAS, 351, 1379

[445] Schneider R. et al., 2006, astroph/0510685

[446] Severgnini, P. et al., 2005, A&A, 431, 87

[447] Shakura, N.I. & Sunyaev, R.A., 1973, A&A, 24,337

[448] Shankar, F. et al., 2004, MNRAS, 354, 1020

[449] Shankar, F. et al., 2006, ApJ, astroph/0601577

[450] Shanks, T. et al., 1987, MNRAS, 277, 739

[451] Shanks, T. & Boyle, B.J., 1994, MNRAS, 271, 753

[452] Shapley, A.E. et al., 2006, 0606635

[453] Shapiro, P.R. & Giroux, M.L., 1987, ApJ, 321, L107

[454] Shapiro, P.R. et al., 2006, astroph/0512516

[455] Sharp, R.G. et al., 2004, MNRAS, 350, 449

[456] Shaver, P.A., 1984, MNRAS, 136, L9

[457] Sheth, R.K. et al., 2003, ApJ, 594, 225

[458] Sheth, R.K. & Tormen, G., 1999, MNRAS, 308, 119

[459] Sheth, R.K. & Tormen, G., 2002, MNRAS, 329, 61

[460] shields, G.A. et al., 2003, ApJ, 583, 124

[461] Shields, G.A. et al., 2006, astroph/0512418

[462] Shimasaku, K. et al., 2006, astroph/0602614

[463] Silk, J., 1995, ApJL, 438, L41

[464] Silk, J. & Rees, M.J., 1998, A&A, 331, L1

[465] Silk, J. & Bouwens, R., 2001, Galaxy Formation, in Encyclopedia of Astronomy and Astrophysics

[466] Silva, L. et al., 1998, ApJ, 509, 103

[467] Silva, L. et al., 2005, MNRAS, 357, 1295

[468] Simpson, C. et al., 2004, MNRAS, 353, 179

[469] Sirianni, M. et al., 2005, astroph/0507614

[470] Small, T.A. & Blandford, R.D., 1992, ApJ, 259, 725

[471] Somerville, R.S. & Primack, J.R., 1999, MNRAS, 310, 1087

[472] Somerville, R.S. & Livio, M., 2003, ApJ, 593, 611

[473] Somerville, R.S. et al., 2004, ApJL, 600, L135

[474] Songaila, A., 2001, ApJL, 561, L153

[475] Spergel, D.N. et al., 2003, ApJS, 148, 175

[476] Spergel, D.N. et al., 2006, astroph/0603449

[477] Springel, V. & Hernquist, L., 2003, MNRAS, 339, 312

[478] Springel, V., Di Matteo, T. & Hernquist, L., 2005a MNRAS, 361, 776

[479] Springel, V., Di Matteo, T. & Hernquist, L., 2005b, ApJ, 620, L79

[480] Springel, V. et al., 2005, Nature, 435, 629

[481] Stanway, E.R. et al., 2004, ApJ, 607, 704

[482] Stark, D.P. et al., 2006, astroph/0604250

[483] Steidel, C.C. & Hamilton, D., 1992, AJ, 104, 941

[484] Steidel, C.C. et al., 1996, AJ, 112, 352

[485] Steidel, C.C. et al., 1999, ApJ, 519, 1

[486] Steidel, C.C., Pettini, M. & Adelberger, K.L., 2001, ApJ, 546, 665

[487] Sterken, C. & Manfroid, J., 1992, Astronomical photometry, Chap. 13&16, Kluwer Academic Publishers

[488] Stern, D. et al., 2006, astroph/0607507

[489] Stiavelli, M. Fall, S.M. & Panagia, N., 2004, ApJ, 600, 508

[490] Stoehr, F. et al., 2002, MNRAS, 335, L84

[491] Stoehr, F. et al., 2003, MNRAS, 345, 1313

[492] Stoehr, F., 2006, MNRAS, astroph/0403077

[493] Szokoly, G.P. et al., 2004, ApJS, 155, 271

[494] Tamura, T. et al., 2001, A&A, 365, L87

[495] Tanaka, Y. et al., 1995, Nature, 375, 659

[496] Taniguchi, Y. et al., 2005, PASJ, 57, 165

[497] Tegmark, M. et al., 1997, ApJ, 474, 1

[498] Thomas, D., Greggio, L. & Bender, R., 1999, MNRAS, 302, 537

[499] Thompson et al., 2006, ApJ, astroph/0503504

[500] Todini, P. & Ferrara, A., 2001, MNRAS, 325, 726

[501] Toomre, A. & Toomre, J., 1972, ApJ, 178, 62

[502] Tosi, M. et al., 2001, AJ, 122, 1271

[503] Totani, T. et al., 2001, ApJL, 550, L137

[504] Tremaine, S. et.al., 2002, ApJ, 574, 740

[505] Treu, T. et al., 2004, ApJ, 615, L97

[506] Treu, T. et al., 2005, ApJ, 622, L5

[507] Tully, R.B. & Fisher, J.R., 1977, A&A, 54, 661

[508] Tumlinson, J. & Shull, J.M., 2000, ApJL, 528, L65

[509] Tumlinson, J., Shull, J.M. & Venkatesan, A., 2003, ApJ, 584, 608

[510] Tumlinson, J., Venkatesan, A. & Shull, J.M., 2004, ApJ, 612, 602

[511] Tumlinson, J., 2006, astroph/0602179

[512] Ueda, Y. et al., 2003, ApJ, 598, 886

[513] Umemura, M., Nakamoto, T. & Susa, H., 2001, The Physics of Galaxy Formation, ASP Conference Proceedings, Vol. 222. p.109

[514] Urry, C. M & Padovani, P., 1995, PASP, 107, 803

[515] van Dokkum, P.G. & Stanford, S.A., 2003, ApJ, 585, 78

[516] van Dokkum, P.G., 2005, AJ, 130, 2647

[517] Vanden Berk, D., et al., 2001, AJ, 122, 549

[518] Vanzella, E. et al., 2001, AJ, 122, 2190

[519] Vanzella, E. et al., 2004, A&A, 423, 761

[520] Venkatesan, A., Nath, B.B. & Shull, J.M., 2006, ApJ, astroph/0508163

[521] Venn, K.A. et al., 2003, Carnegie Observatories Astrophysics Series, Vol. 4: Origin and Evolution of the Elements, ed. A McWilliam and M. Rauch, astroph/0305188

[522] Vestergaard, M., 2004, ApJ, 601, 676

[523] Vestergaard, M. & Peterson, B.M., 2006, ApJ, 641, 689

[524] Vignali, C. et al., 2003, AJ, 125, 2876

[525] Vink, J.S., de Koter, A. & Lamers, H.J.G.L.M., 2001, A&A, 369, 574

[526] Voit, G.M., 2004, astroph/0410173

[527] Volonteri, M., Haardt, F & Madau, P., 2002, Ap&SS, 281, 501

[528] Volonteri, M. & Rees, M.J., 2005, astroph/0506040

[529] Wada, K. & Venkatesan, A., 2003, ApJ, 591, 38

[530] Wang, J.-M., 2003, AJ, 125, 2859

[531] Wang, J.X. et al., 2004, astro-ph/0405499

[532] Wang, J. &. Wei, J.Y., 2006, astro-ph/0605377

[533] Wang, R., Wu, X.-B. & Kong, M.-Z., 2006, astroph/0603514

[534] Warner, C., Hamann, F. & Dietrich, M., 2004, ApJ, 608, 136

[535] Watson, D. et al., 2006, ApJL, astroph/0509640

[536] Webb, T.M. et al., 2003, ApJ, 587, 41

[537] Weedman, D.W., 1986, Quasar Astronomy, Chap. 8&9, Cambridge University Press

[538] Weedman, D. et al., 2004, ApJ, 600, 106

[539] Weinberg, S., 1972, Gravitation and cosmology, Chap. 3&4, John Wiley & Sons, Inc.

[540] White, R.L. et al., 2003, ApJ, 126, 1

[541] White, S.D.M. & Rees, M.J., 1978, MNRAS, 183, 341

[542] White, S.D.M. & Frenk, C.S., 1991, ApJ, 379, 52

[543] Whittet, D.C.B., 1992, Dust in The Galactic Environment, IOP Publishing Ltd.

[544] Williams, R.E. et al., 1996, AJ, 112, 1335

[545] Wilkes, B.J. et al., 2000, in the Springer Lecture Notes of Physics Series as part of the proceedings for "ISO Surveys of a Dusty Universe", astro-ph/0001488

[546] Wilson, G. et al., 2002, AJ, 124, 1258

[547] Wirth, G.D. et al., 2004, AJ, 127, 3121

[548] Wolf, C. et al., 2003, A&A, 408, 499

[549] Wolter, A. et al., 2005, A&A, astroph/0510045

[550] Wu, Q. & Cao, X., 2006, astroph/0607034

[551] Wyithe, J.S.B. & Loeb, A., 2002, ApJ, 581, 886

[552] Wyithe, J.S.B. & Loeb, A., 2003a, ApJ, 595, 614

[553] Wyithe, J.S.B. & Loeb, A., 2003b, ApJL, 588, L69

[554] Wyithe, J.S.B. & Loeb, A., 2005, astroph/0506294

[555] Wyithe, J.S.B. & Cen, R., 2006, ApJ, 0602503

[556] Wyithe, J.S.B. & Loeb, A., 2006, astroph/0603550

[557] Yamada, T. et al., 2005, astroph/0508594

[558] Yan, H. & Windhorst, R.A., 2004a, ApJ, 600, L1

[559] Yan, H. & Windhorst, R.A., 2004b, ApJ, 612, L93

[560] Yoshida et al., 2006, astroph/0606106

[561] Yu, Q. & Lu, Y., 2004, ApJ, 602, 603

[562] Zaldarriaga, M. & Seljak, U., 1997, Phys. Rev. D., 55, 1830

[563] Zaldarriaga, M. & Seljak, U., 1998, Phys. Rev. D., 58, 023003

[564] Zepf, S.E. & Koo, D.C., 1989, ApJ, 337, 34

[565] Zhao, D.H. et al., 2003, ApJL, 597, L9

[566] Zhao, H. & Silk, J., 2005, PRL, 95, 011301

[567] Zheng et al., 2004, astro-ph/0406482

[568] Zhou, H. et al., 2006, astroph/ 0603759

[569] Zinnecker, H., 1984, MNRAS, 210, 43